UNIVERSITY OF CALIFORNIA SAN DIEGO

Investigation of Charge Ordering in the Strongly Correlated Materials $Pr_xY_{1-x}Ba_2Cu_3O_7$ and FeGe by Synchrotron-based X-ray Techniques

A dissertation submitted in partial satisfaction of the
requirements for the degree
Doctor of Philosophy

in

Physics

by

Brandon Gunn

Committee in charge:

Professor Alex Frañó, Chair
Professor Eric Fullerton
Professor Brian Maple
Professor Tenio Popmintchev
Professor Oleg Shpyrko

2024

The dissertation of Brandon Gunn is approved, and it is acceptable in quality and form for publication on microfilm and electronically.

University of California San Diego

2024

DEDICATION

This dissertation is dedicated to my son and to my wife and family, for always supporting me.

TABLE OF CONTENTS

LIST OF FIGURES

LIST OF TABLES

ACKNOWLEDGEMENTS

Thank you to my advisor and mentor Alex Frañó for his unyielding support throughout the entirety of my doctoral program. Thank you to Alejandro Ruiz for the priceless experience bestowed upon me during our countless hours spent conducting synchrotron experiments. Thank you to Rourav Basak for the overabundance of fruitful discussions and unwavering collaboration in conducting many of these experiments. Thank you to Joshua Evans for the invaluable assistance analyzing much of the experimental data. Thank you to Biswajit Sahoo and Thorsten Schmitt for your assistance collecting the XAS and RIXS data from the Swiss Light Source. Thank you to Sarmistha Das, Mayia Vranas, Elliot Kisiel, Dong Le, Wei He, Robin Glefke, Kate Matthews, Ashley Corey and the rest of the X Lab members for making this experience so memorable. Thank you to Brian Maple for PYBCO project inspiration and guidance. Thank you to Camilla Moir and Kalyan Sasmal for growing the PYBCO samples. Thank you to Yi Lu for your help in the PYBCO project and invaluable assistance with DFT and Quanty. Thank you to Tim Boyle, Morgan Walker, and Eduardo da Silva Neto, and Santi Blanco-Canosa for your help with the PYBCO project. Thank you to Yu He for the fruitful discussions and help in the PYBCO project. Thank you to Fanny Rodolakis for your incalculably tremendous time and effort put into our many beamtimes at APS. Thank you to Jun-Sik Lee and Hai Huang for your help measuring the 3D CO at SSRL. Thank you to Martin Sundermann and Hlynur Gretarsson for your help with the orbital imaging. Thank you to Ayman Said for your help measuring the PYBCO phonon dispersions. Thank you to Xiaokun Teng, Ming Yi, Ananya Biswas, and Pengcheng Dai for letting me be a part of the FeGe project and your help throughout. Thank you to Phil Ryan and Jong Woo Kim for your help measuring the FeGe at APS. Thank you to all other collaborators, without whom this research would not have been possible.

Chapter 4.2.4, in full, is a reprint of the material as it appears in Nature Communications in Stabilization of three-dimensional charge order through interplanar orbital hybridization in $Pr_xY_{1-x}Ba_2Cu_3O_{6+\delta}$. A. Ruiz, B. Gunn, Y. Lu, K. Sasmal, C. M. Moir, R. Basak, H. Huang, J.-S.

Lee, F. Rodolakis, T. J. Boyle, M. Walker, Y. He, S. Blanco-Canosa, E. H. da Silva Neto, M. B. Maple, and A. Frañó, Nature Communications, 2022. The dissertation author was a primary investigator and author of this paper.

VITA

2015	A. S. in Mathematics, Diablo Valley College
2015	A. S. in Physics, Diablo Valley College
2018	B. S. in Physics *cum laude*, San Francisco State University
2024	Ph. D. in Physics, University of California San Diego

PUBLICATIONS

B. Gunn, R. Basak, A. Ruiz, J. Evans, Y. Lu, C. M. Moir, M. B. Maple, and A. Frañó. *Characterization of $Pr_xY_{1-x}Ba_2Cu_3O_{6+\delta}$ by resonant and non-resonant inelastic x-ray scattering techniques*. In preparation.

R. Basak, S. Das, U. S. Goteti, B. Gunn, J. Evans, N. Sarkar, P. Shafer, C. Klewe, J. W. Freeland, F. M. Rodolakis, S. A. Cybard, R. C. Dynes, and A. Frañó. *Tuning a coupled phase transition in nickelate thin films using helium ion implantation*. In preparation.

P. Salev, E. Kisiel, D. Sasaki, B. Gunn, W. Ho, M. Feng, J. Li, N. Tamura, I. Poudyal, Z. Islam, Y. Takamura, A. Frañó, I. K. Schuller. *Inhomogeneous lattice strain induced by electrical triggering of a metal-insulator transition.* Submitted.

X. Chen, A. Ruiz, A. J. Bishop, B. Gunn, R. Basak, T. Zhu, Y. He, M. Vranas, E. Weschke, R. K. Kawakami, R. J. Birgeneau, and A. Frañó. *Antiferromagnetic order in a layered magnetic topological insulator $MnBi_2Se_4$ probed by resonant soft x-ray scattering*. Phys. Rev. B **109**, 184418 (2024).

V. Sunko, Y. Sun, M. Vranas, C. C. Homes, C. Lee, E. Donoway, Z.-C. Wang, S. Balguri, M. B. Mahendru, A. Ruiz, B. Gunn, R. Basak, S. Blanco-Canosa, E. Schierle, E. Weschke, F. Tafti, A. Frañó, and J. Orenstein. *Spin-carrier coupling induced ferromagnetism and giant resistivity peak in $EuCd_2P_2$*. Phys. Rev. B **107**, 144404 (2023).

A. Ruiz*, B. Gunn*, Y. Lu, K. Sasmal, C. M. Moir, R. Basak, H. Huang, J.-S. Lee, F. Rodolakis, T. J. Boyle, M. Walker, Y. He, S. Blanco-Canosa, E. H. da Silva Neto, M .B. Maple, and A. Frañó. *Stabilization of three-dimensional charge order through interplanar orbital hybridization in $Pr_xY_{1-x}Ba_2Cu_3O_{6+\delta}$*. Nat. Commun. **13**, 6197 (2022).

S. Zhang, I.-T. Chiu, M.-H. Lee, B. Gunn, M. Feng, T. J. Park, P. Shafer, A. T. N'Diaye, F. Rodolakis, S. Ramanathan, A. Frañó, I. K. Schuller, Y. Takamura, and G. Galli. *Determining the oxygen stoichiometry of cobaltite thin films*. Chem. Mater. **34**, 2076-2084 (2022).

M. Vagadia, S. Sardar, T. Tank, S. Das, B. Gunn, P. Pandey, R. Hübner, F. Rodolakis, G. Fabbris, and Y. Choi, D. Haskel, A. Frañó, and D. S. Rana. *Extraordinary anisotropic magnetoresistance in $CaMnO_3/CaIrO_3$ heterostructures*. Phys. Rev. B **105**, L020402 (2022).

* These authors contributed equally.

ABSTRACT OF THE DISSERTATION

Investigation of Charge Ordering in the Strongly Correlated Materials $Pr_xY_{1-x}Ba_2Cu_3O_7$ and FeGe by Synchrotron-based X-ray Techniques

by

Brandon Gunn

Doctor of Philosophy in Physics

University of California San Diego, 2024

Professor Alex Frañó, Chair

A primary focus of modern condensed matter physics concerns the study of strongly correlated materials in which enhanced electron interactions give rise to emergent phenomena, such as high-temperature superconductivity. The strong electromagnetic coupling between electrons and photons makes x-rays a highly sensitive probe for investigating the emergent properties of these materials. The advent of modern synchrotron light sources significantly enhances these capabilities through the production of high-brilliance x-ray beams that offer full control over the incident photon energy, thereby enabling the detection of signals emanating from phases in which only a small number of valence electrons contribute to the scattering signal via resonant

enhancement. This dissertation demonstrates how these synchrotron-based x-ray scattering and spectroscopy techniques can be utilized to study a wide range of material characteristics and electronic properties in modern condensed matter systems. The x-ray techniques are applied to the characterization of two strongly correlated systems, $Pr_xY_{1-x}Ba_2Cu_3O_7$ and FeGe. In $Pr_xY_{1-x}Ba_2Cu_3O_7$, x-ray absorption spectroscopy and resonant inelastic x-ray scattering are used to elucidate the effects of the substituted Pr ion on the electronic structure, non-resonant inelastic x-ray scattering techniques are employed to determine the shape of the active Cu $3d$ orbital hole that is responsible for the anisotropic behavior observed in transport measurements, and resonant elastic x-ray scattering techniques are used to investigate a novel three-dimensional charge order that is stabilized by the Pr substitution and is demonstrated to compete directly with the high-temperature superconducting phase. Resonant elastic x-ray scattering techniques are further utilized to probe the role of the Ge honeycomb lattice in the formation of charge order in the kagome metal FeGe, which is supported by density-functional theory calculations. Understanding and controlling the correlated phenomena in these and other quantum materials has significant implications for various technologies, including quantum computing, energy storage, and next-generation electronics.

Chapter 1

Introduction

1.1 Scope of this dissertation

The underlying goal of this dissertation, in addition to presenting the novel research conducted throughout the doctoral program, is to prepare a graduate or advanced undergraduate student to begin performing research that involves utilizing x-rays to characterize materials. The entirety of the x-ray scattering and absorption data presented in this dissertation were collected at synchrotron light sources and, accordingly, this will be the dissertation's primary focus. Experiments conducted at synchrotrons typically involve using intricate and complex equipment, often involving vacuum systems, four-circle goniometers, and delicate detectors within a relatively short time frame (usually 2-6 days per beamtime), which can result in an overwhelming experience for new students. The intention of this dissertation is to provide a foundation of practical information regarding general synchrotron-based experimental procedures so that students encountering their first beamtime can more primarily focus on the details of their experiment, rather than on the intricacies of the synchrotron operations. Because synchrotron beamtime is so valuable, it is generally advisable to pre-characterize samples using a standard laboratory x-ray source, which will also be briefly discussed in this dissertation. Additionally,

there are many parallels between x-ray and neutron scattering experiments, oftentimes yielding information that is highly complimentary to one another. In an effort to inform and encourage students about utilizing this additional probe, the properties of x-rays will largely be contrasted against those of neutrons, even though no neutron-based data is presented within this dissertation. This may be particularly insightful to students who are already experienced with x-ray scattering and wish to learn the basics of neutron scattering through the comparative lens of something with which they are already familiar.

To this end, the first half of this dissertation introduces the basic properties and characteristics of probing matter with x-rays and provides detailed information about a useful assortment of synchrotron-based experimental techniques, namely:

1. x-ray absorption spectroscopy
2. resonant and non-resonant elastic x-ray scattering
3. resonant and non-resonant inelastic x-ray scattering

These techniques constitute the basic tenets of modern synchrotron experiments, collectively representing a vast multitude of condensed matter phenomena which may be investigated through their means, while also providing a useful foundation to learning many other synchrotron-based techniques not covered in this dissertation.

The second half of this dissertation presents the research conducted during the entirety of this doctoral program. It contains examples for all of the synchrotron-based techniques that are discussed in the first half of this dissertation. It shows how various material characteristics and electronic properties can be uncovered through the application of these techniques to two strongly correlated systems, $Pr_xY_{1-x}Ba_2Cu_3O_7$ and FeGe. Additionally, some computational modeling, primarily density-function theory calculations, which are further discussed in Appendix C, is included to compliment the experimental data.

Chapter 2 This chapter discusses utilizing x-rays to study material systems. The properties of x-rays which make it a suitable probe for investigating matter are contrasted against those of neutrons. The generation mechanisms and characteristics of x-rays produced by standard laboratory sources and synchrotron light sources are compared. The interactions between x-rays and matter by either scattering or absorbing are detailed, distinguishing between elastic, inelastic, and resonant scattering processes.

Chapter 3 The principles and characteristics of x-rays and their interactions with matter are applied to various synchrotron-based experimental techniques, including x-ray absorption spectroscopy and resonant/non-resonant elastic/inelastic x-ray scattering.

Chapter 4 The majority of this doctoral research focused upon characterizing the $Pr_xY_{1-x}Ba_2Cu_3O_7$ system, which is summarized in this chapter. The experimental x-ray scattering and spectroscopy techniques discussed in Chapter 3 are used to extract information about the material and electronic properties of this system, including imaging the shape of the active copper $3d$ orbital, as well as characterizing a three-dimensional charge ordering phase which directly competes with superconductivity.

Chapter 5 The remainder of this doctoral research focused on studying charge ordering in the kagome metal FeGe. Preliminary measurements and density-functional theory calculations are included in this section.

Chapter 2

Fundamentals of X-rays

2.1 X-ray Properties and Characteristics

Light is of the most fundamental of probes used to study physical systems. As the story goes, it was Sir Isaac Newton's visual observation of an apple falling from a tree that led him to develop the first theory of gravity [1]. Up until the recent first observation of gravitational waves [2], light was effectively the *only* probe available to astronomers that has been capable of yielding information about galaxies, stars, and other distant celestial phenomena [3]. While astronomy largely concerns itself with objects separated by unimaginably vast distances, the use of light, and in particular, x-rays, is no less useful as a tool for investigating phenomena of inconceivably small length scales, as well. One such notable example includes how Rosalind Franklin was able to resolve the double-helix structure of DNA, a molecule $\sim$2 nm in size, using x-ray diffraction in 1953 [4]. Moreover, at least seven Nobel prizes have been awarded for topics that are directly related to or have utilized the x-ray-based techniques discussed in this dissertation [5]:

- to Wilhelm Conrad Röntgen in 1901 (physics) "in recognition of the extraordinary services he has rendered by the discovery of the remarkable rays subsequently named after him"

- to Max von Laue in 1914 (physics) ”for his discovery of the diffraction of x-rays by crystals”
- to Sir William Henry Bragg and William Lawrence Bragg in 1915 (physics) ”for their services in the analysis of crystal structure by means of x-rays”
- to Max Ferdinand Perutz and John Cowdery Kendrew in 1962 (chemistry) ”for their studies of the strutures of globular proteins”
- to Francis Harry Compton Crick, James Dewey Watson, and Maurice Hugh Frederick Wilking in 1962 (medicine) ”for their discoveries concerning the molecular structure of nucleic acids and its significance for information transfer in living materials”
- to Dorothy Crowfoot Hodgkin in 1964 (chemistry) ”for here determinations by x-ray techniques of the structures of important biochemical substances”
- to Allan M. Cormack and Godfrey N. Hounsfield in 1979 (medicine) ”for the development of computer assisted tomography”

It is impossible to overstate the significance that x-ray scattering and spectroscopy techniques have played in advancing our understanding of multiple scientific fields, from materials science to genetic engineering.

Light has a variety of properties which make it highly suitable for investigating material systems. For the sake of making an illuminating and useful comparison, these properties will be contrasted against those of neutrons, which are also often used in material science to provide complimentary information with x-rays due to fundamental differences in its particle properties and interaction mechanisms. Photons can essentially interact with matter in one of two ways: the photon can either be *absorbed* or *scattered.* Both of these interaction mechanisms can be utilized to gain information about the material being studied and will be discussed in depth in Chapter 3. Although neutrons can also be absorbed by a material, albeit by the atomic nuclei in a process

called *neutron capture* which changes the elemental isotope [6], there is not really a common analogous experimental technique to x-ray absorption spectroscopy for neutrons. For scattering, though, the concept is largely the same regardless of whether x-rays or neutrons[1] are being used: scattering from atoms creates interference (diffraction) patterns which can be used to probe how atoms are arranged within a material. It may be useful for the reader to keep this context in mind while reading the following comparison between probing with x-rays and neutrons.

Within the context of quantum field theory, photons are elementary particles and are the carriers of the electromagnetic force [7] which only couple to charged particles, which happen to primarily be electrons in most experiments and everyday situations. Because photons carry no charge themselves, photons do not directly interact with each other. That is to say, if you point two beams of light such that their paths are crossing, the beams of light will pass through one another unperturbed, unlike, for example, two crossed jets of water, which would interact very strongly. That is not to say that photons cannot interact indirectly through nonlinear effects, but these interactions are generally only non-negligible if the beam intensities within an optical media are sufficiently high, such as in the case of two-photon absorption [8], or if the photon energies are greater than the total rest mass energy of a spontaneously created particle–antiparticle pair (e.g., $E \geq 1.022$ MeV, in the case of electron–positron pair production) [9], which mostly occur within particle colliders or from very high-energy cosmological gamma rays. As is the case with all of the force mediators, photons are bosons and carry a spin of 1.

Neutrons, by contrast, are composite particles composed of one up quark (charge $\frac{2}{3}$, spin $\frac{1}{2}$) and two down quarks (charge $-\frac{1}{3}$, spin $\frac{1}{2}$). Although neutrons are stable when bound with other nucleons, they are unstable outside of a nucleus and will undergo beta minus decay, transforming into a proton via the process

$$n \rightarrow p + e^{-} + \overline{\nu_e}$$

[1] Electrons are also used but will not be discussed in this dissertation.

where n is a neutron, p is a proton, e^- is an electron, and $\overline{\nu_e}$ is an electron antineutrino. Fortunately, as this is a consequence of the weak nuclear force, the resulting lifetime is relatively long at $\sim$15 minutes, making it feasible to use neutrons as a probing source[2]. Similar to the photon, the neutron's net charge is zero, due to the sum of the charges of its quarks[3]. However, unlike the chargeless photon, because the neutron is not the electromagnetic force carrier (i.e., is not itself associated with oscillating electromagnetic fields), its inherent lack of charge implies that it does *not* interact with charged particles via the electric force, according to Coulomb's law

$$\boldsymbol{F_E} = \frac{1}{4\pi\varepsilon_0}\frac{q_1 q_2}{r^2}\hat{\boldsymbol{r}}$$

where ε_0 is the permittivity of free space, q_1 and q_2 are the particle charges, r is the separation between particles, and $\hat{\boldsymbol{r}}$ is the unit vector of $\boldsymbol{r}$. Thus, unlike photons, neutrons are not scattered by the electrons (we'll soon see there is a major exception to this) in a material but rather by the atomic nuclei via the strong nuclear force.

Spins do not directly sum the way that charge does (the detailed explanation why requires quantum chromodynamics, the theory which describes the strong nuclear force, which is highly complex and well beyond the scope of this dissertation) and, as such, the neutron's spin is $\frac{1}{2}$, making it a fermion. While this difference indeed means that neutrons obey Fermi-Dirac statistics while photons obey Bose-Einstein statistics, the application of the Pauli Exclusion Principle to the former is mostly involved in the theory of the shell model of nuclear energy states within atomic nuclei and is not so relevant within the context of the neutron-scattering-based techniques used to probe material systems.

A significant practical implication resulting from the bosonic versus fermionic nature of photons and neutrons, respectively, is that it is significantly easier to generate x-rays than

[2] As an interesting aside, due to the quirk of time dilation within special relatively which describes how objects move more slowly through the time dimension as they travel more quickly through the spatial dimensions, photons effectively do not experience time, making the concept of decaying with some finite lifetime nonsensical.

[3] It is interesting to note, though, that the neutron *does* have an internal charge structure which is distinctly opposite from its antiparticle, the antineutron. The photon, in contrast, is its own antiparticle.

neutrons. Because neutrons are fermionic (*baryonic*, more specifically) they are subject to the conservation of baryon number [10], which implies that they cannot be created ad hoc through energy conversions, but rather must either be obtained from pre-existing sources of neutrons or created in processes in which baryon number is conserved, such as in electron capture

$$p + e^- \rightarrow n + \nu_e$$

where p is a proton, e^- is an electron, n is a neutron, and ν_e is an electron neutrino. The latter method is not typically feasible for producing beams of neutrons, so they are generally either obtained through the fission of radioactive elements, such as uranium, (e.g., reactor neutron sources) or by using a proton beam to blast apart heavy elements (e.g., spallation neutron sources). Bosonic x-rays, in contrast, are not subject to any such number conservation laws and may easily be created by atomic electron transitions (e.g., standard laboratory x-ray sources) or by the (de)acceleration of charged particles (e.g., synchrotron x-ray sources), both of which will be discussed in detail in Section 2.3.3.

2.2 Probing Matter with X-rays

The fact that both x-rays and neutrons have non-zero spins is also relevant. It implies that both particles are polarized, which can be utilized experimentally (e.g., measuring magnetic dichroism). It also subjects both particles to spin conservation laws, which is relevant for x-ray absorption and emission, for example. Additionally, having a non-zero spin allows neutrons (unlike photons, because they have no mass) to have a non-zero magnetic dipole moment, given by the equation

$$\boldsymbol{\mu} = -g_n \frac{e\,\hbar}{2m_n} \boldsymbol{S_n}$$

where g_n is the neutron gyromagnetic ratio, e is the elementary charge, $\hbar$ is the reduced Planck constant, m_n is the neutron mass, and $\boldsymbol{S_n}$ is the neutron spin angular momentum. Critically, this property allows neutrons to interact with electrons magnetically in the absence of Coulombic interactions. Unlike photons, neutrons are not able interact with all electrons in a material, rather only with unpaired electrons in the outer shells. However, as it turns out, for neutrons, this magnetic scattering by electrons is of a comparable magnitude as structural nuclear scattering. This makes neutrons a powerful tool for determining magnetic structures (e.g., ferromagnetism, antiferromagnetism, etc.) within materials. Although, historically, neutrons have been the probe of choice for studying both static and dynamic magnetic structures, while x-rays have been used to provide information about crystal structures through interactions with the electronic charge distributions, it should be expected that x-rays are also sensitive to magnetic distributions, considering that x-rays are part of the *electromagnetic* spectrum (Figure 2.1). Unlike neutrons, however, the structural[4] and magnetic scattering amplitudes are **not** of comparable strength. For x-rays, the charge-based structural scattering amplitude is significantly stronger than for magnetic scattering. For an x-ray scattering from a single electron, the ratio of these two scattering amplitudes is [11, 12]:

$$\frac{A_{magnetic}}{A_{charge}} = \frac{\hbar\omega}{m_e c^2}$$

where $\hbar$ is the reduced Planck constant, ω is the angular frequency, m_e is the electron mass, and c is the speed of light. This ratio is 0.01 for 5.11 keV x-rays, resulting in a magnetic scattering intensity that is a factor 10^{-4} times weaker than the corresponding charge scattering intensity. This is compounded by the fact that all atomic electrons contribute to the charge scattering while only electrons with unpaired angular momenta in open shells contribute to the magnetic scattering, which can decrease the relative magnetic scattering intensity by another

[4]It is important to remember here that, while *structural* scattering refers to scattering by the atomic lattice for both cases, neutrons are primarily scattered by the atomic nuclei while photons are scattered by the electrons.

factor of $\sim 10^{-2}$. While it may initially seem that this relatively low magnetic scattering intensity renders x-rays virtually useless as a probe studying magnetic systems, this is not necessarily the case for situations in which the magnetic peak being investigated does not overlap with any charge peaks. In these cases, magnetic peaks can still be measured within reasonable time frames if the low scattering intensity is compensated by an increase in x-ray flux that is of comparable magnitude. As discussed in Section 2.3.3, such a high x-ray flux can be easily achieved at many modern synchrotron light sources. Neutron sources, on the other hand, are more limited in their ability to produce neutrons. Therefore, even though neutrons have a greater magnetic interaction strength than x-rays, it is often able to measure magnetic structures in a comparable amount of time using x-rays, due to the significantly higher flux provided by synchrotron light sources than neutron sources.

Penetration depth is another property that is significantly different between x-rays and neutrons that arises from their difference in interaction mechanisms. Because x-rays interact so strongly with electron densities via the Coulomb force, the penetration depth is relatively low. While the x-ray penetration depth does vary depending on factors such as the sample composition, the wavelength of x-rays being used, and the angle of incidence, the strong sample interaction ultimately dictates that probing with x-rays is a surface-sensitive technique. The significantly weaker nucleon-nucleon interactions between neutrons and matter (resulting from the very short range of the strong nuclear force and tiny size of the nucleus relative to the entire atom) means that they are highly penetrating, making neutron scattering a bulk-sensitive probe. To illustrate the degree of interaction strength disparity between x-rays and neutrons with matter, $>95\%$ of a neutron beam would be transmitted through a 5 mm thick aluminum plate, compared to $<0.1\%$ for an x-ray beam [14].

An important corollary of this significant contrast in probe-sample interaction strength is the relative sample *size* that is required. The relatively shallow penetration depth of x-rays (often < 1 μm for soft x-rays and up to tens of μm for hard x-rays), in conjunction with the ability

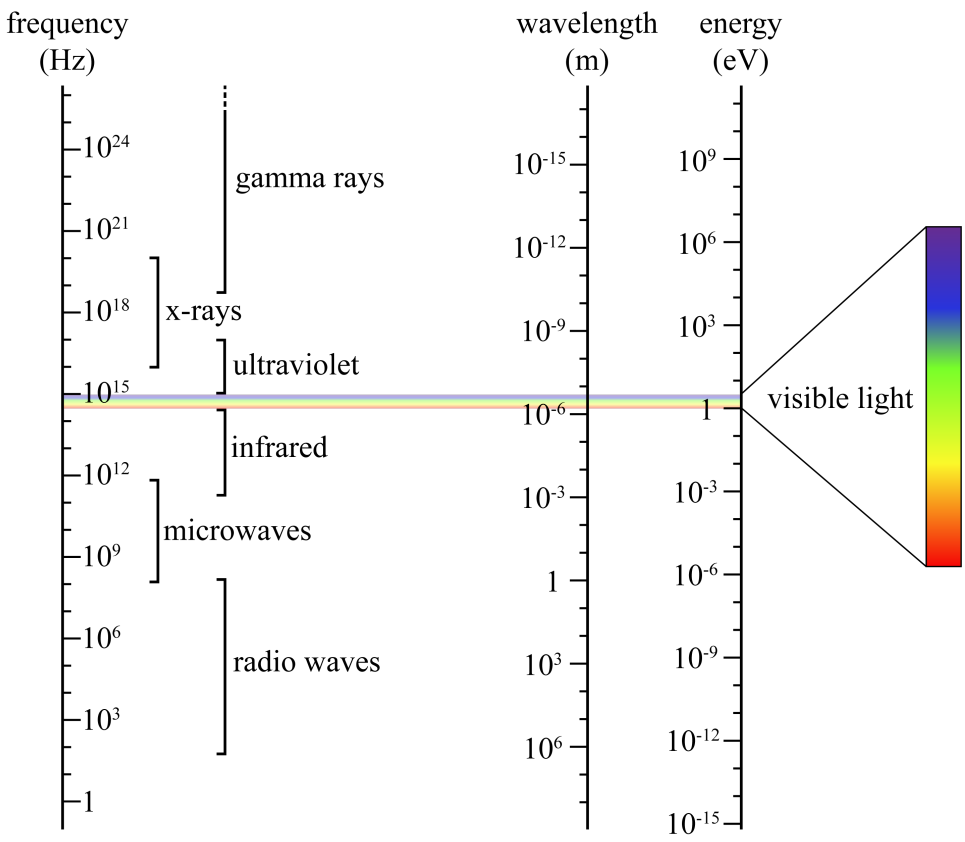

Figure 2.1: Various categorical ranges of the electromagnetic spectrum are shown, according to their frequency (Hz), wavelength (m), and energy (eV). The visible portion of the electromagnetic spectrum corresponds to light with wavelengths between 400-700 nm and energies between 2-3 eV. X-rays correspond to wavelengths of light between 1 μm -10 nm with energies between 100 eV to 100 keV. Adapted from [13].

to produce high-flux x-ray beams with very small footprints ($\sim$10-100 μm) at synchrotron light sources, generally permits samples with dimensions on the order of 100 μm to be easily measured. In contrast, due the high penetration depth and relatively large footprint ($\sim$10 mm) of neutron beams, much larger samples are required and it is generally preferred that the sample has a mass of several grams.

Another important corollary resulting from the disparity of interaction strength with matter (in conjunction with the significantly higher flux available from x-ray sources than neutron sources) is the amount of time that is required to collect data via x-ray scattering versus neutron scattering. Data collection times for neutrons typically range from several minutes to several

hours, which is generally much longer than the collection times for x-rays. At synchrotron light sources, depending on the experimental techniques being used, sub-second data acquisition is often possible with x-rays. In addition to allowing for a more efficient use of experimental time by increasing the throughput of measurements that can be made, the faster data acquisition times also enable time resolved studies, such as pump-probe experiments, in which the sample is first excited (i.e., pumped) by x-rays, a laser, or some other stimulus, and then subsequently measured (i.e., probed) by x-rays in its excited state, necessitating data acquisition timescales that are very short.

The penetration depth, or, conversely, the scattering intensity, of either x-rays or neutrons also depends on the material being studied. More specifically, it depends upon the elemental scattering *cross sections* of the atoms within the sample. While a mathematical description of the scattering (and also absorption) cross sections will be given for x-rays in Section 3.2, for the purposes of the comparison between neutron and x-ray scattering it is sufficient to think of the cross section as the probability amplitude that a scattering event will occur and is strongly dependent upon which element constitutes the scatterer. Similarly, the absorption cross section represents the probability amplitude that an atom will absorb an x-ray or neutron. Cross sections are expressed in units of area (*barns*, specficially, where $1\ b = 10^{-28}\ m^2 = 10^{-24}\ cm^2$), which lends itself to the somewhat useful conceptualization of each scattering (or absorbing) atom as a bullseye-esque "target" in which the relative size of the target is given by that element's cross section. Because x-rays interact with the electron densities, the scattering strength increases greatly as the number of atomic electrons increases. For x-rays

$$\sigma_c \propto Z^2$$

where σ_c is the coherent (i.e., elastic) scattering cross section and Z is the atomic number. This strong Z dependence often makes it challenging to measure scattering signals from lighter

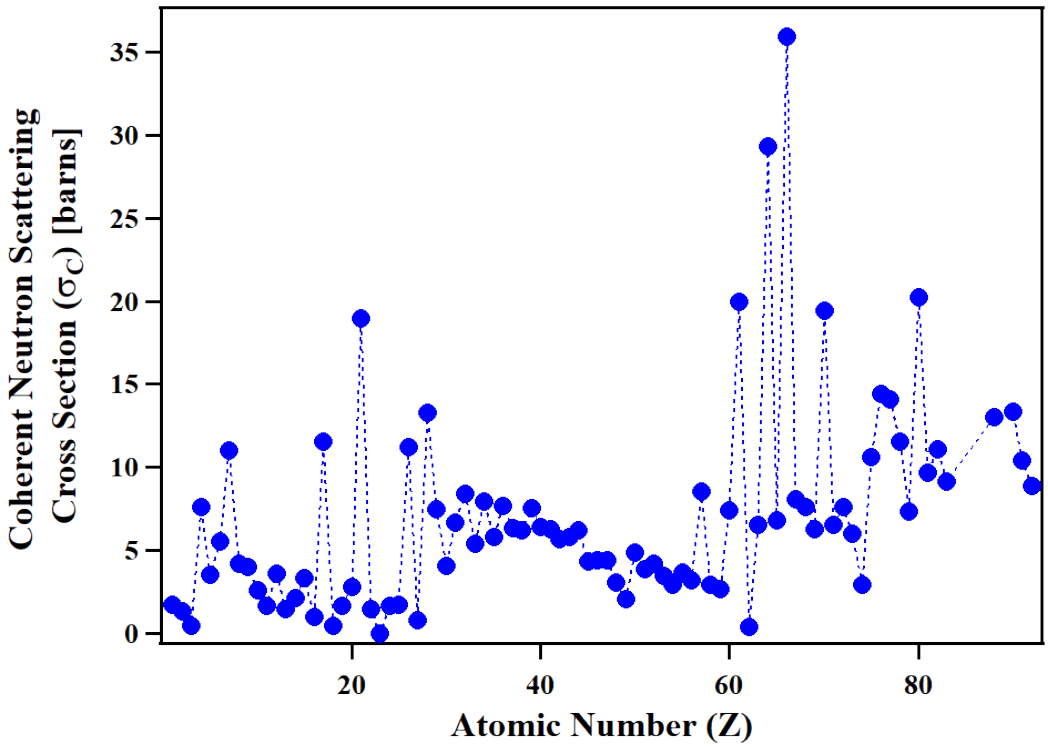

Figure 2.2: The coherent scattering cross section for neutrons is shown for the primary isotope of most elements, up to uranium ($Z = 82$). Adapted from [15].

elements such as hydrogen or oxygen using x-rays[5]. In contrast, the coherent scattering cross section for neutrons do not obey a simple relation to atomic number and appear to vary with Z at random[6], as shown in Figure 2.2, which shows the neutron coherent scattering cross section for the primary isotope of most elements, up to uranium ($Z = 82$) [15].

The disparity between x-ray and neutron scattering cross sections is increasingly apparent upon consideration of the total scattering cross section, which includes both coherent and incoherent contributions. Figure 2.3 illustrates this distinction for a selection of commonly measured elements [16]. Perhaps the most striking difference in x-ray versus neutron cross section is that of hydrogen (H), which has the largest total neutron scattering cross section of any elemental isotope, making neutron scattering far more suitable at detecting H scattering signals than x-rays.

[5]It is also why the heavy element lead is used in protective vests during medical x-rays.

[6]The coherent neutron coherent cross section *is* well understood within the context of quantum chromodynamics, but this is well outside of the scope of this dissertation.

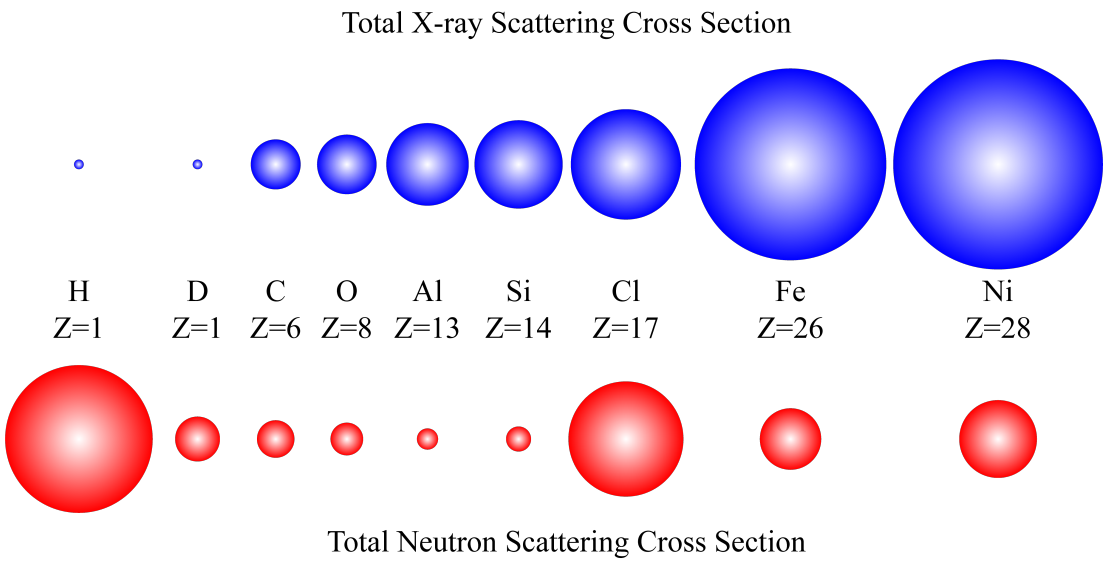

Figure 2.3: The total (coherent + incoherent) scattering cross sections are compared for x-rays and neutrons for a selection of commmonly measured elements. Adapted from [16].

However, incoherent scattering is a major contributor to hydrogen's total neutron scattering cross section. Because this large incoherent scattering cross section significantly raises background levels, it is common to irradiate samples with neutrons in order to convert the H to its isotope deuterium (D). This is favorable because, unlike H, D has a larger coherent scattering cross section than incoherent scattering cross section, even though the total scattering cross section is >10 smaller than for H. Similarly, neutrons are often more suitable than x-rays at measuring oxygen when in the presence of heavy metals (e.g., transition-metal oxides) due to more comparable scattering cross sections for neutrons than for x-rays. Another less straightforward example is lithium, which is difficult to detect with x-rays when heavier elements are present due to its low atomic number ($Z = 3$). However, even though the neutron scattering cross section of lithium is much more comparable to heavier elements than for x-rays, it also has a moderately high neutron absorption cross section. For this reason, neither x-rays nor neutrons are particularly well suited at measuring samples containing lithium, though neutrons are typically considered to be better.

Another contrasting property between x-rays and neutrons is the *atomic form factor*, which describes the scattering amplitude of an x-ray, neutron, or other wave by an isolated atom.

The atomic form factor, f, is a function of the *momentum transfer* between the incident and scattered beam, $\mathbf{Q}$. While $\mathbf{Q}$ will be more rigorously defined in Section 3.2, for the purpose of comparing the x-ray and neutron form factors, it is sufficient to define only the magnitude of $\mathbf{Q}$ as

$$|\mathbf{Q}| = 4\pi\frac{sin(\theta)}{\lambda}$$

where λ is the wavelength of the incident and scattered x-ray or neutron (the scattering process is assumed to be elastic) and θ is defined as the angle between the scattered x-ray or neutron and the sample plane (or, equivalently, half of the angle between the incident and scattered x-ray or neutron wavevectors). The most important feature of this relation to note is that $|\mathbf{Q}|$ increases with the angle of the scattered x-ray or neutron. We will see in Section 3.2 that the atomic form factor $f(\mathbf{Q})$ involves a Fourier transform of the spatial density distribution of the scattering atom. For x-rays, the atomic form factor falls off at large $|\mathbf{Q}|$, as shown in Figure 2.4 [17], due to destructive interference between electrons within the scattering atom. Neutrons, however, scatter from the atomic nuclei, which are so small relative to the spacing between atoms and the wavelength of the incident neutrons that its spatial density distribution may be treated as an infinitesimal point (i.e., delta function). Because the Fourier transform of a delta function is unity, neutrons have a constant atomic form factor for nuclear scattering. Although the amplitude value depends on the isotope of the scattering nucleus, the scattering amplitude does not vary with $|\mathbf{Q}|$. This is not true, however, for magnetic scattering by neutrons, which do scatter from the electron charge densities of the scattering atom, therefore yielding an atomic form factor that is similar to that of x-rays. A key difference in the scattering of x-rays and the magnetic scattering of neutrons is that x-ray scattering is weighted heavily by the core electrons, whereas neutrons only scatter from the unpaired electrons in the outer shell. The scattering electron distribution is therefore more diffuse for neutron magnetic scattering than for x-rays, resulting in an atomic form factor which decays more rapidly.

As a final practical consideration between x-ray and neutron scattering experiments, the

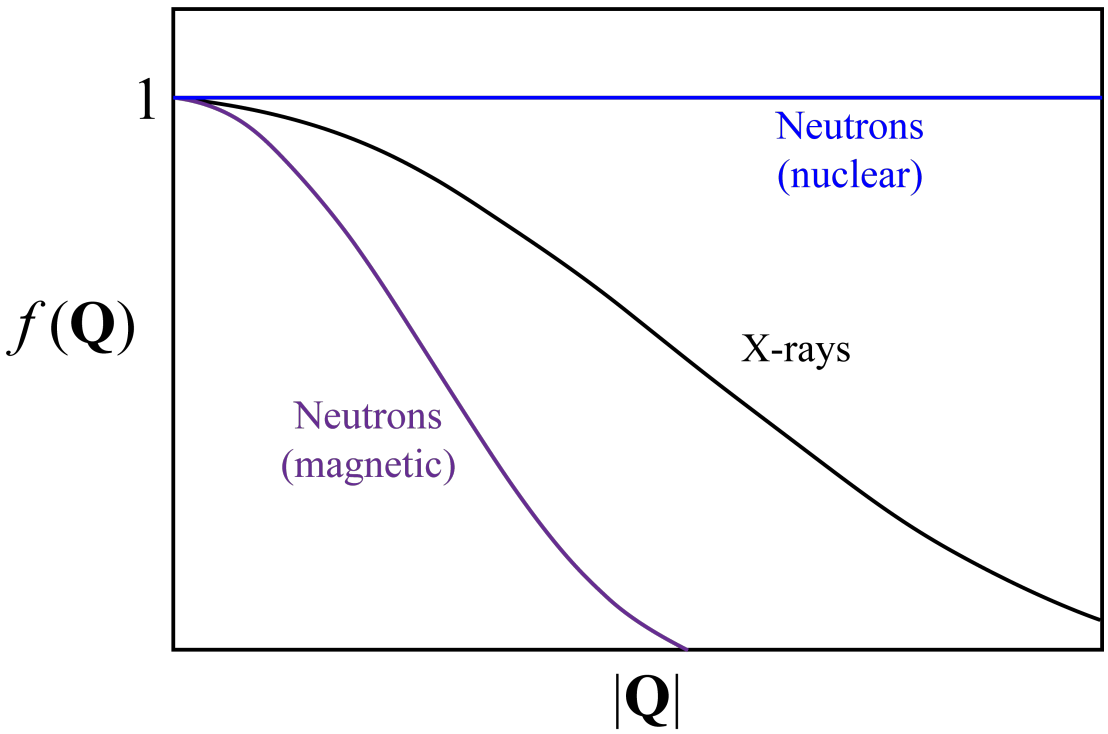

Figure 2.4: The normalized functional forms of the atomic form factors for x-ray and neutron scattering are plotted as a function of $|\mathbf{Q}|$. Adapted from [17].

sample destructiveness of each probe will be compared. Both x-rays and neutrons are highly advantageous probes in this regard, as both are generally considered to be non-destructive techniques; however, this is not without caveats for both x-rays and neutrons. While it is true that x-rays are generally non-destructive, especially for most samples being measured within the scope of condensed matter physics and material science, it ultimately depends on the material composition and geometry of the sample, as well as the energy and intensity of the x-ray beam. It is certainly possible for the x-ray beam to destroy a sample under the right circumstances[7]. With neutron scattering experiments, one does not typically need to worry about the sample being destroyed, but rather with the sample becoming radioactive. This occurs when atomic nuclei within the sample absorb some fraction of the incident neutrons, resulting in the formation of

[7]I learned this the hard way when a highly focused, high-energy x-ray beam cut through a thin sample of single-crystal $YBa_2Cu_3O_7$ during an inelastic x-ray scattering experiment. The takeaway from this lesson is, if during an experiment your data suddenly becomes abnormal with no obvious explanation, consider checking on your sample.

different isotopes. If these isotopes are unstable, this may result in your sample being held for some period of time following the experiment before it can be safely returned. This effect is highly dependent on the material composition of the sample and, if certain elements are present (e.g., cobalt), the sample will never be returned.

This concludes the review of the relevant properties of x-rays and the characteristics of using them to investigate matter. It is hoped that these fundamental principles have been acutely elucidated by contrasting x-rays to neutrons as a probing source. Furthermore, it is hoped that the reader has obtained a basic knowledge about these two particles that will encourage consideration of utilizing both x-rays and neutrons to obtain complimentary information about their material systems. The focus will now be turned solely to x-rays for the remainder of this dissertation.

2.3 X-ray Generation

2.3.1 History

X-rays were first discovered by Wilhelm Conrad Röntgen in 1895 [18] at the University of Würzberg, Germany while using a Geissler tube, which is essentially a partially evacuated glass cylinder with electrodes on either end that contains a conductive fluid, such as neon or argon. When a sufficiently large voltage is applied to the electrodes, the resulting electric current flows along the tube as it ionizes the molecules in the conductive fluid. As the disassociated electrons and ions recombine, photons are emitted via fluorescence, operating similarly to a modern neon lamp. The color or wavelengths of light emitted by the Geissler tube varies with choice of conductive fluid, depending on the separation of electron energy levels of that particular material. Using a fluorescent screen to detect these emitted photons, Röngten was surprised to discover that the photons were still observed when the detector was obscured from the Geissler tube by either paper or wood, but not by metal or *bones*, as shown in Figure 2.5, which depicts the first published medical x-ray, taken by Röntgen of the left hand of his wife, Anna Bertha Ludwig.

Figure 2.5: Upon discovering x-rays in 1895, Wilhelm Röntgen performed the first medical x-ray of the left hand of his wife, Anna Bertha Ludwig. Reproduced from [19].

These mysterious observations led Röngten to designate them as *x-rays* after the commonly used algebraic variable x, implying that it was an unknown form of radiation, which we now know are simply photons with energies within a specific range, as shown in Figure 2.1.

2.3.2 Modern X-ray Sources

While Geissler tubes are no longer used today, the most common x-ray sources, such as those found in many labs, still consist of a cathode and anode with a high voltage placed across them, as shown in Figure 2.6. However, rather than passing an electric current through a conducting fluid, the cathode and anode are separated by vacuum. The electric field resulting

from the large potential difference causes electrons to boil off of the cathode and accelerate towards the anode. As these accelerated electrons collide with the anode, electrons bound to the atoms within the anode are excited and consequently fluoresce, emitting x-ray photons with specific, characteristic wavelengths. Just as the wavelength of emitted light depended upon the choice of conductive fluid within the Geissler tube, the wavelength of x-rays emitted from these modern x-ray sources depends upon the material choice of the anode. Because the anode must be metallic, in order to be electrically conductive, and have a reasonably high melting point, in order to withstand the Joule heating produced by the application of very high voltages, the choice of anode material is limited. Copper is the most prevalent anode material because it produces the shortest wavelength of x-rays that is greater than 1 Å that is highly suitable for studying a very wide range of materials (using too small of wavelength x-rays results in weak scattering and contracts diffracted patterns to smaller Bragg angles, while using too large of wavelength x-rays suffers from poor penetration depth and limits the range of accessible Bragg reflections), but chromium, iron, cobalt, molybdenum, and silver are also commonly used and the most suitable choice of anode ultimately depends on the material being studied. For example, cobalt, iron, and, to a lesser extent, manganese all fluoresce significantly when illuminated by a copper x-ray source, resulting in elevated background levels and a reduced signal-to-noise ratio.

When x-rays are generated by this method, more than one wavelength is present. When charged particles, such as electrons, accelerate or decelerate, they generate changing electric and magnetic fields that propagate as electromagnetic waves, manifesting as photons. As the electrons emitted by the cathode impinge upon the anode, they rapidly decelerate, producing a continuous spectrum of photons, called *bremsstrahlung radiation* (a German term which roughly translates to *braking radiation*). The maximum, or cut off, energy of this spectrum is dependent upon the magnitude of the electric potential difference between the cathode and anode. This continuous spectrum is generally considered as background and a nuisance for standard laboratory x-ray sources but, as will be discussed in the following section, is crucial to the production of x-rays

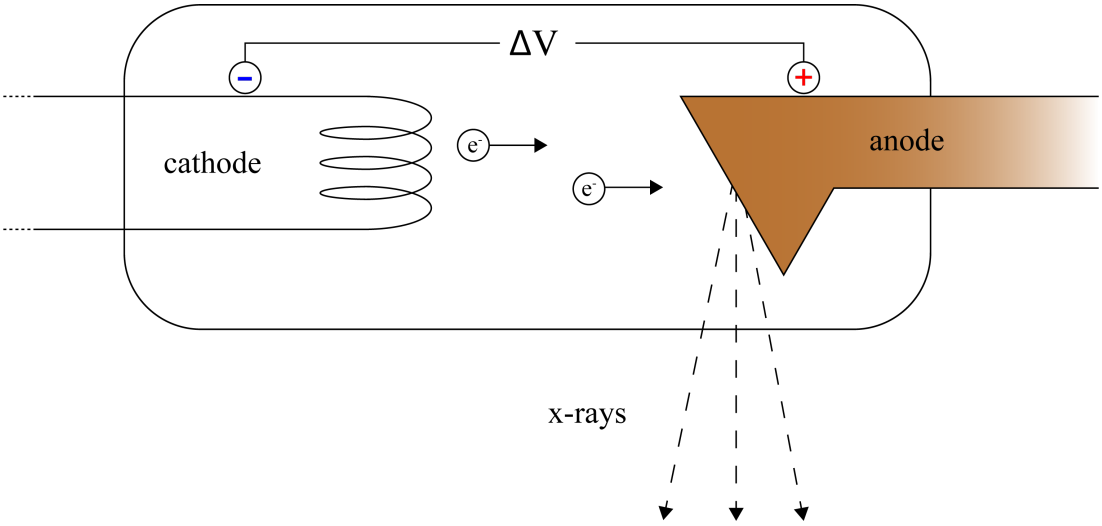

Figure 2.6: A schematic of a modern x-ray source consisting of a cathode and anode inside of an evacuated chamber. When a large enough voltage is applied, electrons are boiled off of the cathode and accelerated towards the anode. These electrons collide with and excite the atoms within the anode. These excited atoms are unstable and consequently fluoresce, generating x-rays.

generated by synchrotron sources. Overlaying this continuous background are multiple peaks at discrete energies produced by the fluorescing anode. The electrons which collide with the anode have enough energy that core electrons in the anode are excited into unbound states. The resulting core hole is not stable and is quickly filled by electrons in higher energy levels, according to the dipole selection rules. Because the anode materials have ground state electronic structures consisting of multiple occupied energy levels, there are multiple electronic transitions available to collapse into the unstable core hole. Each of these different transitions produces an x-ray with a unique and discrete energy corresponding to the difference in energy between each of the transitional states.

These discrete x-ray emission spectra are named using *Siegbahn* notation. In this notation, the principal quantum number (n) of the innermost shell involved in the electronic transition is represented by a capital letter, beginning with K for $n = 1$, L for $n = 2$, M for $n = 3$, and so on. The various transitions to this states within each shell are denoted with a Greek letter as a subscript, in addition to sometimes a number as a subscript to the Greek letter. Confusingly,

the Greek letter and number provide no information about the higher-energy electronic state involved in the transition and are instead listed in order of highest observed intensity [20]. Since this nomenclature is unsystematic and difficult to learn, in addition to suffering from the issue that various transitions have been observed since the introduction of the Siegbahn notation in the 1920's which have not been named within this notation, an improved nomenclature has been established by the International Union of Pure and Applied Chemistry (IUPAC), called *IUPAC notation*. We will see in Chapter 3 that this is the notation commonly used for most modern x-ray techniques, such as in x-ray absorption spectroscopy. A complete table of the IUPAC notation for electronic states up to $n = 4$ can be found at the end of Section 3.1. Nevertheless, Siegbahn notation is still the most common nomenclature used when referring to the emission lines of standard laboratory x-ray sources. These transitions are depicted in Figure 2.7 [21], though it is likely sufficient to commit only the K_α ($2p \rightarrow 1s$) transition to memory, as this is generally the emission that is used for x-ray experiments performed with standard laboratory x-ray sources due to being the highest intensity.

Because $2p$ electronic states may have two possible values of total angular momentum (j) with slightly different energies, the K_α emission line actually contains a fine structure consisting of two emission lines separated by slightly different energies associated with each of these transitions. K_{α_1} corresponds to the higher energy $2p_{\frac{3}{2}} \rightarrow 1s$ transition, while K_{α_2} corresponds to the lower energy $2p_{\frac{1}{2}} \rightarrow 1s$ transition. The K_{α_1} emission line is typically twice as intense as the K_{α_2} emission line. This is because the multiplicity of electronic states, given by the formula $2j+1$, of the K_{α_1} ($j = \frac{3}{2}$ initial state) transition is double that of the K_{α_2} ($j = \frac{1}{2}$ initial state) transition. However, it is common not to distinguish between these fine structured emissions and simply refer to their sum as K_α, largely due to the energy difference between the emissions being so small that many standard laboratory x-ray setups are unable to resolve them separately. A typical spectrum produced by a modern x-ray source containing each of these features is shown in Figure 2.8.

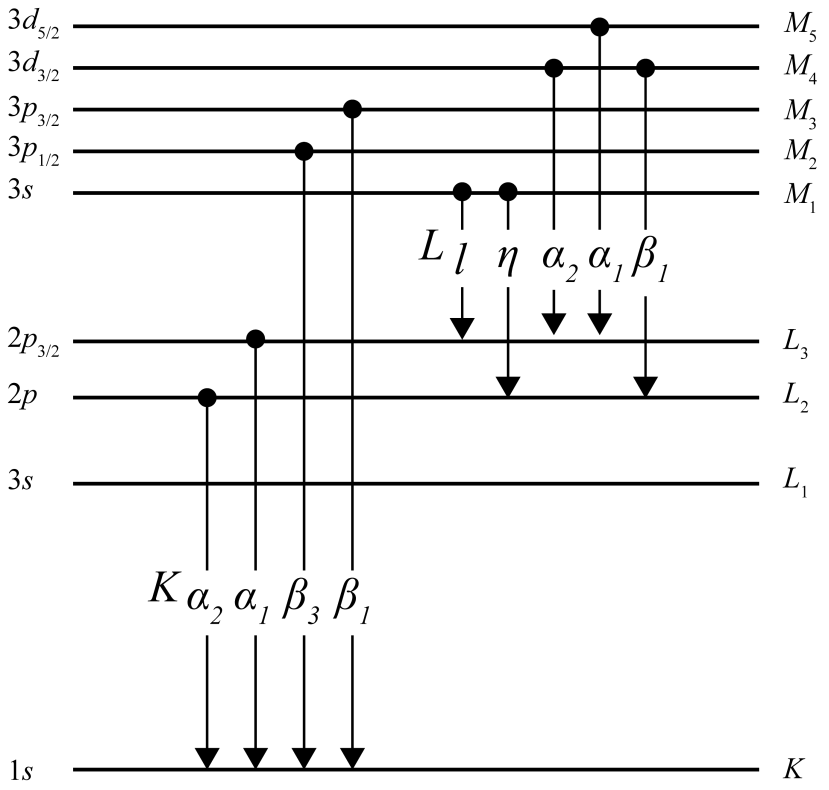

Figure 2.7: A diagram illustrating the Siegbahn notation for some common transitions between electronic states alongside the modernized IUPAC notation. Adapted from [21].

The energies of x-rays emitted by these electronic transitions can be calculated using Moseley's law [22]

$$E = E_i - E_f = \frac{m_e q_e^2 q_Z^2}{8h^2\varepsilon_0^2}\left(\frac{1}{n_f^2} - \frac{1}{n_i^2}\right)$$

where m_e is the electron mass, h is Planck's constant, ε_0 is the permittivity of free space, n_i and n_f are the initial and final electronic energy levels, respectively, q_e is the elementary charge, and q_Z is the effective charge of the nucleus, given by

$$q_Z = (Z - b)q_e$$

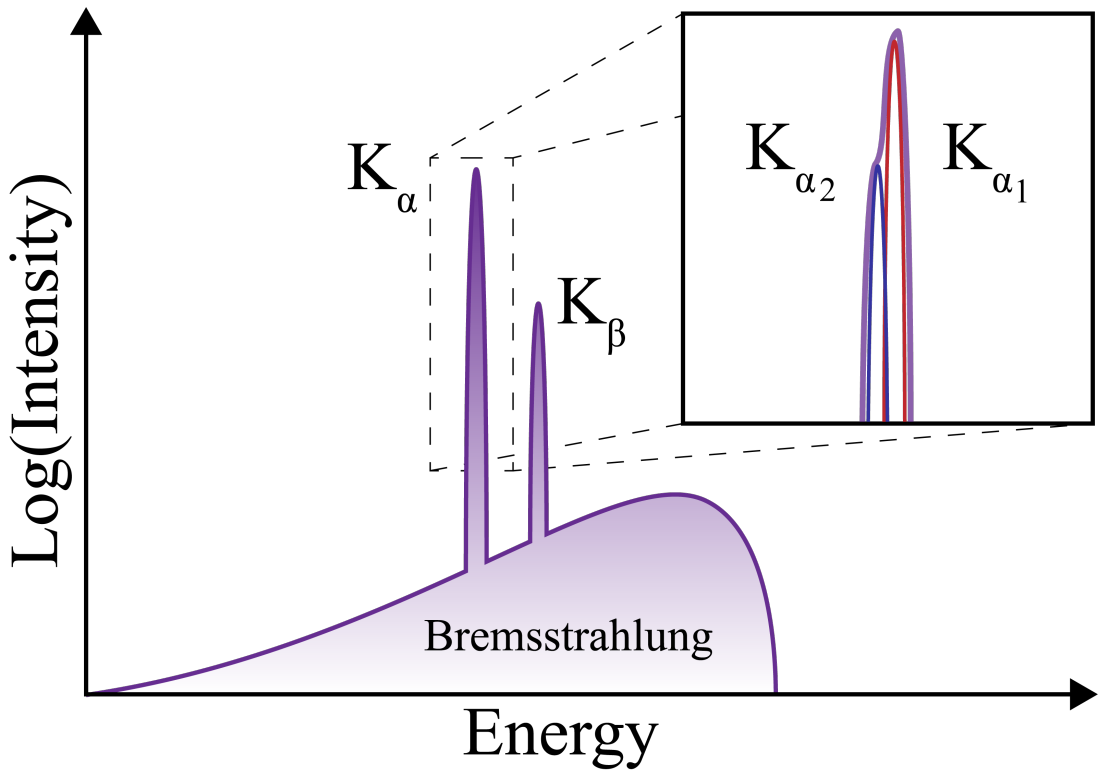

Figure 2.8: A typical spectrum of x-rays produced by a modern x-ray source plotted with the log of the intensity versus the energy of emitted x-rays. The deceleration of electrons impinging upon the anode produces a continuous spectrum of bremsstrahlung radiation with a maximum cut off energy that depends upon the magnitude of voltage applied between the cathode and anode. The discrete K_α and K_β emissions result from electronic $2p \rightarrow 1s$ and $3p \rightarrow 2s$ transitions, respectively. An inset shows that the fine structure of the K_α emission is composed of K_{α_1} (red) and K_{α_2} blue emissions, which correspond to electrons transitioning from the $2p$ states with total angular momenta of $j = \frac{3}{2}$ and $j = \frac{1}{2}$, respectively.

where Z is the atomic number and b is an empirically measured constant that accounts for screening of the nuclear charge. For the most commonly used case of K_α emissions, Moseley's law reduces to

$$E = E_i - E_f = \frac{m_e q_e^4}{8h^2\varepsilon_0^2}\left(\frac{1}{1^2} - \frac{1}{2^2}\right)(Z-1)^2 \approx \frac{3}{4}(Z-1)^2 \times 13.6 \text{ eV}$$

While standard laboratory x-ray sources have improved significantly over the decades since Röntgen's initial discovery, even the most modern sources continue to suffer from some

major limitations. The intensity of standard x-ray sources is limited by the ability to dissipate heat from the anode that is generated by the large power drawn from the application of high voltages. Furthermore, x-rays are emitted from the anode isotropically and only a very small fraction of the x-rays emitted into the 2π solid angle can be utilized for performing measurements. The wavelengths of x-rays produced by standard sources are not tunable and only exist for very specific values determined by the electronic energy structure of the limited choice of materials that are suitable for use as an anode. In the following section, we will see how synchrotrons offer significant advantages over standard laboratory x-ray sources.

2.3.3 Synchrotrons

A synchrotron colloquially refers to a large facility that generates intense beams of x-rays which are produced by applying magnetic fields to charged particles traveling around a circular ring at relativistic speeds. Technically, only one stage within the facility is truly considered to be a synchrotron and it is not the stage from which x-rays are produced, so referring to the entire facility as a synchrotron is a bit of a misnomer. Synchrotrons are also commonly used as a component within particle colliders, such as at CERN, but this dissertation will refer specifically to the facilities whose principle purpose is the production of light. These so-called light sources typically consists of multiple stages, as shown in Figure 2.9. The charged particles must first be produced and electrons constitute the most simple option, typically being produced either by thermionic emission (i.e., heating a piece of metal) or by applying a laser pulse to a photo-cathode. Consequently, electrons are by far the most commonly used charged particle for this application and will be solely referred to through the remainder of this dissertation, however positrons are also sometimes used, such as at the Photon Factory at the High Energy Accelerator Research Organization (KEK) in Japan, for example (protons are not very suitable for light-producing applications due to being roughly 2000 times more massive than the electron but are utilized in particle collider applications, such as in the synchrotron used at CERN).

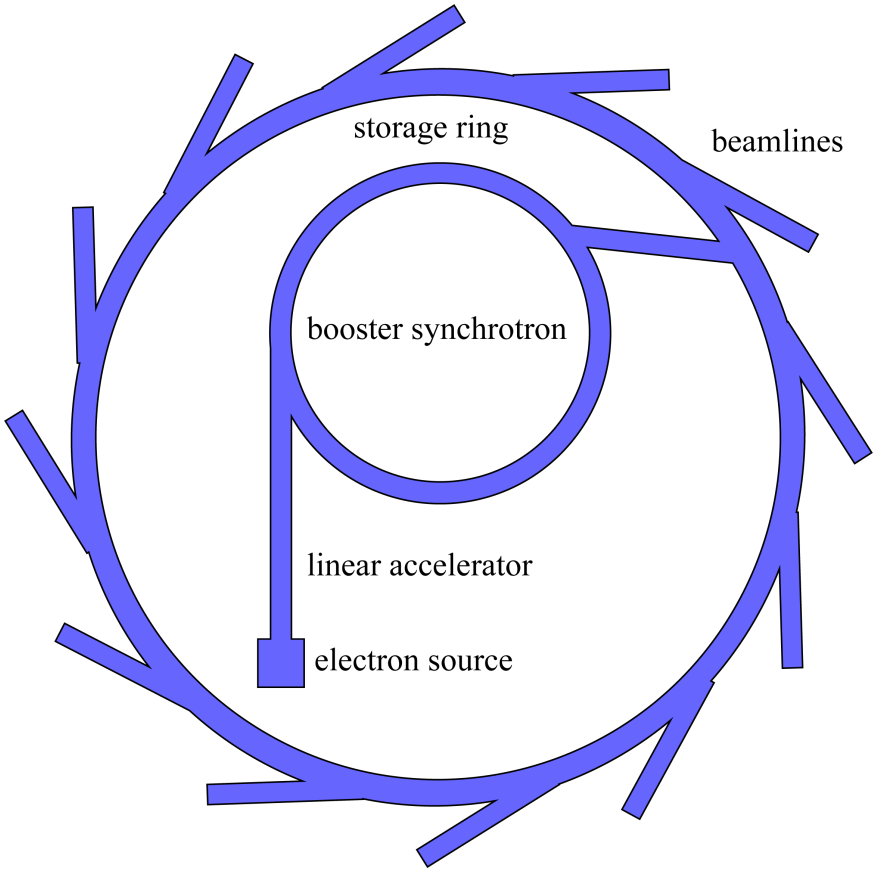

Figure 2.9: A typical layout of a synchrotron light source. An electron source produces bunches of electrons, which are accelerated from rest up to energies of ∼0.5 GeV in a linear accelerator. The electrons are then accelerated up to energies of typically 3-12 GeV in a booster synchrotron. The electrons are then injected into a storage ring, which keeps them at constant energy. Insertion devices located within the storage ring cause the electron bunches to produce beams of x-rays along the beamlines to be utilized for performing experiments.

Once the electrons have been produced, which are typically done in bunches, the first main stage in a light source is a linear accelerator (or linac) whose primary purpose is accelerating the electrons from rest up to energies of roughly 0.5 GeV using high-voltage alternating electric fields. These electrons are often sent to an accumulator ring which compresses the electron bunch into a shorter pulse. The electron bunches are then injected into the next stage, which is the actual synchrotron. It is a racetrack-shaped ring of electromagnets with the purpose of boosting the energies of the electrons from ∼0.5 GeV to typically between 3-12 GeV for most modern facilities. Radio frequency (rf) cavities are used to accelerate the electrons and bending

and focusing magnets are used to maintain their orbital path. Once the electrons have been accelerated to their target energy, they are injected from the booster synchrotron into the storage ring, which is a circular ring where the electrons are kept at constant energy. The storage ring can be quite large, often with circumferences in excess of 1 kilometer, and is enclosed within thick layers of concrete shielding to protect the light source users, who are generally working in the experiment hall located just outside of the storage ring, from harmful radiation. At various locations around the storage ring, bending magnets and insertion devices are used to deflect the electron bunches from their orbital path and cause them to produce synchrotron radiation. The generated synchrotron radiation is directed towards a beamline, which contains one or more endstations where synchrotron users are able to conduct experiments. There may be dozens of beamlines, depending on the facility, and each is equipped with specialized crystal and/or mirror optics that selects out the photon energies required for their specific type of experiment. Each endstation typically contains additional optics to analyze the absorption, scattering, or imaging process, as well as detectors for collecting data generated by interactions between the x-ray beam and sample being studied.

While there are many types of insertion devices, one of the most common is called an *undulator*. As shown in Figure 2.10, an undulator consists of two rows of alternating permanent magnets that are separated by a small gap. As the electrons travel through this gap between the magnet arrays, the alternating magnetic field causes the electron trajectories to oscillate and emit synchrotron radiation. The term *synchrotron radiation* specifically refers to magnetobremsstrahlung radiation (i.e., bremsstrahlung radiation resulting from acceleration due to magnetic fields) from ultrarelativistic (i.e., kinetic energy $\gg mc^2$) charged particles[8]. Because the electrons are moving at such highly relativistic speeds where $v \approx c$, the emitted synchrotron radiation is collimated within a cone of angle

[8]Magnetobremsstrahlung radiation is called *gyro radiation* when emitted by non-relativistic (i.e., $v \ll c$) particles and called *cyclotron radiation* when emitted by mildly relativistic (i.e., kinetic energies are comparable to mc^2) particles.

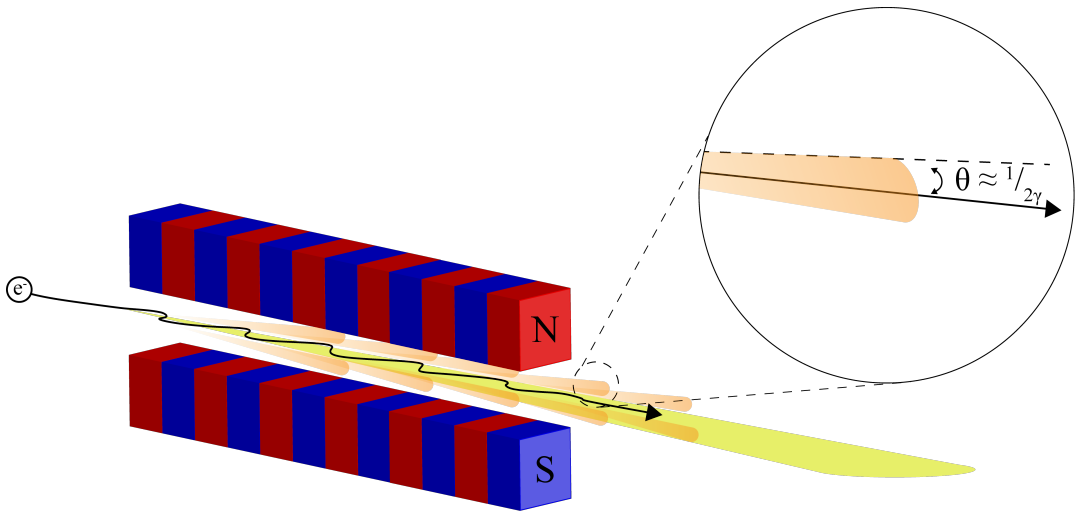

Figure 2.10: An undulator insertion device consists of two periodic arrays of permanent magnets separated by a gap. As electrons travel through this gap between the magnet arrays, their alternating magnetic fields cause the electron trajectory to oscillate and emit synchrotron radiation. Adapted from [23].

$$\theta \approx \frac{1}{2\gamma}$$

where γ is the Lorentz factor, defined as

$$\gamma = \frac{1}{\sqrt{1 - \frac{v^2}{c^2}}}$$

As of 2023, the Advanced Photon Source at Argonne National Laboratory utilizes a ring current where the electrons are traveling at energies of 7 GeV [24], which corresponds to velocities $>$99.999999% of the speed of light. Using the relation $\gamma = \frac{E}{m_e c^2}$, where the electron rest energy $m_e = 0.511$ MeV, this yields a Lorentz factor of $\gamma \approx 13,700$, resulting in a collimation angle of $\theta \approx 0.04$ mrad. Compared to standard laboratory x-ray sources that emit x-rays isotropically, this illustrates how tremendously more efficient synchrotrons are at utilizing a much larger fraction of its generated x-rays by collimating them within a narrow beam. Additionally, synchrotrons are able to produce a significantly larger number of photons per second, both overall and within a

given energy range, because they do not suffer from the same power limitations of standard x-ray sources as there is no anode that must be cooled. The amount of synchrotron radiation that can be produced is instead most significantly limited by the magnitude and cross-section of the beam current that can be sustained within the storage ring, which is limited by the number of electrons that can be bunched together (due to Coulomb repulsion between electrons within each bunch) and the impedance of the vacuum chamber [25]. All of these factors are captured by a quantity called the *brilliance* [11], which is defined as

$$\text{brilliance} = \frac{\text{photons/second}}{(\text{mrad})^2(\text{mm}^2 \text{ source area})(0.1\% \text{ bandwidth})}$$

This quantity characterizes the amount of photons per second within a spectral energy range, which is defined, by convention, as a fixed relative energy bandwidth of 0.1%, while also accounting for the beam divergence and cross section of the source and offers the most straightforward way of comparing both the intensity and directionality of x-ray beams.

The final characteristic of x-ray beams that will be discussed is *coherence*. As depicted in Figure 2.11, X-ray beams are commonly described as transverse electromagnetic waves where the electric and magnetic fields oscillate perpendicular to each other and to the direction of propagation, according to the relation

$$\boldsymbol{E} \times \boldsymbol{B} = \boldsymbol{k}$$

where $\boldsymbol{E}$ is the electric field, $\boldsymbol{B}$ is the magnetic field, and $\boldsymbol{k}$ is the wavevector, which is related to its wavelength by the relation

$$k = \frac{2\pi}{\lambda}$$

The electric field, which varies with both space and time, is often described as a plane wave (i.e., as having constant amplitude in the plane perpendicular to the direction of propagation)

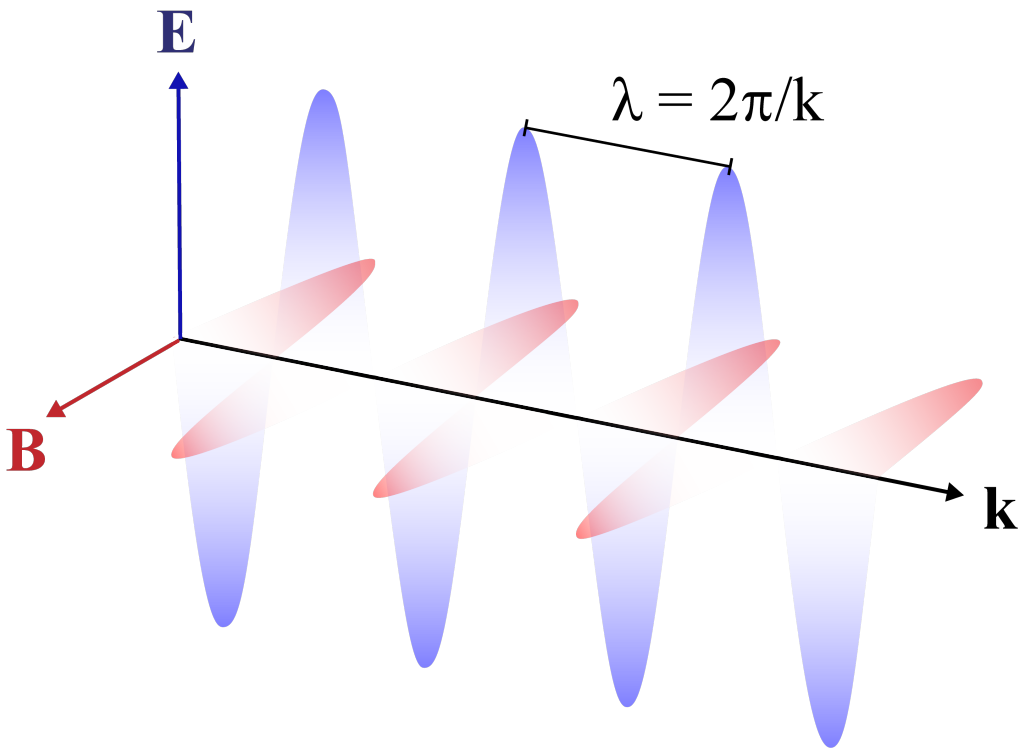

Figure 2.11: A transverse electromagnetic wave describing an x-ray. The electric field, $\boldsymbol{E}$, and magnetic field, $\boldsymbol{B}$, oscillate perpendicular to each other and also to the direction of propagation, $\boldsymbol{k}$.

with the relation

$$\boldsymbol{E}(\boldsymbol{r},t) = E_0 e^{i(\boldsymbol{k}\cdot\boldsymbol{r}-\omega t)}\hat{E}$$

where E_0 is the amplitude of the electric field, $\hat{E}$ is the direction of polarization, t is time, and ω is the angular frequency, which is related to the period of oscillation by the relation

$$\omega = \frac{2\pi}{T}$$

Quantization of the electromagnetic field yields photons with energy and momenta according to the relations

$$E = \hbar\omega$$

$$\boldsymbol{p} = \hbar\boldsymbol{k}$$

where E is energy, $\boldsymbol{p}$ is momentum, and $\hbar$ is the reduced Planck constant. While this plane wave description of an x-ray beam is straightforward and useful for many applications, it is ultimately an idealization because it defines x-ray beams as: *i*) being perfectly monochromatic and *ii*) having a perfectly well-defined direction of propagation. Another way to state this is that the plane wave state describes an x-ray beam which is perfectly coherent. The deviations of a real x-ray beam from this idealization is therefore described by its *coherence length*.

Consider two plane waves traveling in the same direction, $\hat{\boldsymbol{k}}$, but with slightly different energies or wavelengths, λ and $\lambda - \Delta\lambda$, as shown in Figure 2.12 [11]. Initially, the maximum amplitude of both waves are aligned such that their relative phase, $\Delta\phi$, is zero and the two waves are said to be in phase. Due to the difference in wavelengths between these two waves, there is eventually a point along their path of propagation where the maximum amplitude of one wave coincides with the minimum amplitude of the second wave such that $\Delta\phi = \pi$ and the two waves become fully out of phase with each other. As the waves continue to propagate, another point is reached where they become in phase again. The distance required for the two waves to lose their phase coherence (i.e., change from being in phase to being fully out of phase) is called the *longitudinal* coherence length, L_L. If that distance spans N wavelengths for the first wave and $N + \frac{1}{2}$ wavelengths for the second wave, we obtain the relation

$$L_L = N\lambda = (N + \frac{1}{2})(\lambda - \Delta\lambda)$$

Expanding the right side of this equation yields

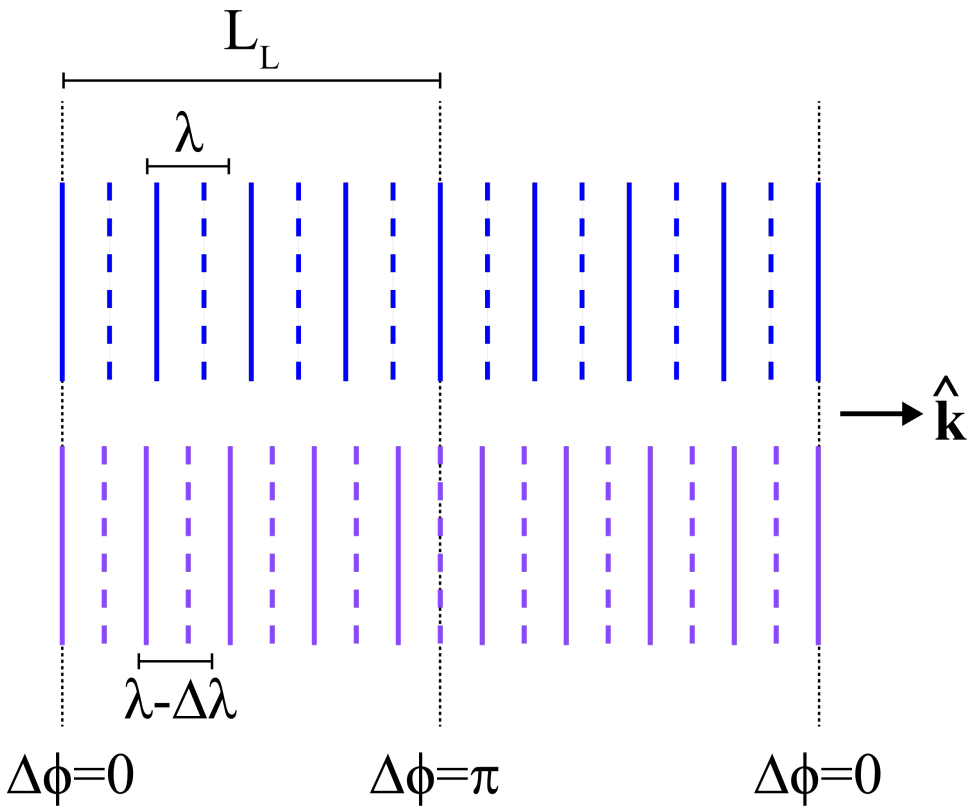

Figure 2.12: Two plane waves are traveling in the same direction, $\hat{\boldsymbol{k}}$, but with slightly different wavelengths, λ (blue) and $\lambda - \Delta\lambda$ (purple). At the initial point of propagation, the amplitudes of both waves are at their maxima (solid lines), indicating that the two waves are in phase ($\Delta\phi = 0$). As the waves propagate, the maximum amplitude of one wave eventually coincides with the minimum (dashed lines) of the second wave, indicating that they are fully out of phase ($\Delta\phi = \pi$). The longitudinal coherence length, L_L, is defined to be the distance required for the two waves to change from being in phase to fully out of phase with each other. Adapted from [11].

$$N + \frac{1}{2} = \frac{\lambda}{2\Delta\lambda}$$

Because it is assumed that $\Delta\lambda \ll \lambda$, the waves must propagate over many wavelengths before they become out of phase, such that $N \gg \frac{1}{2}$, implying that

$$N \approx \frac{\lambda}{2\Delta\lambda}$$

Substituting this relation into the definition for the longitudinal coherence length yields [26]

$$L_L \approx \frac{\lambda^2}{2\Delta\lambda}$$

While this example is illustrated for two waves of varying wavelength, real x-ray beams typically consist of a continuous spectrum of wavelengths about some primary value, λ. When calculating the longitudinal coherence length of a real x-ray beam, $\Delta\lambda$ is taken to be the bandwidth of this spectrum. The degree of longitudinal coherence that is required for an experiment depends on its application. It is often the case that the x-ray beam will be filtered by a monochromator to further decrease $\Delta\lambda$. This finite coherence resulting from a lack of monochromaticity can be equivalently described as a *coherence time*, τ, which instead describes the period of *time* over which an x-ray beam maintains its phase coherence, which can be obtained from its frequency spectrum and is defined to be [11]

$$\tau = \frac{1}{\Delta\nu} \approx \frac{L_L}{c}$$

where $\Delta\nu$ is the *frequency* bandwidth of the x-ray beam. As shown, it can also be obtained by dividing the longitudinal coherence length by the speed of light, c, implying that the longitudinal coherence length is truly a measure of temporal coherence, rather than spatial.

Similarly, consider two waves with the same wavelength, λ, that are emitted from two points on a source that are separated by a distance, d, as shown in Figure 2.13 [11]. At some observable point located a distance, D, from the source, the two waves will be traveling in slightly different directions separated by an angle, θ. Due to the difference in the directions of propagation between the two waves, there will be a point on the wavefront where the maximum amplitude of the two waves coincide, indicating that they are in phase, as well as a point on the wavefront where the maximum amplitude of one wave coincides with the minimum of the other wave, indicating that they are fully out of phase. This lateral separation over which the coherence of the wavefront is maintained is called the *spatial coherence length*, L_S. The triangle formed by these

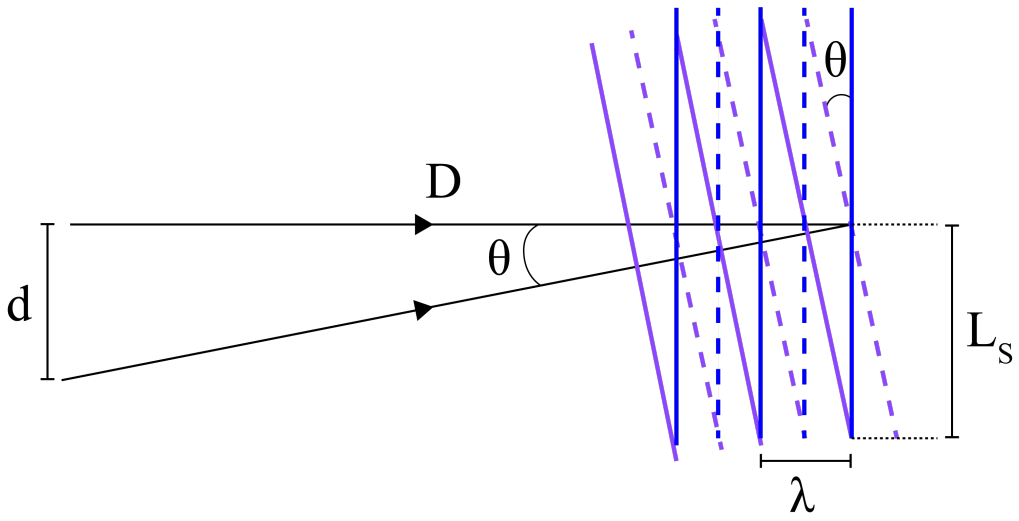

Figure 2.13: Two plane waves with the same wavelength, λ, are emitted from two points on the source that are separated by a distance, d. At some observable point located a distance, D, from the source, the two waves are traveling in slightly different directions, separated by an angle, θ. The spatial coherence, L_S, is defined to be the lateral distance between the points from where the waves are in phase (the maximum (solid lines) amplitudes coincide) to the point where the the waves are out of phase (the maximum amplitude of one wave coincides with the minimum (dashed lines) of the other wave). Adapted from [11].

coincident waves yields the relation

$$L_S = \frac{\lambda}{2\theta}$$

From the triangle formed by the emission points on the source to the observation point we obtain the relation

$$\theta = \frac{d}{D}$$

Substituting this relation into the definition for the spatial coherence length yields [11]

$$L_S = \frac{\lambda D}{2d}$$

This quantity describes the spatial extent to which the wavefront of the x-ray beam is coherent and places an upper limit on the separation between two objects from which interference effects may be produced.

Chapter 3

Experimental X-ray Techniques

3.1 X-ray Absorption Spectroscopy

As discussed in Chapter 2, when an x-ray is incident upon a material, it interacts directly with the electrons within the material and does so in one of two ways, through either: *i*) absorption or *ii*) scattering. Experimental techniques based upon the absorption of x-rays will be discussed first, partly because it is more straightforward to do so in the sense that the notion of directionality is *mostly* irrelevant in absorption experiments, thereby not requiring the inclusion of crystal structures or reciprocal spaces, but more importantly absorption will be discussed first because doing so will be relevant to later discussions of scattering techniques which involve resonance.

Consider an x-ray beam with an initial intensity, I_0, that is incident upon a sample of some material along the x axis, as shown in Figure 3.1. As the x-ray beam penetrates through the material, some of the x-rays will be absorbed, thereby attenuating the beam intensity, $I(x)$, as it continues to propagate. This absorption is characterized by a linear absorption coefficient, μ. The absorption coefficient is related to the absorption cross section, σ_a by the following equation [11]

$$\mu = \rho_{at}\sigma_a = \left(\frac{\rho_m N_A}{M}\right)\sigma_a$$

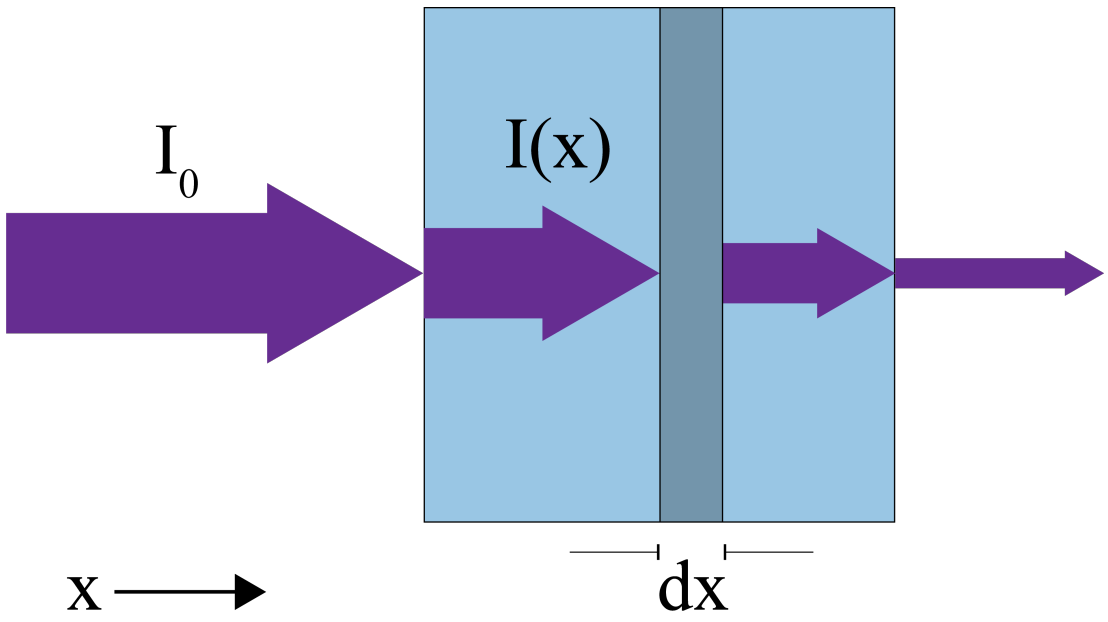

Figure 3.1: An x-ray beam of intensity I_0 is incident upon a sample. As the x-ray beam propagates through the sample along the x direction, it's intensity, $I(x)$, becomes attenuated due to absorption. Adapted from [11].

where ρ_{at} is the atomic number density, ρ_m is the mass density, M is the molar mass, and N_A is Avogadro's number. Similar to the scattering cross sections discussed in Chapter 2, the absorption cross section, and therefore also the the absorption coefficient, vary with both atomic number, Z, and the energy of the incident x-rays. In this case [11]

$$\sigma_a \propto Z^4$$

The energy dependence of the absorption cross section is more complex and will be discussed shortly. The absorption by an infinitesimal slice of thickness dx at a depth x is therefore equal to $I(x)\,\mu\,dx$. This must be equivalent to the differential attenuation in intensity of the x-ray beam, dI, such that

$$dI = -I(x)\,\mu\,dx$$

Dividing by $I(x)$ produces the differential equation

$$\frac{dI}{I(x)} = -\mu\, dx$$

Integrating the left side from I_0 to $I(x)$ and the right side from 0 to x yields

$$ln\left(\frac{I(x)}{I_0}\right) = -\mu x$$

Exponentiating both sides and multiplying through by I_0 produces

$$I(x) = I_0 e^{-\mu x}$$

This equation is commonly known as the *Bouguer-Lambert-Beer law* [27]. Using this relation, in principle, it is possible to empirically determine the absorption coefficient of a material by simply aiming an x-ray beam at a sample and using a detector to measure the fraction of photons that come out the other side, as long as the initial beam intensity and sample thickness are known. While this *transmission mode* method is perfectly valid, for many samples it is not an effective approach for measuring x-ray absorption. Because the x-rays interact so strongly with the electrons in the material, the penetration depth is far too low for any x-rays to make it through the sample to be measured by the detector. This is especially true for the soft x-ray regime that is often required for studying many classes of materials, such as in the case of transition-metal oxides, and is the primary focus of this dissertation. For this reason, x-ray absorption spectra are generally measured in *reflection mode* indirectly by instead detecting the decay products of the absorption process.

Before discussing the x-ray absorption process and its subsequent decay products, an important distinction must be made. X-ray absorption spectroscopy (XAS) is an inner shell spectroscopy, meaning that the incident x-rays are interacting with deep-core electrons, rather than valence electrons. If a deep-core electron absorbs a very hard x-ray with sufficient (typically

fixed) energy, it can be excited into the continuum of unbound states, ionizing the atom. However, this is the process that is measured by a technique called *x-ray photoelectron spectroscopy* (XPS), which is distinctly different from the absorption processes measured by XAS, in which core electrons are excited into unoccupied bound states and remain within the sample. The key difference is that bound states only exist at discrete energies, implying that the transitions between electronic states can only occur for certain discrete energies at values corresponding to the energy difference between the two transitional states. Because XAS uses a tunable x-ray beam to vary the beam energy, if there are no unoccupied states for the core electron to transition into that correspond to the energy of the incident photons, no absorption can occur.

As mentioned, in XAS a core electron absorbs an incoming photon and is promoted to an unoccupied bound state somewhere above the Fermi level, leaving behind a so-called *core hole*, as shown in Figure 3.2 [28]. This puts the system into an excited state that is unstable. The system relaxes to a lower energy state as an electron in a higher energy state decays into the core hole. The timescale of this relaxation is on the order of 1-2 femtoseconds. The decaying electron can emit a photon with an energy that is equal to the energy difference between its prior state the core hole state via fluorescence. In general, if the absorbed photon is within the x-ray range, the emitted photon will also be within the x-ray range. If the same electron that absorbed the incident photon collapses into the core hole state, the process is elastic and the emitted photon will have the same energy as the incident photon. Alternatively, the excess energy carried by the higher level electron decaying into the core hole can instead be transferred to a valence electron, causing that valence electron to be emitted into the continuum of unbound states. These emitted electrons are called *Auger* electrons. Thus, it is these decay products — the emitted photons or Auger electrons — that are measured to obtain the x-ray absorption spectra in reflection mode.

Technically, it is not usually the Auger electrons themselves that are directly detected. When an atom emits an Auger electron, it becomes ionized. To prevent the sample from becoming

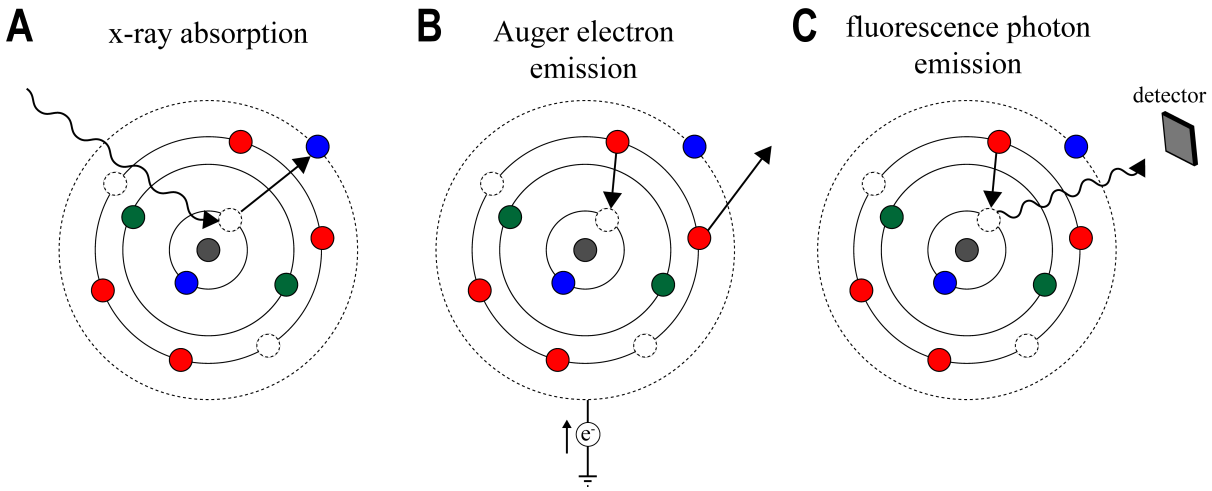

Figure 3.2: **A** An x-ray photon is absorbed by a core electron, exciting it into an unoccupied bound state above the Fermi level as it leaves behind an unstable core hole. **B** An electron decays into the core hole. The excess energy is transferred to another outer-shell electron, which is emitted as an Auger electron. This electron is replenished through the drain current, which is measured as part of the total electron yield. **C** Alternatively, as the electron decays into the core hole, the excess energy can be emitted as an fluorescence photon. The emitted photon is measured by a detector as part of the total fluorescence yield. Adapted from [28].

positively charged during XAS measurements, the sample is always grounded[1] such that the lost Auger electrons may be resupplied, thereby allowing the sample to remain neutral. Thus, it is this current that replenishes the sample that is typically measured during XAS experiments and is called the *total electron yield* (TEY). It is possible, though, to measure the Auger electrons directly; however, this is generally only done when it is necessary to measure Auger electrons within some energy range, such as in the cases of Auger electron spectroscopy (AES) or resonant photoemission spectroscopy (RPES). For XAS, however, it is not necessary to discriminate the Auger electron energies. There is a strong assumption that the TEY signal is proportional to the absorption because, as the sample absorbs more incident x-rays, more core holes are created, resulting in more Auger electrons being emitted, regardless of how much energy the Auger electrons carry. Therefore, measuring the TEY is a highly valid method of obtaining x-ray

[1] When performing XAS experiments, it is important to use a conductive adhesive (e.g., silver paint or epoxy) to mount the sample. If the sample itself (or its substrate, in the case of thin films) is not conductive, a small amount of silver paint is typically applied from the corner of the sample to its mounting plate in order to provide a grounding path.

absorption spectra.

The same logic is applied to measuring XAS by detecting photons emitted by the absorption process. In this case, it is the emitted photons themselves that are directly detected. It is possible, though, that the emitted photons can be reabsorbed by other atoms within the sample before reaching the detector. This effect is called *self-absorption* and can produce distortions in the fluorescence signal, implying that it is sometimes a less valid method of obtaining x-ray absorption spectra. Similar to measuring the TEY, these photons are detected without energy discrimination, which is called the *total fluorescence yield* (TFY). It is possible, though, to only count photons emitted with energies within some range, which is called the partial fluorescence yield. Furthermore, the entire spectrum of emitted photons can itself also be measured. We will see in Section 3.5 that this technique is called *resonant inelastic x-ray scattering*, which will be discussed later in more detail.

In practice, both the TEY and TFY signals are generally both recorded simultaneously when performing XAS measurements. Although these two signals are generally very similar, there are some key differences. TEY signals often exhibit significantly higher signal-to-noise ratios than TFY signals. This is in part because fluorescence is emitted isotropically and the photon detectors only span a small fraction of the overall 2π solid angle, so only a small fraction of the overall fluorescence is captured by the measurement. In contrast, because TEY measures the sample drain current, all electrons that are emitted from the sample contribute to the TEY signal. Furthermore, Auger electrons that are emitted below the surface layer interact strongly with other atoms within the sample as they are ejected towards the surface before escaping the sample. These interactions can create cascades of secondary electrons that are emitted from the valence band of the other atoms which act to amplify the TEY signal. Because emitted electrons interact so strongly with electrons in neighboring atoms via Coulomb repulsion, the probing depth of the TEY signal is shallower than for TFY. TEY signals are typically restricted to a probe depth of $\sim$10 nm, whereas TFY signals may exhibit a probe depth of 100-300 nm. This contrast allows

TEY and TFY signals to provide complimentary information about the sample surface and bulk, respectively.

Since photons carry momentum, the electronic excitations resulting from their absorption are subject to selection rules. Although quadrupole signals can be observed in hard x-ray excitations, the majority signals always follow the dipole selection rules:

$$\Delta l = \pm 1$$

$$\Delta m = 0, \pm 1$$

$$\Delta s = 0$$

$$\Delta j = 0, \pm 1 \text{ (no } 0 \rightarrow 0)$$

where l is the orbital angular momentum quantum number, m is the magnetic quantum number, s is the spin quantum number, and $j = l + s$ is the total angular momentum quantum number. The first equation states that electronic transitions resulting from the x-ray absorption must change by one shell (e.g., $s \rightarrow p$ and $p \rightarrow d$ or s). This restriction imposed by the dipole selection rule is significantly beneficial to XAS measurements because it offers the most direct way to probe these states. For example, oxygen $2p$ states may be directly probed through the excitation of $1s$ electrons (K-edge), while exciting the $2p$ electrons (L-edge) of a transition metal directly probes its $3d$ states.

The energy dependence of the electronic transition probability, T, will occur from an initial state, $|i\rangle$, to final state, $|f\rangle$, is given by Fermi's Golden Rule (Appendix A) [21]

$$T_{i \rightarrow f} = \frac{2\pi}{\hbar} |\langle f | \mathcal{H}_{int} | i \rangle|^2 \delta(E_i - E_f - \hbar\omega)$$

where E_i and E_f are the energies of the initial and final electronic states, $\hbar\omega$ is the x-ray energy, and $\mathcal{H}_{int}$ is the interaction Hamiltonian, which is given by

$$\mathcal{H}_{int} = \frac{e}{m_e} \boldsymbol{p} \cdot \boldsymbol{A}$$

where e is the elementary charge, m_e is the electron mass, $\boldsymbol{p}$ is momentum, and $\boldsymbol{A}$ is the vector potential, which is related to the electric field, $\boldsymbol{E}$, of the x-ray by

$$\boldsymbol{E} = -\frac{\partial \boldsymbol{A}}{\partial t}$$

where t is time. This implies that the electronic transitions are driven by the oscillating electric field of the incident x-rays. The absorption cross section can then be defined as

$$\sigma_a = \frac{T_{i \to f}}{\Phi_0}$$

where Φ_0 normalizes the transition probability by flux of the incident x-ray beam.

X-ray absorption spectra are thus measured by tuning the beam energy and the underlying functional form that is recorded is a direct consequence of the energy dependence of the absorption cross section. For free atoms, the absorption cross section features discontinuities, called *absorption edges*, at excitation energies corresponding to the transitions of core electrons, resulting in a sharp increase in the x-ray absorption as the beam energy is increased over these absorption edges. For atoms bound within solids, additional absorption features may be observed due to interactions with nearby atoms, as shown in Figure 3.3.

Near (within $\sim$50 eV of) the absorption edge, called the *x-ray absorption near edge structure* (XANES) region, features arising from strong scattering and local atomic resonances provide information about the bonding environment and oxidation state of the absorbing atom. As the oxidation state of the absorbing atom increases, the effective charge of the nucleus increases as a result of the reduced screening. This shifts the absorption edge to higher energy as more energetic x-rays are required to excite core electrons. Further (up to 1000 eV or more) above the absorption edge, called the *extended x-ray absorption fine structure* (EXAFS) region, quantum

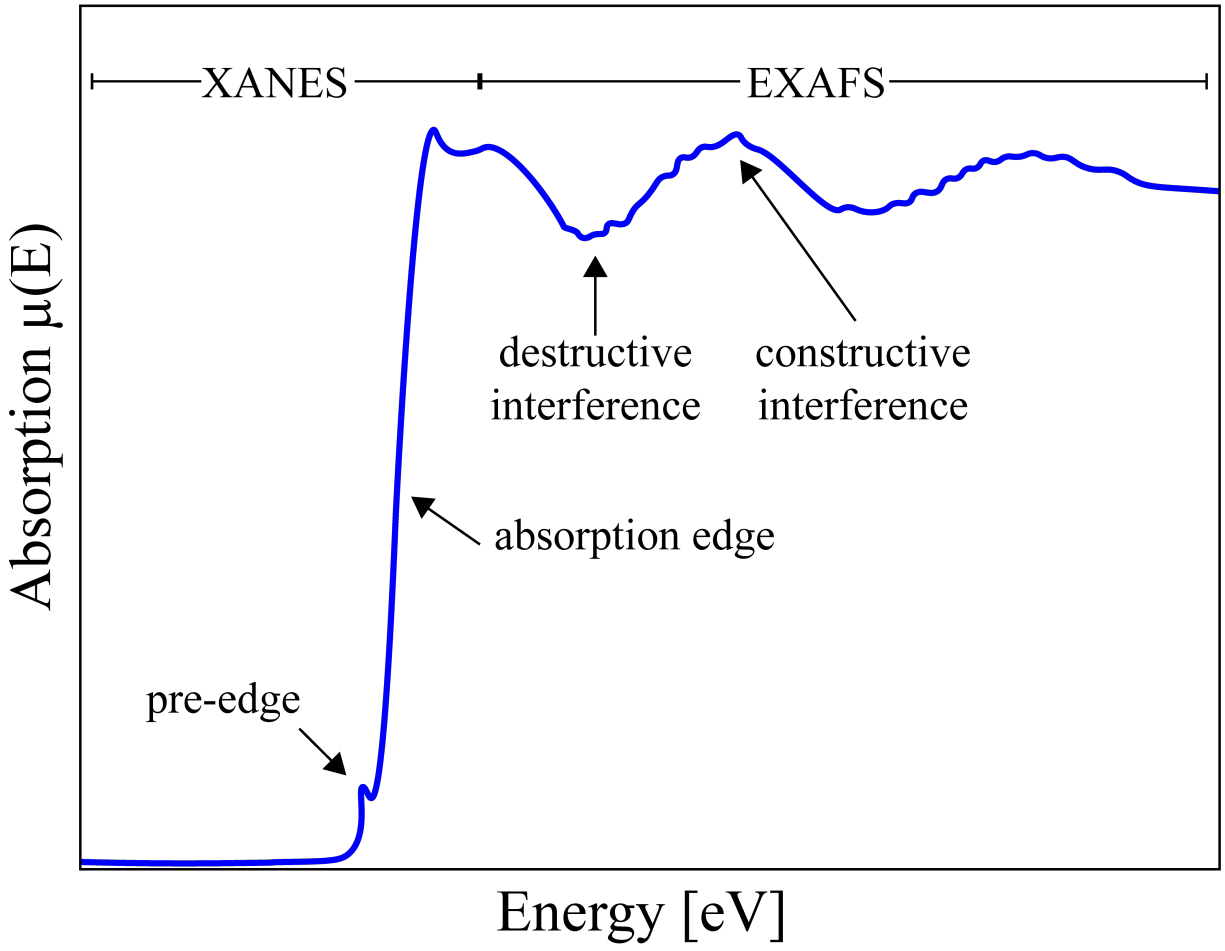

Figure 3.3: A typical x-ray absorption spectrum is shown. A weak pre-edge structure arises from transitions between bound states. The absorption sharply increases at the absorption edge when the x-ray beam energy matches that of an electric dipole transition. The x-ray absorption near edge structure (XANES) region provides information about the oxidation state of the absorbing atom. In the extended x-ray absorption fine structure (EXAFS) region, constructive and destructive interference arises from multiple scattering of emitted photoelectrons with nearby atoms. Adapted from [29].

interference effects resulting from the multiple scattering of emitted photoelectrons with other atoms create oscillations which provide further information about the local environment.

It is also possible for features to exist before the absorption edge, called the *pre-edge*. Pre-edge structures are typically weak because they result from transitions between bound states.

For example, pre-edge structures resulting from a $1s \rightarrow 3d$ transition are observed for all transition metals which do not have fully occupied $3d$ orbitals. This transition is dipole-forbidden, hence the weak transition probability, but it may still be observed due to direct quadrupolar coupling or $3d-4p$ orbital hybridization.

The nomenclature used to describe the different absorption edges is the modern IUPAC notation, as discussed in Chapter 2. It refers to the binding energy of the electronic state which absorbs the x-ray. In this notation, each principle quantum number (n) is represented by a capital letter, beginning with K for $n = 1$. The states within each electron shell are denoted with a numerical subscript, in order of increasing orbital angular momentum, l, and total angular momentum, j. The multiplicity of states, $2j+1$, gives the relative intensity of the observed absorption edges (e.g., the L_3 edge will be twice as strong as the L_2 because its multiplicity is double). This notation is summarized up through $n = 4$ in Table 3.1.

Table 3.1: IUPAC notation is used to label x-ray absorption edges. The electronic shells are labeled as $(nl_j)^{2j+1}$, where n, l, s, and j are the principal, orbital angular momentum, spin, and total angular momentum quantum numbers, where j runs from $|l-s| \leq j \leq l+s$, and the multiplicity is $2j+1$.

n	l	s	j	$2j+1$	Electronic state	IUPAC notation
1	0	$\frac{1}{2}$	$\frac{1}{2}$	2	$\left(1s_{\frac{1}{2}}\right)^2$	K
2	0	$\frac{1}{2}$	$\frac{1}{2}$	2	$\left(2s_{\frac{1}{2}}\right)^2$	L_1
2	1	$\frac{1}{2}$	$\frac{1}{2}$	2	$\left(2p_{\frac{1}{2}}\right)^2$	L_2
2	1	$\frac{1}{2}$	$\frac{3}{2}$	4	$\left(2p_{\frac{3}{2}}\right)^4$	L_3
3	0	$\frac{1}{2}$	$\frac{1}{2}$	2	$\left(3s_{\frac{1}{2}}\right)^2$	M_1
3	1	$\frac{1}{2}$	$\frac{1}{2}$	2	$\left(3p_{\frac{1}{2}}\right)^2$	M_2
3	1	$\frac{1}{2}$	$\frac{3}{2}$	4	$\left(3p_{\frac{3}{2}}\right)^4$	M_3
3	2	$\frac{1}{2}$	$\frac{3}{2}$	4	$\left(3d_{\frac{3}{2}}\right)^4$	M_4
3	2	$\frac{1}{2}$	$\frac{5}{2}$	6	$\left(3d_{\frac{5}{2}}\right)^6$	M_5
4	0	$\frac{1}{2}$	$\frac{1}{2}$	2	$\left(4s_{\frac{1}{2}}\right)^2$	N_1
4	1	$\frac{1}{2}$	$\frac{1}{2}$	2	$\left(4p_{\frac{1}{2}}\right)^2$	N_2
4	1	$\frac{1}{2}$	$\frac{3}{2}$	4	$\left(4p_{\frac{3}{2}}\right)^4$	N_3
4	2	$\frac{1}{2}$	$\frac{3}{2}$	4	$\left(4d_{\frac{3}{2}}\right)^4$	N_4
4	2	$\frac{1}{2}$	$\frac{5}{2}$	6	$\left(4d_{\frac{5}{2}}\right)^6$	N_5
4	3	$\frac{1}{2}$	$\frac{5}{2}$	6	$\left(4f_{\frac{5}{2}}\right)^6$	N_6
4	3	$\frac{1}{2}$	$\frac{7}{2}$	8	$\left(4f_{\frac{7}{2}}\right)^8$	N_7

3.2 Elastic X-ray Scattering

The simplest case of x-ray scattering occurs when the energy of the incident and outgoing photon is conserved, known as elastic scattering. In reality, x-ray scattering is generally not purely elastic and is more accurately described as *Bragg scattering*, which is defined as the scattering by the thermodynamic average of the electronic charge density, with Bragg scattering only approaching purely elastic scattering at low temperature. But at ordinary temperatures for for large structures, such as crystalline solids, the Bragg and elastic scattering only deviate by $O(N^{-1})$, where N is the number of vibration degrees of freedom and, in most practical cases, purely elastic and Bragg x-ray scattering can be considered to be essentially equivalent [30].

While x-ray scattering techniques are indeed used to study non-crystalline systems, such as liquids, glasses, or polymers, this dissertation will focus on scattering from crystals, in which the constituent atoms are arranged into structures which possess long-range spatial ordering. Crystals consist of a periodic arrays of points in one, two, or three dimensions, forming a *lattice*. Attached to each lattice point is one or more atoms, called a *basis*, that is the same for every lattice site. A lattice therefore necessarily possesses translational symmetry when shifting from one lattice point to another. Navigation between lattice points is facilitated by assigning a set of *lattice vectors*, requiring one lattice vector per dimension, as shown in Figure 3.4 for a two-dimensional lattice. These lattice vectors define the *crystallographic axes*. The choice of lattice vectors is not unique and may be chosen arbitrarily as long as each vector *i*) begins and terminates on a lattice site and *ii*) is linearly independent of the other vectors in the set. Using this set of lattice vectors, a *lattice translation operator* may be constructed, which has the following form in three dimensions

$$\boldsymbol{T} = n_1\boldsymbol{a}_1 + n_2\boldsymbol{a}_2 + n_3\boldsymbol{a}_3$$

where $\{\boldsymbol{a}_1, \boldsymbol{a}_2, \boldsymbol{a}_3\}$ are the set of lattice vectors and $\{n_1, n_2, n_3\}$ are arbitrary integers. The crystal

remains invariant under any translations by this operator. The lengths of the unit cell along each crystallographic axis, which are determined by the magnitudes of the lattice vectors, $\{a_1,\ a_2,\ a_3\}$ or commonly $\{a,\ b,\ c\}$, are referred to as *lattice constants*. These lattice vectors form the edges of the *unit cell*, whose volume is given by the following formula in three dimensions

$$V = |\boldsymbol{a}_1 \times \boldsymbol{a}_2 \cdot \boldsymbol{a}_3|$$

A *primitive* unit cell is defined as the unit cell in which the volume is minimized, such as in the case of the *Wigner-Seitz* cell, which is constructed by bisecting the lines connecting a lattice point with its nearest neighbors. In practice, however, it is usually most convenient to work with a *conventional* unit cell, which is formed by assigning the set of lattice vectors which best reflects the symmetries of the underlying lattice.

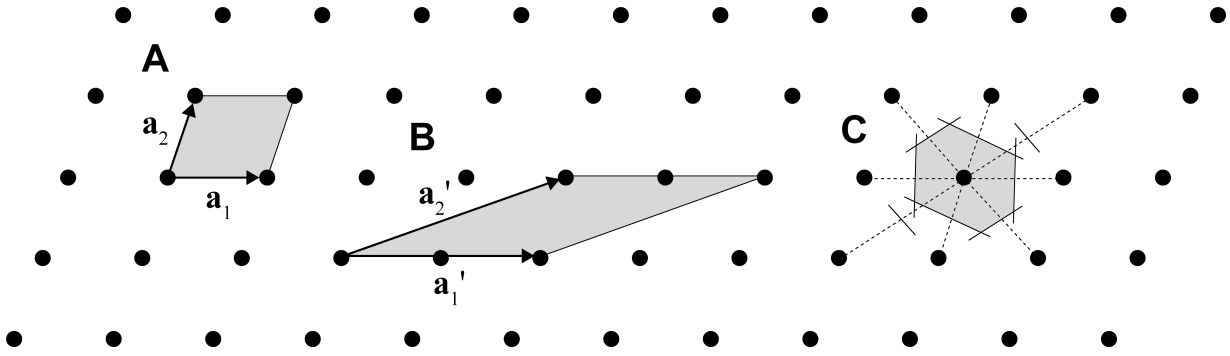

Figure 3.4: **A** A primitive cell is formed by choice of lattice vectors $\{\boldsymbol{a}_1,\ \boldsymbol{a}_2\}$. **B** The choice of lattice vectors $\{\boldsymbol{a}_1',\ \boldsymbol{a}_2'\}$ results in a unit cell that is both non-primitive and non-conventional. **C** The Wigner-Seitz unit cell is constructed by bisecting the lines connecting a lattice point with its nearest neighbors (dashed lines). Adapted from [31].

As it turns out, in three dimensions, there are identically 14 unique lattices, called *Bravais* lattices, belonging to 7 systems, which are defined by the equivalence of the dimensions $\{a_1,\ a_2,\ a_3\}$ and interior angles $\{\alpha,\ \beta,\ \gamma\}$ of the unit cell [31]. Each system contains a combination of simple (P), body centered (I), base centered (C), and face centered (F) lattices, yielding the 14 Bravais lattices, as shown in Figure 3.5. In two dimensions, this number is reduced to 5 unique

lattices. Similarly, there are 32 unique *point groups* which describe the compatible symmetry operations of the atomic bases that attach to each lattice point of the 7 lattice systems. Each point group may posses some combination of rotational, enantiomorphic (i.e., possessing only rotation axes), centrosymmetric (i.e., possessing a center of inversion), and polar (i.e., possessing symmetry about the polar axis) symmetries [32]. The properties of the lattice systems and their point groups are tabulated in Table 3.2.

Table 3.2: The 7 three-dimensional lattice systems are defined by the equivalence of the dimensions $\{a_1, a_2, a_3\}$ and interior angles $\{\alpha, \beta, \gamma\}$ of the unit cell. Each system contains a combination of simple (*P*), body-centered (*I*), base-centered (*C*), and face-centered (*F*) lattices, yielding 14 Bravais lattices in total. The 7 lattice systems support a total of 32 point groups that each possess some combination of rotational, enantiomorphic (red), centrosymmetric (blue), and polar (**bold**) symmetries. Adapted from [31, 32].

System	Lattices	Parameters	Point groups
Triclinic	*P*	$a_1 \neq a_2 \neq a_3$ $\alpha \neq \beta \neq \gamma$	**1**, -1
Monoclinic	*P*, *C*	$a_1 \neq a_2 \neq a_3$ $\alpha = \gamma = 90^\circ \neq \beta$	**2**, ***m***, 2/*m*
Orthorhombic	*P*, *I*, *C*, *F*	$a_1 \neq a_2 \neq a_3$ $\alpha = \beta = \gamma = 90^\circ$	222, ***mm*2**, *mmm*
Tetragonal	*P*, *I*	$a_1 = a_2 \neq a_3$ $\alpha = \beta = \gamma = 90^\circ$	**4**, -4, 4/*m*, 422, ***4mm***, -42*m*, 4/*mmm*
Cubic	*P*, *I*, *F*	$a_1 = a_2 = a_3$ $\alpha = \beta = \gamma = 90^\circ$	23, *m*-3, 432, -43*m*, *m*-3*m*
Trigonal	*P*	$a_1 = a_2 = a_3$ $\alpha = \beta = \gamma < 120^\circ, \neq 90^\circ$	**3**, -3, 32, ***3m***, -3*m*
Hexagonal	*P*	$a_1 = a_2 \neq a_3$ $\alpha = \beta = 90^\circ$ $\gamma = 120^\circ$	**6**, -6, 6/*m*, 622, ***6mm*** -62*m*, 6/*mmm*

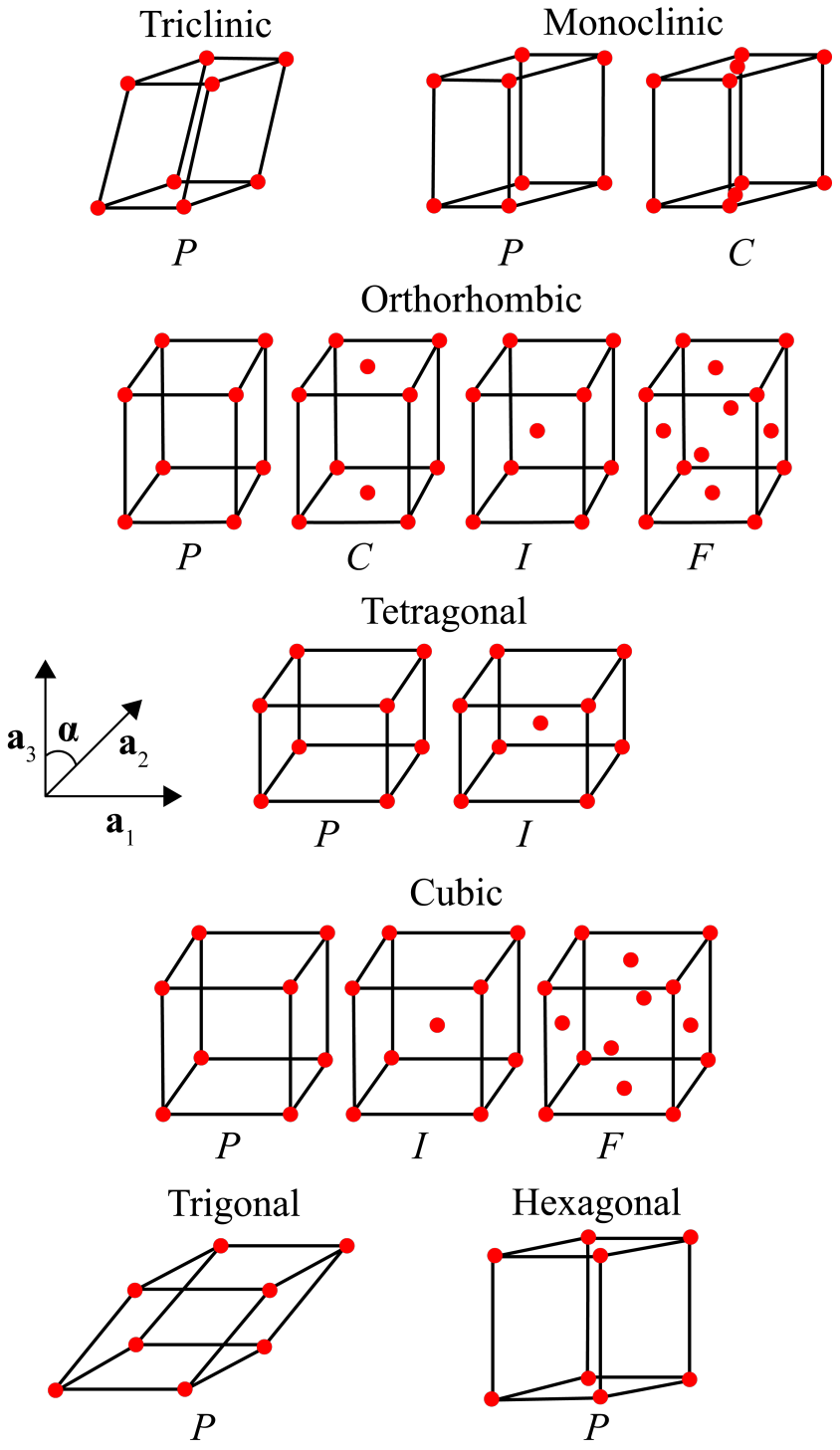

Figure 3.5: The 7 lattice systems are shown. Each lattice system contains some combination of simple (*P*), body-centered (*I*), base-centered (*C*), and face-centered (*F*) lattices, yielding the 14 Bravais lattices. Adapted from [33].

For the purposes of x-ray scattering, it is useful to think of the atoms within the crystal as lying within different families of planes. Three non-colinear points are required to specify a unique crystal plane. As it turns out, the most convenient way of specifying a crystal plane is using *Miller indices*, for reasons which will be discussed shortly. To identify the Miller indices for a crystal plane:

1. Identify the intercepts of the plane along each crystallographic axis in units of the lattice constants, a_1, a_2, and a_3 (or commonly a, b, and c).

2. Take the reciprocal of each intercept.

3. If this set of reciprocals contains any fractions, multiply the entire set by the lowest common denominator.

4. The resulting Miller indices are expressed as (hkl). Negative indices are expressed with a bar above that index.

For example, if a crystal plane has intercepts which are located 4 unit cells along the a_1 axis, $\frac{1}{2}$ of a unit cell along the a_2 axis, and -2 unit cells along the a_3 direction, the reciprocals of $\{4, -\frac{1}{2}, 2\}$ are $\{\frac{1}{4}, -2, \frac{1}{2}\}$, which has a lowest common denominator of 4. Multiplying each reciprocal by 6 produces $\{1, -8, 2\}$, which is expressed as $(1\bar{8}2)$. While (hkl) denotes a particular crystal plane, the notation $\{hkl\}$ is used to denote the set of planes which are symmetrically equivalent. Additionally, $[hkl]$ is used to denote the direction that is normal to the (hkl) plane and $\langle hkl \rangle$ is used to denote the set of directions which are symmetrically equivalent to $[hkl]$.

It is important to make the distinction that, while (hkl) denotes a particular crystal plane, it is not a singular plane but rather the entire set of identical planes existing through all unit cells of the crystal. These planes are evenly spaced, with a lattice spacing d_{hkl}. For orthorhombic systems

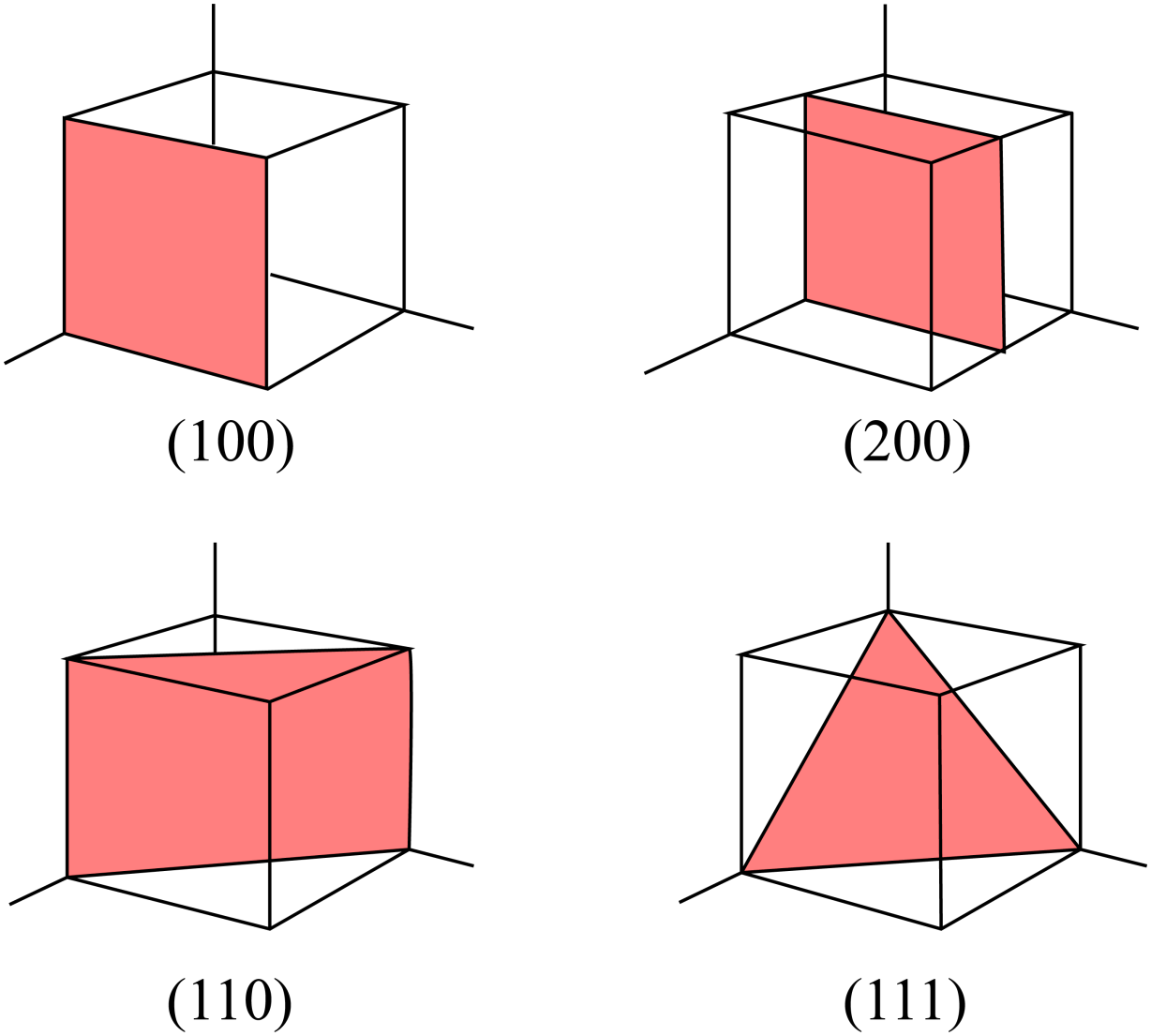

Figure 3.6: Some common lattice planes (red) are illustrated with their corresponding Miller indices for a cubic system. The (200) plane is parallel to the (100) plane, but with half of the lattice spacing. Adapted from [31].

$$\frac{1}{d_{hkl}^2} = \frac{h^2}{a^2} + \frac{k^2}{b^2} + \frac{l^2}{c^2}$$

This formula is straightforward to apply to tetragonal and cubic systems where two or three of the lattice constants are equivalent, respectively. For the cubic system, this simplifies to

$$d_{hkl} = \frac{a}{\sqrt{h^2 + k^2 + l^2}}$$

The formulas for triclinic, monoclinic, and trigonal systems are significantly more complex because they must involve the values of the angles, $\{\alpha,\ \beta,\ \text{and}\ \gamma\}$, and will not be listed explicitly. However, it may be useful to provide the formula for hexagonal systems, which are relatively common

$$\frac{1}{d_{hkl}^2} = \frac{4}{3}\left(\frac{h^2 + hk + k^2}{a^2}\right) + \frac{l^2}{c^2}$$

Now that the concepts of crystal lattices and planes have been established, the elastic scattering of x-rays by crystals may be introduced. X-rays are electromagnetic waves and are therefore subject to wave phenomena. The interatomic distances within a solid are typically on the order of 1 Å $= 10^{-10}$ m. Therefore, light must have a wavelength that is of similar order or smaller in order to observe interference effects arising from the scattering of atoms within a solid. This corresponds to an energy of the order [34]

$$\hbar\omega = \frac{hc}{\lambda} = \frac{hc}{10^{-10}\ \text{m}} = 12.3 \times 10^3\ \text{eV}$$

This energy falls firmly within the x-ray regime, as shown in Figure 2.1. *X-ray diffraction* exploits these interference effects to obtain information about the atoms within the materials being studied. Consider a beam of monochromatic x-rays with some wavelength, λ, that is incident upon some sample, as shown in Figure 3.7. The sample is a crystalline material, so the atoms are periodically ordered according to the symmetry of the underlying lattice. The angle of incidence between the x-rays and some particular family of crystal planes is θ. This is assumed to be an elastic scattering process, so x-rays are reflected by the lattice planes at the same angle, θ, and the wavelength of the scattered x-rays is conserved. Because the spacing between lattice planes is d, x-rays scattered from two adjacent planes will be subject to a difference in path length.

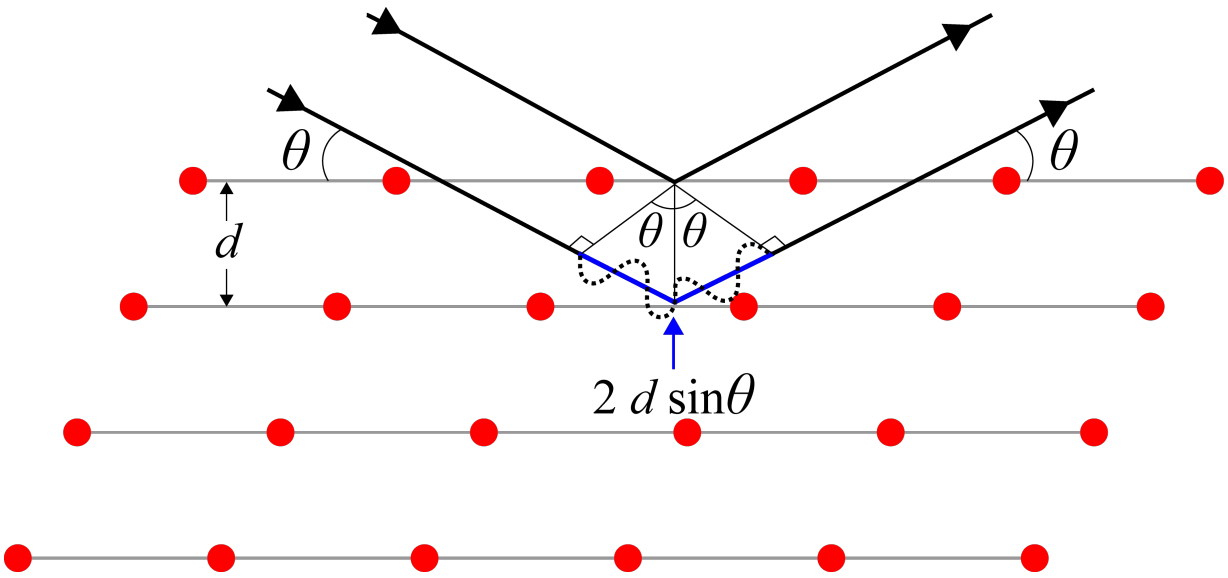

Figure 3.7: A particular family of crystal planes (gray lines) contains identical arrangements of lattice site (red circles) that are separated by a distance, d. X-rays (black lines) are incident upon two neighboring planes at an angle, θ, and are reflected at the same angle. The path difference (blue lines) of the incident and reflected x-rays sum to $2d\sin(\theta)$. The Bragg condition is satisfied when this path difference is equal to an integer multiple of the x-ray wavelength, as shown (dotted line) for $n = 3$.

This difference in path length for the incident x-rays scattered by two neighboring planes is $d\sin\theta$. Likewise, the difference in path length after elastically scattering is also $d\sin\theta$. The total difference in path length between the scattered x-rays is therefore $2d\sin\theta$. In the majority of cases, no scattered x-rays will be observed due to destructive interference between neighboring planes. However, if the difference in path length between scattered x-rays happens to be an integer multiple of the x-ray wavelength, constructive interference may occur. This condition for constructive interference is known as the *Bragg condition* or as *Bragg's law*

$$n\lambda = 2d\sin\theta$$

where n is an integer corresponding to the *order* of the Bragg reflection. By rotating a crystal through an x-ray beam at many angles, a diffraction pattern is produced as the Bragg condition is occasionally satisfied for the different families of lattice planes. The produced diffraction pattern

is related to the crystal planes through a *Fourier transform*. Just as the Fourier transform of a signal that is periodic in the *time domain* yields a single, discrete frequency in the *frequency domain*, the Fourier transform of a structure that is periodic in *space* yields a single, discrete point in what is called *reciprocal space*. Unlike time, space is three-dimensional and taking the Fourier transform of a structure with periodicities in three dimensions yields points that are also distributed in three dimensions. A Fourier transform may therefore be applied to a crystal lattice and doing so forms a set of points in reciprocal space that is called a *reciprocal lattice*, as shown in Appendix B.

The lattice in real space is often referred to as the *direct* lattice in order to distinguish it from the reciprocal lattice. As it turns out, applying a Fourier transform to a Bravais lattice in direct space yields a Bravais lattice in reciprocal space. As Fourier transforms preserve the angles between vectors, the angles $\{\alpha, \beta, \gamma\}$ are equivalent for unit cells on both the direct and reciprocal lattices. This implies that the reciprocal lattice will belong to the same system as the direct lattice. It does not, however, guarantee that the reciprocal lattice will be the same Bravais lattice as the direct lattice. For example, if the direct lattice is face-centered cubic (fcc), the reciprocal lattice will be body-centered cubic (bcc) and vice versa. It also does not guarantee that the reciprocal lattice vectors will be parallel to the direct lattice vectors. For example, if the direct lattice is hexagonal, the in-plane reciprocal lattice vectors will be rotated by 30°with respect to the direct lattice vectors. The reciprocal lattice vectors $\{\boldsymbol{b}_1, \boldsymbol{b}_2, \boldsymbol{b}_3\}$ are related to the direct lattice vectors $\{\boldsymbol{a}_1, \boldsymbol{a}_2, \boldsymbol{a}_3\}$ through the relations

$$\boldsymbol{b}_1 = \frac{2\pi}{V_{uc}} \boldsymbol{a}_2 \times \boldsymbol{a}_3$$
$$\boldsymbol{b}_2 = \frac{2\pi}{V_{uc}} \boldsymbol{a}_1 \times \boldsymbol{a}_3$$
$$\boldsymbol{b}_3 = \frac{2\pi}{V_{uc}} \boldsymbol{a}_1 \times \boldsymbol{a}_2$$

where $V_{uc} = \boldsymbol{a}_1 \cdot (\boldsymbol{a}_2 \times \boldsymbol{a}_3)$ is the volume of the unit cell in real space. By taking the magnitudes of the above relations, we can see that the spacing between reciprocal lattice points, $\{b_1, b_2, b_3\}$ (or commonly $\{h,k,l\}$), along the directions of the reciprocal lattice vectors, $\{\boldsymbol{b}_1, \boldsymbol{b}_2, \boldsymbol{b}_3\}$, is related to the direct lattice spacing between lattice points, $\{a_1, a_2, a_3\}$, along the directions of the direct lattice vectors, $\{\boldsymbol{a}_1, \boldsymbol{a}_2, \boldsymbol{a}_3\}$, through the relations

$$b_1 = \frac{2\pi}{a_1}$$
$$b_2 = \frac{2\pi}{a_2}$$
$$b_3 = \frac{2\pi}{a_3}$$

Each family of lattice planes in the direct lattice possesses a unique combination of periodicity and direction and therefore corresponds to identically one point on the reciprocal lattice. Herein lies the reason behind why indexing lattice planes by their reciprocals is so useful. The Miller indices of a crystal plane are also the reciprocal space coordinates of its corresponding diffraction peak; i.e., it tells the experimenter exactly where to stick the detector, as long as the periodicity and its corresponding direction are known. The diffraction peaks are observed when the tip of the *scattering vector* (or momentum transfer vector, as shown in Section 2.2), $\mathbf{Q}$, lies on a reciprocal lattice site. As shown in Figure 3.8, the scattering vector is defined as

$$\mathbf{Q} = \boldsymbol{k}_{out} - \boldsymbol{k}_{in}$$

where $\boldsymbol{k}_{in}$ is the wavevector of the incident x-ray and $\boldsymbol{k}_{out}$ is the wavevector of the outgoing x-ray. The scattering process is elastic, so $|\boldsymbol{k}_{in}| = |\boldsymbol{k}_{out}| = \frac{2\pi}{\lambda}$. Additionally, $\theta_{in} = \theta_{out} = \theta$, where θ_{in} and θ_{out} are the angles of the incident and outgoing wavevectors, respectively, measured with respect to the plane of the sample. The magnitude of $\mathbf{Q}$ is then

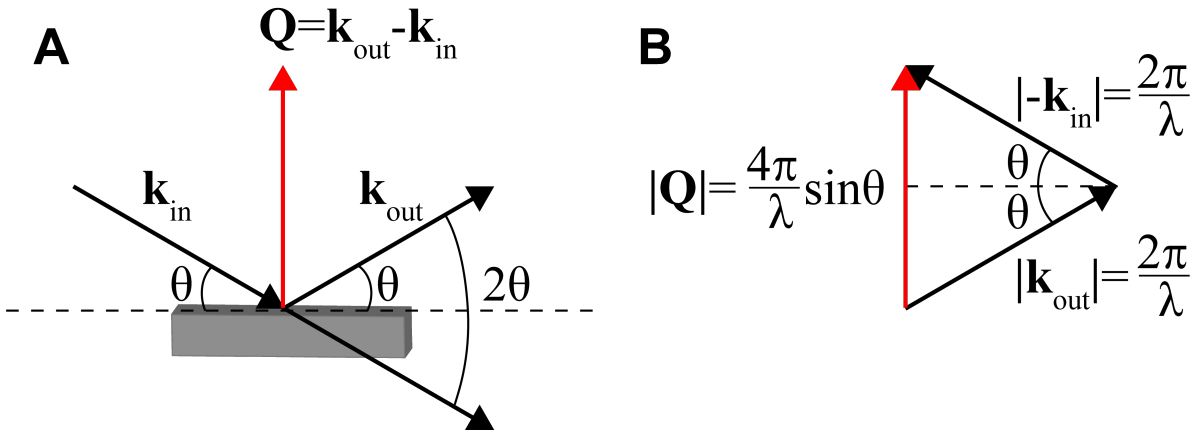

Figure 3.8: **A** An x-ray with wavevector $\boldsymbol{k}_{in}$ is incident upon a sample at an angle θ, relative to the plane of the sample. The outgoing x-ray with wavevector $\boldsymbol{k}_{out}$ is scattered at an angle θ, relative to the plane of the sample, or 2θ, relative to $\boldsymbol{k}_{in}$. Diffraction is observed when the tip of the scattering vector, $\mathbf{Q} = \boldsymbol{k}_{out} - \boldsymbol{k}_{in}$, lies on a reciprocal lattice point. **B** The magnitude of **Q** may be calculated from the right triangles formed by its vector sum.

$$|\mathbf{Q}| = \frac{4\pi}{\lambda}\sin\theta = \frac{2\pi}{d_{hkl}}$$

where the rightmost expression has been obtained by substituting the Bragg condition, $n\lambda = 2d\sin\theta$, for $n = 1$, which we now recognize as the Fourier transform of the family of lattice planes from which the x-rays are scattering. In real x-ray scattering experiments, it is usually not feasible to change the angle of the x-ray beam itself. The x-ray beam typically remains fixed and the incident scattering angle, θ, is instead varied by rotating the sample. Relative to the incident beam, rather than the plane of the sample, the x-rays are scattered through an angle 2θ. Since it is the scattered x-rays that are measured in experiment, the angle of the detector is parameterized by 2θ. When the condition $2 \times \theta = 2\theta$ is satisfied, the scattering is *specular*, meaning that the scattering vector is parallel to the sample normal. In general, however, θ and 2θ may be moved independently as long as $\frac{2\theta}{2} > \theta$, in which prevents the scattered x-rays from being blocked by the sample itself. Using the relation $E = \frac{hc}{\lambda}$ for the energy of the x-ray photon, we can rewrite $|\mathbf{Q}|$ as

$$|\mathbf{Q}| = \frac{4\pi}{hc}E\sin\theta$$

which indicates that the magnitude of the scattering vector scales not only with angle, but also with the photon energy. This implies that higher energy x-rays are able to access more points on a reciprocal lattice than lower energy x-rays. The region of reciprocal space which may be accessed by a given x-ray wavevector (ignoring the sample shadow) is called an *Ewald sphere*. The Ewald sphere is constructed by aligning $\boldsymbol{k}_{in}$ such that its tip falls at the origin of the reciprocal lattice. As 2θ is varied from 0 to 2π while maintaining the specular condition, Q traces the boundary of Ewald sphere boundary, as shown in Figure 3.9. All reciprocal lattice sites which fall within the Ewald sphere may be experimentally accessed, barring those blocked by the sample. However, this is a limitation of the mounting geometry and access to these lattice sites may be recovered by simply mounting the sample in a different orientation. Accessing lattice sites which fall outside of the Ewald sphere boundary is significantly less trivial, as this requires increasing the x-ray energy to expand the Ewald sphere radius.

As its name implies, the Ewald sphere is three-dimensional, while the set of points spanned by $\{\theta, 2\theta\}$ is restricted to a two-dimensional plane, called the *scattering plane*. Hence, we require an additional angle to access the set of reciprocal lattice points that are contained by the Ewald sphere but lie outside of the scattering plane. One option is rotate the sample in-plane about its surface normal, which is parameterized by the angle ϕ. The other option is by varying the angle χ, which is essentially akin to a polar angle in spherical coordinates, like θ, but rotated 90° so that its axis of rotation is perpendicular to θ. Thus, the set of angles $\{\theta, 2\theta, \chi, \phi\}$ form the so-called four-circle scattering geometry, as shown in Figure 3.10. There is, however, an inherent issue to describing a three-dimensional space with four angular variables. The transformation from $(h,k,l) \rightarrow (\theta, 2\theta, \chi, \phi)$ results in an associated degeneracy of 2π. This issue may be resolved in a few ways. The most common method is to set $\phi = 0^\circ$ and use χ to access reciprocal lattice points that lie outside of the θ-2θ plane. An alternative method is to set $\chi = 90^\circ$ and use ϕ instead of χ. It is also possible to define an angle, ω, such that $\omega = \theta - \frac{2\theta}{2}$ and set $\omega = 0$, thereby removing the linear independence of θ and 2θ [36].

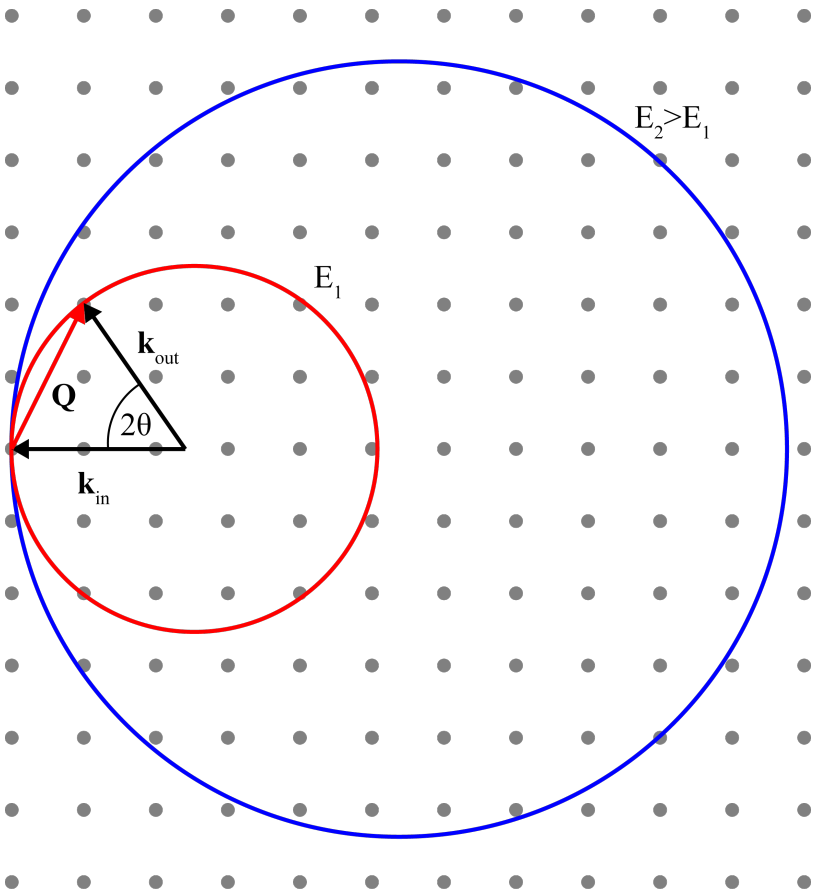

Figure 3.9: The projection of two Ewald spheres on the scattering plane are shown for x-rays with energies E_1 (red) and $E_2 > E_1$ (blue). For x-rays with energy E_1, as 2θ is varied from 0 to 2π while maintaining the specular condition, the scattering vector, $\mathbf{Q}$, sweeps out the boundary of the Ewald sphere. All reciprocal lattice points (gray dots) contained within the projection of this Ewald sphere may be accessed by some combination of $\{\theta, 2\theta\}$. Increasing the x-ray energy from E_1 to E_2 expands the radius of the Ewald sphere, allowing access to a larger region of reciprocal space. Adapted from [35].

Bragg's law is useful for determining the location of diffraction peaks in reciprocal space, but it does not provide any information about their intensity. Historically, x-ray diffraction by crystals was experimentally observed prior to understanding their origin. Once the Bragg condition was established, it successfully explained all of these observed diffraction peaks. However, upon attempting to use Bragg's law to predict the existence of previously unobserved peaks, it was discovered that some of these peaks appeared to be absent. Furthermore, it failed to predict why some diffraction peaks were brighter than others. This is because the Bragg's

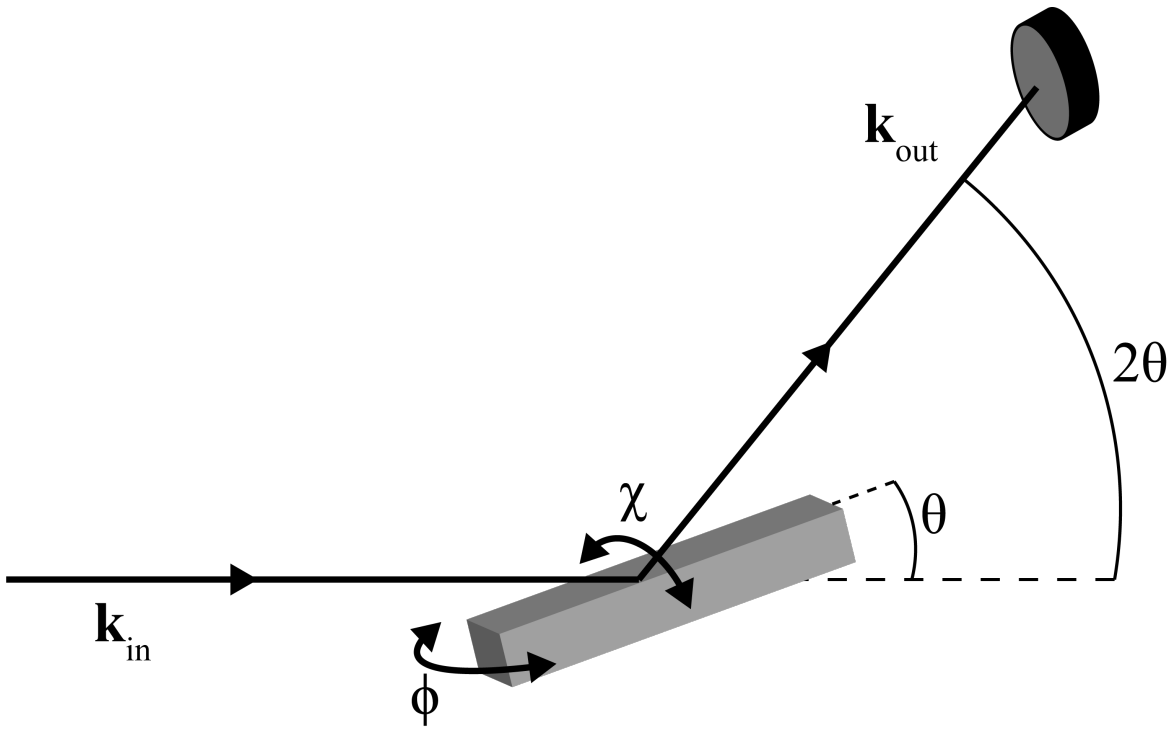

Figure 3.10: An incident x-ray with wavevector $\boldsymbol{k}_{in}$ scatters from a sample with wavevector $\boldsymbol{k}_{out}$ before being measured by a detector. The angle of the sample relative to $\boldsymbol{k}_{in}$ is given by θ. The angle of the detector relative to $\boldsymbol{k}_{in}$ is given by 2θ. The angle of the sample along the in-plane axis perpendicular to $\boldsymbol{k}_{in}$ is given by χ. The in-plane rotation angle of the sample is given by ϕ.

law formulation neglects the structure of the charge density and instead approximates it as being uniformly distributed across the lattice planes. In order to accurately predict the intensity of x-ray diffraction peaks, one must account for both the scattering amplitude by individual atoms, as well as interference effects arising from multiple atoms within the unit cell.

The scattering amplitude from a single atom is given by the *atomic form factor*, $f^0(\mathbf{Q})$, which is defined as the Fourier transform of the charge density [11]

$$f^0(\mathbf{Q}) = \int \rho(\boldsymbol{r}) e^{i\mathbf{Q}\cdot\boldsymbol{r}} d\boldsymbol{r}$$

where $\rho(\boldsymbol{r})$ is the spatial distribution of the charge density. In the limit that $\mathbf{Q} \to 0$

$$f^0(\mathbf{Q}=0)=Z$$

where Z is the atomic number. Because the scattered intensity is proportional to the form factor squared, this explains why the coherent scattering cross section is proportional to Z^2, as discussed in Section 2.2. This is, however, a purely classical formulation that does not account for the electronic structure of discrete bound states that arises quantum mechanics. The full form of the atomic form factor is then

$$f(\mathbf{Q},\omega)=f^0(\mathbf{Q})+f'(\omega)+if"(\omega) \tag{3.1}$$

where the last two terms are called *dispersion corrections* and depend explicitly on the x-ray energy. If the energy of the incident x-ray is much less than the electronic binding energies, the dispersion corrections reduce the scattering cross section. If the x-ray energy matches that of an electronic transition, the scattering is said to be *resonant* and the cross section becomes significantly enhanced. For x-ray energies that are much greater than the electronic binding energies, the dispersion corrections become negligible.

Now that the scattering amplitude from individual atoms has been discussed, the scattering amplitude from the ensemble of atoms within a crystal, called the *structure factor*, may be analyzed. A crystalline material may be described as the convolution of the lattice with its atomic basis. Similar to the atomic form factor, the structure factor is defined as the Fourier transform of the crystal structure. The convolution theorem therefore implies that the structure factor, $F(\mathbf{Q})$, is the product of structure factors for the lattice and basis

$$F(\mathbf{Q})=\sum_n e^{i\mathbf{Q}\cdot\boldsymbol{R}_n}\sum_j f_j(\mathbf{Q})e^{i\mathbf{Q}\cdot\boldsymbol{r}_j}$$

where $\boldsymbol{R}_n$ is a lattice vector and $\boldsymbol{r}_j$ is a vector that labels the positions of atoms within a unit cell. The second summation is called the *unit cell structure factor* and sums over the atomic form factor of each atom in the basis, while the first summation sums over all lattice sites in the crystal. Evaluation of the unit cell structure factor results in *diffraction selection rules* which specify which reflections will have a non-zero diffraction intensity for a given lattice structure. A simple example is for the body-centered cubic lattice, which has a basis with atoms located at $(0,0,0)$ and $(\frac{1}{2},\frac{1}{2},\frac{1}{2})$. For simplicity, lets assume both atoms in the basis are identical, so that they have an equivalent atomic form factor, f. Then, the unit cell structure factor evaluates to:

$$\begin{aligned}
\sum_j f_j(\mathbf{Q}) e^{i\mathbf{Q}\cdot\boldsymbol{r}_j} &= f\sum_j e^{2\pi i(hx_j+ky_j+lz_j)} \\
&= f[1+e^{i\pi(h+k+l)}] \\
&= f[1+(-1)^{h+k+l}] \\
&= \begin{cases} 2f, & h+k+l = \text{even} \\ 0, & h+k+l = \text{odd} \end{cases}
\end{aligned}$$

As shown, reflections where (h,k,l) sum to an odd number, such as the (001) or (111) reflections, will have zero intensity, thereby explaining why some diffraction peaks predicted by Bragg's law could not be experimentally observed. The diffraction selection rules for some common unit cell types can be found in Table 3.3.

Table 3.3: The diffraction selection rules determine if a reflection with Miller indices (hkl) is allowed or forbidden for various common unit cell types. Adapted from [37].

Unit Cell Type	Allowed Reflections	Forbidden Reflections
Primitive	any h,k,l	none
Body-centered	$h+k+l$ =even	$h+k+l$ =odd
Face-centered	h,k,l all odd or h,k,l all even	h,k,l mix of odd and even
Diamond (fcc)	h,k,l all odd or h,k,l = multiple of 4	h,k,l mix of odd and even or h,k,l all even but not a multiple of 4
Hexagonal	l odd and $h+2k$ is not a multiple of 3 or l even	l odd and $h+2k$ is a multiple of 3

3.3 Resonant Elastic X-ray Scattering

X-rays in traditional scattering experiments interact with all atomic electrons and, because the majority of these electrons are located in the core near the nucleus, such techniques are very suitable for determining things such as the lattice structure of a crystal or the orientation distribution of crystallites in a thin film. However, much of modern condensed matter research concerns the study of strongly correlated systems in which the electronic charge, orbital, and/or spin degrees of freedom collectively order, giving rise to novel ground states that lead to exotic phenomena such as high-temperature superconductivity in cuprates [38, 39] and colossal magnetoresistance in manganites [40, 41]. It is therefore difficult to observe these phenomena with conventional x-ray scattering since only a small fraction of the valence electrons are typically involved in the ordering.

A far more efficient technique for studying these charge, orbital, and spin modulations is

resonant elastic x-ray scattering[2] (REXS), which is essentially the same x-ray diffraction used to probe spatial modulations as described in Section 3.2, but augmented by an additional XAS component that enables sensitivity to electronic structure. This is achieved by tuning the incident beam energy to an absorption edge. The incident x-ray excites a core electron to an unoccupied state, producing a core hole. The excited electron decays back into the core hole and emits an x-ray with the same energy as the incident x-ray, as shown in Figure 3.11. This not only greatly enhances the scattering cross section, but also enables the same elemental and valence state specificity that is afforded by XAS. REXS is a particularly powerful tool for probing modulations involving the partially occupied $3d$, $4f$, and $5f$ valence states of $3d$-transition metal, lanthanide, and actinide ions by tuning to the energy of the corresponding $2p \rightarrow 3d$ ($L_{2,3}$-edge), $3d \rightarrow 4f$ ($M_{4,5}$-edge), and $4d \rightarrow 5f$ ($N_{4,5}$-edge) dipole transitions, respectively, which generally involve beam energies in the 200-2000 eV range [42].

The resonant condition enhances the scattering cross section by virtue of the dispersion correction terms in Equation 3.1, $f'(\omega)$ and $if''(\omega)$, where the second term is imaginary because it represents dissipation in the system (i.e., absorption). While these terms are challenging to accurately predict for real systems and are often experimentally determined from XAS measurements, they can be calculated for scattering from a single electron using a forced charged oscillator model [11]. Suppose that a bound electron is subject to the electric field of an incident x-ray beam

$$\boldsymbol{E}_i = E_0 e^{-i\omega t}\hat{x}$$

where E_0 is the amplitude, ω is the frequency, and $\hat{x}$ is the direction of polarization. The equation of motion for the electron is then

[2]This name is actually somewhat of a misnomer, as it does not discriminate against inelastic scattering contributions, although they may be small compared to the elastic signal for many cases. Resonant *energy-integrated* x-ray scattering would be a more technically correct name for this technique. For this reason, it is commonly referred to by the broader name of *resonant soft x-ray scattering* (RSXS), which is colloquially understood not to include resonant inelastic x-ray scattering (RIXS).

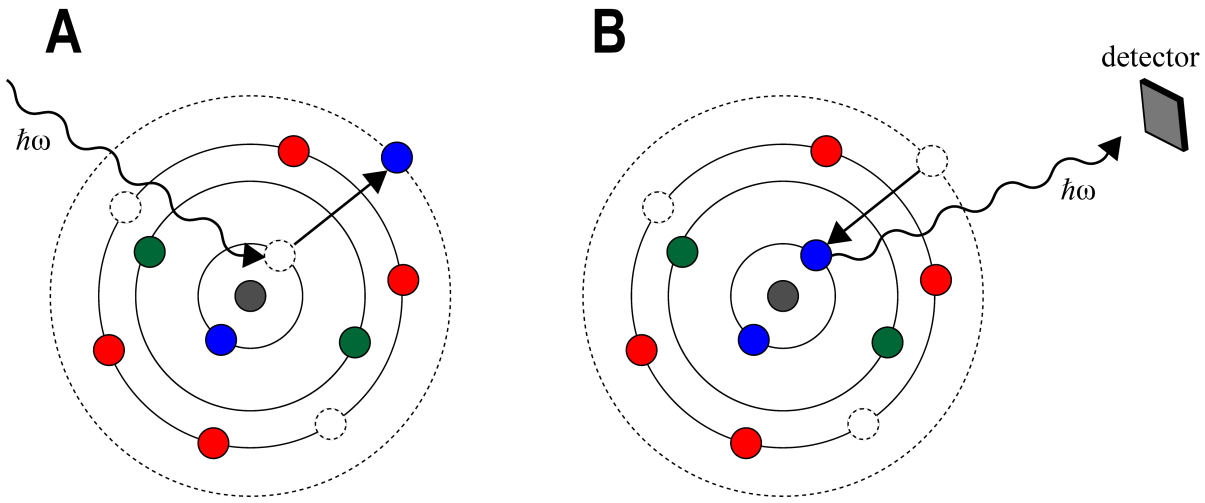

Figure 3.11: **A** In the resonant elastic x-ray scattering process, an incident x-ray with energy $\hbar\omega$ excites a core electron into an unoccupied state near the Fermi level, producing a core hole. **B** The electron then decays back into the core hole, emitting a photon with the same energy as the incident x-ray. Adapted from [28].

$$\ddot{x} + \Gamma\dot{x} + \omega_0^2 x = -\frac{eE_0}{m}e^{-i\omega t}$$

where the damping term, $\Gamma\dot{x}$, represents energy dissipation due to re-radiation of the applied field, with $\Gamma \ll \omega_0$. By substituting a solution of the form $x(t) = x_0 e^{-i\omega t}$, the amplitude of the forced oscillation, x_0, is

$$x_0 = -\frac{eE_0}{m}\frac{1}{\omega_0^2 - \omega^2 - i\omega\Gamma}$$

The radiated field measured a distance r at time t is proportional to the acceleration, $\ddot{x}$, at the prior time $t' = t - \frac{r}{c}$

$$E_r(r,t) = \frac{e}{4\pi\varepsilon_0 r c^2}\ddot{x}(t - \frac{r}{c})$$

The acceleration at time t' is

$$\begin{aligned}\frac{d}{dt}\left(x\left(t-\frac{r}{c}\right)\right) &= \ddot{x}\left(t-\frac{r}{c}\right)\\ &= -\omega^2 x_0 e^{-i\omega t} e^{i\frac{\omega}{c}r}\\ &= \frac{eE_0}{m}\frac{\omega^2}{\omega_0^2-\omega^2-i\omega\Gamma}e^{-i\omega t}e^{i\frac{\omega}{c}r}\end{aligned}$$

Substituting this into the equation for the radiated field yields

$$\begin{aligned}E_r(r,t) &= \frac{e^2}{4\pi\varepsilon_0 mc^2 r}\frac{\omega^2}{\omega_0^2-\omega^2-i\omega\Gamma}E_0 e^{-i\omega t}e^{i\frac{\omega}{c}r}\\ &= -r_0\frac{\omega^2}{\omega^2-\omega_0^2+i\omega\Gamma}E_0 e^{-i\omega t}\frac{e^{ikr}}{r}\end{aligned}$$

where $r_0 = \frac{e^2}{4\pi\varepsilon_0 mc^2}$ is the classical electron radius and $k = \frac{\omega}{c}$. The ratio of the radiated and incident fields is then

$$\frac{E_r(r,t)}{E_i} = -r_0\frac{\omega^2}{\omega^2-\omega_0^2+i\omega\Gamma}\frac{e^{ikr}}{r}$$

This equation describes an emitted spherical wave of the form $\frac{e^{ikr}}{r}$ with an amplitude of $-r_0\frac{\omega^2}{\omega^2-\omega_0^2+i\omega\Gamma}$. This amplitude corresponds to the *atomic scattering length*, which is expressed in units of $-r_0$. The atomic form factor, f, is then

$$f = \frac{\omega^2}{\omega^2-\omega_0^2+i\omega\Gamma}$$

Rewriting this expression yields

$$
\begin{aligned}
f &= \frac{\omega^2}{\omega^2 - \omega_0^2 + i\omega\Gamma} \\
&= 1 + \frac{\omega_0^2 - i\omega\Gamma}{\omega^2 - \omega_0^2 + i\omega\Gamma} \\
&\approx 1 + \frac{\omega_0^2}{\omega^2 - \omega_0^2 + i\omega\Gamma}
\end{aligned}
$$

where the approximation in the last line results from $\Gamma \ll \omega_0$. For high energy incident photons where $\omega \gg \omega_0$, the binding energy becomes negligible and the electron may be considered as unbound. This case yields $f \approx 1$, which corresponds to Thomson scattering by a free electron. Thus, the remaining term corresponds to the dispersion corrections

$$
f'(\omega) + if''(\omega) = \frac{\omega_0^2}{\omega^2 - \omega_0^2 + i\omega\Gamma}
$$

Separating the real and imaginary parts yields

$$
\begin{aligned}
f'(\omega) &= \frac{\omega_0^2(\omega^2 - \omega_0^2)}{(\omega^2 - \omega_0^2)^2 + (\omega\Gamma)^2} \\
f''(\omega) &= \frac{\omega_0^2\omega\Gamma}{(\omega^2 - \omega_0^2)^2 + (\omega\Gamma)^2}
\end{aligned}
$$

The dispersion correction terms for the single electron forced oscillator model are plotted in Figure 3.12. As shown, the dispersion corrections take their maximal values when the incident photon energy matches the resonant energy of the bound electron. Upon comparison of f'' (i.e., the absorption term) in Figure 3.12 to the XAS spectrum in Figure 3.3, it can be seen that the lineshape in real materials has an edge shape, rather than a peak. This is a limitation of the single electron forced oscillator model arising from the fact that there is only one resonant energy within

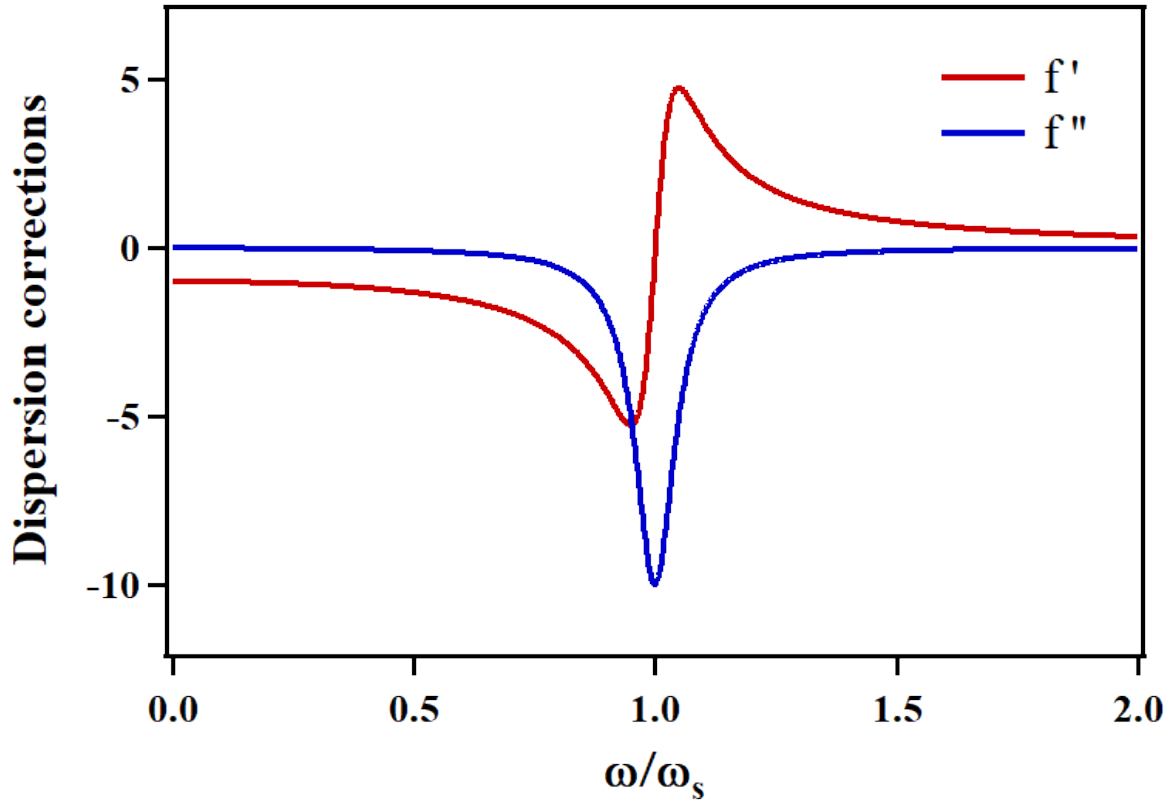

Figure 3.12: The real, f', and imaginary, f'', parts of the dispersion correction are shown as a function of the incident photon frequency, ω, relative to the resonant frequency, ω_0, for a single electron using a damped oscillator model. The damping coefficient, Γ, has been set to $0.1\omega_0$.

this model. In real materials, there is a continuum of states above the absorption edge which an electron may be excited into and each of these states has a corresponding resonant energy which yields the observed step-edge lineshape. To recover this edge shape, more elaborate modeling is required.

There are some inherent complications to working within these soft x-ray ranges. The set of accessible reciprocal lattice points may be very limited due to the reduced radius of the Ewald sphere at low energies. Additionally, because soft x-rays interact so strongly with matter, the penetration depth is significantly lower than for hard x-rays, oftentimes limiting the probe depth to $\sim$100 atomic layers or less, resulting in measurements which are more representative of the sample surface or near-surface, rather than its bulk. Unlike for hard x-rays, soft x-rays

also interact strongly with air, necessitating that the experiment be conducted within a scattering chamber held under ultra-high vacuum to prevent attenuation of the x-ray beam and subsequent scattering signal. This requirement introduces an additional layer of complexity to experimental logistics. Careful planning of sample mounting should be exercised as the vacuum systems make changing or adjusting samples non-trivial and add additional overhead due to the time required to pump down to the required vacuum levels, though these effects are somewhat mitigated by setups which include an interlock system. If working at low temperature, the choice of mounting adhesive should be carefully considered (e.g., opting for a strong silver paint or epoxy instead of carbon tape) as retrieving fallen samples requires breaking the vacuum in the scattering chamber can result in hours of experimental time loss and is often reserved for the end of the experiment. In some cases, warming up from low temperatures must be done slowly to prevent pressure spikes due to the sublimation of water which can cause valves along the beamline to automatically shut. While resonant scattering may increase the experimental complexity, these complications are compensated for by the significant increase in sensitivity to charge, orbital, and spin modulations.

3.4 Inelastic X-ray Scattering

The most familiar example of inelastic scattering is likely *Compton scattering*, where a photon with wavelength λ_i is incident upon an electron, as shown in Figure 3.13. Upon scattering, energy is transferred from the photon to the electron, causing it to recoil. The photon is subsequently scattered at some angle, θ, and its wavelength, λ_f, increases according to the relation [11]

$$\lambda_f = \lambda_i + \frac{h}{m_e c}(1 - \cos\theta)$$

where h is Planck's constant, m_e is the electron mass, and c is the speed of light, except for the trivial case where $\theta = 0$ and the scattering is elastic. More generally, he Hamiltonian describing

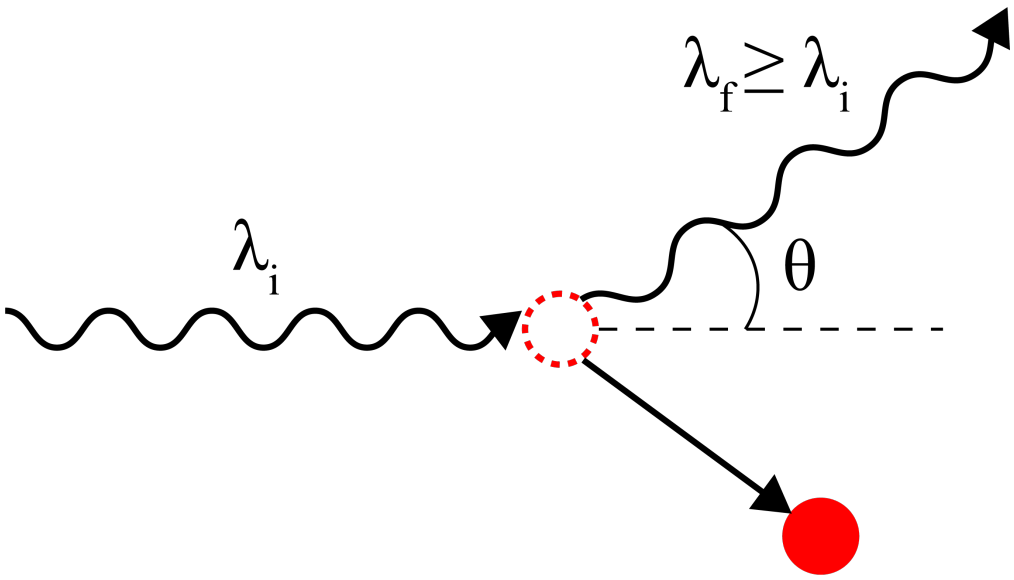

Figure 3.13: The Compton scattering process. A photon (black wavy lines) with wavelength λ_i is incident upon an electron (red circle), causing it to recoil. The photon is scattered at some angle, θ, and its wavelength, λ_f, increases by $\frac{h}{m_e c}(1-\cos\theta)$.

the interaction between the electromagnetic field of the incident x-ray and the electron is given by [43]

$$\mathcal{H}_{int} = \sum_j \frac{e^2}{2m_e c^2} \boldsymbol{A}_j^2 + \sum_j \frac{e}{m_e} \boldsymbol{p}_j \cdot \boldsymbol{A}_j$$

where e is the elementary charge, m_e is the electron mass, c is the speed of light, $\boldsymbol{p}_j$ is the momentum of the jth electron, and $\boldsymbol{A}_j$ is the vector potential. The first term is associated with non-resonant scattering (both elastic and inelastic), while the second term is associated with absorption (as discussed in Section 3.1) and resonant scattering.

The double differential cross section for inelastic x-ray scattering is given by the Kramers-Heisenberg formula [44]

$$\frac{d^2\sigma}{d\Omega d\omega_f} = \left(\frac{e^2}{m_e c^2}\right)^2 \left(\frac{\omega_f}{\omega_i}\right) \sum_f \left| (\boldsymbol{\varepsilon}_f \cdot \boldsymbol{\varepsilon}_i) \langle f | \sum_j e^{-i\mathbf{Q}\cdot\boldsymbol{r}_j} | i \rangle \right. \tag{3.2}$$

$$+ \frac{1}{m_e} \sum_n \left[\frac{\langle f | \sum_j (\boldsymbol{\varepsilon}_f \cdot \boldsymbol{p}_j) e^{i\boldsymbol{k}_f \cdot \boldsymbol{r}_j} | n \rangle \langle n | \sum_j (\boldsymbol{\varepsilon}_i \cdot \boldsymbol{p}_j) e^{i\boldsymbol{k}_i \cdot \boldsymbol{r}_j} | i \rangle}{E_i - E_n + \hbar\omega_i + \frac{i\Gamma}{2}} \right. \tag{3.3}$$

$$\left. \left. + \frac{\langle f | (\boldsymbol{\varepsilon}_i \cdot \boldsymbol{p}) e^{-i\boldsymbol{k}_i \cdot \boldsymbol{r}} | n \rangle \langle n | (\boldsymbol{\varepsilon}_f \cdot \boldsymbol{p}) e^{i\boldsymbol{k}_f \cdot \boldsymbol{r}} | i \rangle}{E_i - E_n + \hbar\omega_f + \frac{i\Gamma}{2}} \right] \right|^2 \delta\left(E_f - E_i - \hbar\omega\right) \tag{3.4}$$

where $\{\hbar\omega_i, \hbar\omega_f\}$ are the incident and scattered photon energies (with $\omega = \omega_f - \omega_i$), $\{\boldsymbol{\varepsilon}_i, \boldsymbol{\varepsilon}_f\}$ are the corresponding polarizations, $\{\boldsymbol{k}_i, \boldsymbol{k}_f\}$ are the corresponding wavevectors, $|i\rangle$ is the initial electronic state, $|n\rangle$ is the intermediate electronic state, $|f\rangle$ is the final electronic state, $\{E_i, E_n, E_f\}$ are the corresponding energies, and Γ is the excited state lifetime. This quantity describes the scattering of an x-ray from an initial state to a final state into some solid angle, $d\Omega$, with some momentum transfer, $\mathbf{Q}$, and into some energy bandwidth, $d\omega_f$. Upon inspection, it is easy to see that this expression is a generalized form of Fermi's golden rule (Appendix A). Only the first term is associated with non-resonant inelastic scattering

$$\frac{d^2\sigma}{d\Omega d\omega_f} = \left(\frac{e^2}{m_e c^2}\right)^2 \left(\frac{\omega_f}{\omega_i}\right) \left| (\boldsymbol{\varepsilon}_f \cdot \boldsymbol{\varepsilon}_i) \sum_f \langle f | \sum_j e^{-i\mathbf{Q}\cdot\boldsymbol{r}_j} | i \rangle \right|^2 \delta\left(\frac{E_f - E_i}{\hbar} - (\omega_f - \omega_i)\right)$$

which is commonly expressed as

$$\frac{d^2\sigma}{d\Omega d\omega_f} = \left(\frac{e^2}{m_e c^2}\right)^2 (\boldsymbol{\varepsilon}_f \cdot \boldsymbol{\varepsilon}_i)^2 \left(\frac{\omega_f}{\omega_i}\right) S(\mathbf{Q}, \omega)$$

where $S(\mathbf{Q}, \omega)$ is called the *dynamic structure factor*. The quantity preceding the dynamic structure factor, $\left(\frac{e^2}{m_e c^2}\right)^2 (\boldsymbol{\varepsilon}_f \cdot \boldsymbol{\varepsilon}_i)^2 \left(\frac{\omega_f}{\omega_i}\right)$, is called the *Thomson scattering cross section* and acts as a scale factor that is related to the probe-sample interaction [45]. $S(\mathbf{Q}, \omega)$ may therefore

be regarded as essentially equivalent to the scattering cross section as it is the quantity which is proportional to the experimentally measured intensities. The dynamic structure factor is a generalization of the structure factor discussed in Section 3.2 that considers correlations in *time*, as well as space. This allows IXS to probe the dynamics of a system, whereas elastic scattering is used to probe its static structure.

Modern synchrotron light sources are able to measure IXS spectra with meV resolution, enabling the measurement of phonon dispersions, which is one of the most common applications of the IXS technique. IXS experiments are conducted using an IXS spectrometer, which is essentially a large x-ray diffractometer that can scan the photon energy. An example schematic for an IXS spectrometer is shown in Figure 3.14.

The IXS spectrometer operates by passing the x-ray beam through a high-resolution monochromator, which can reduce the bandwidth of the x-ray beam to the meV level [46]. The beam is scattered by the sample before passing through an analyzer crystal that also has a resolution on the order of meV. To perform an IXS measurement, the analyzer angle (2θ) is first moved to the desired momentum transfer ($\mathbf{Q}$). The energy of the incident x-ray beam is then scanned while the position and analyzer energy are held fixed. The resulting spectrum is produced as a function of energy transferred to the sample with an intensity that is proportional to $S(\mathbf{Q}, \omega)$. A generic IXS spectrum can be seen in Figure 3.15, which illustrates the typical energy and lineshape for a variety of excitations which may be probed by IXS. To measure a phonon

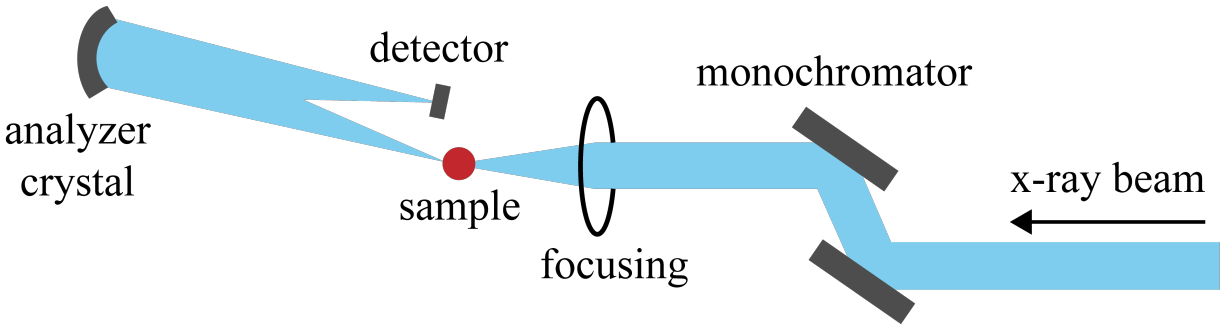

Figure 3.14: An example schematic for an IXS spectrometer. Adapted from [46].

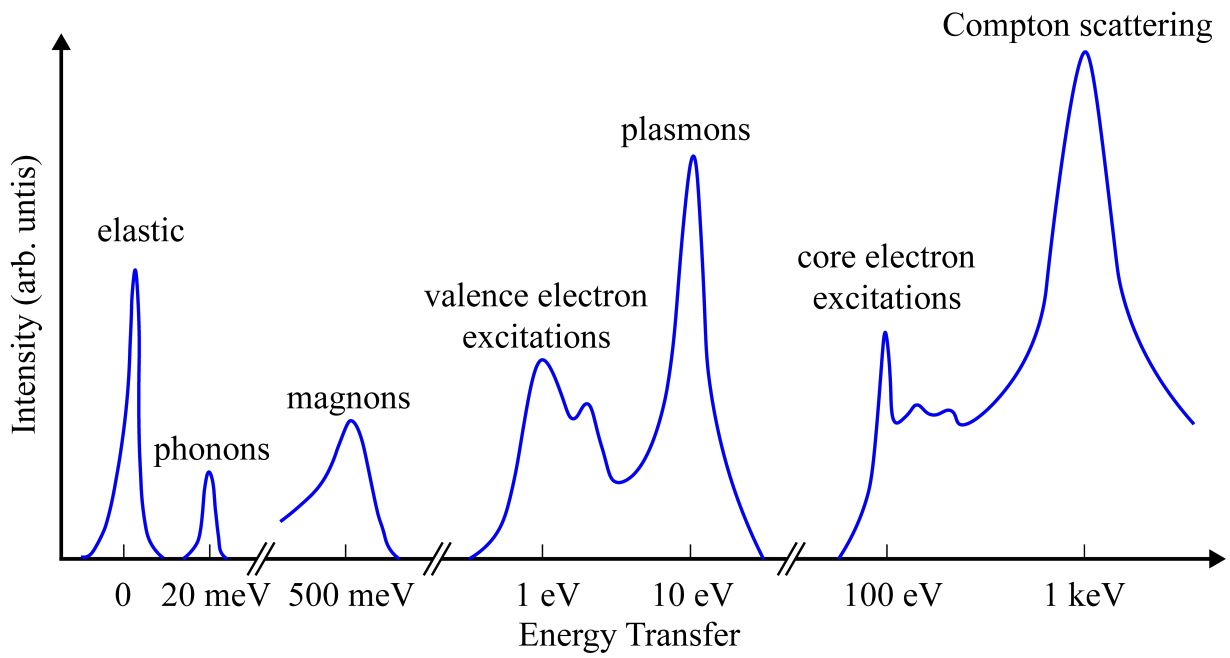

Figure 3.15: A typical inelastic x-ray scattering (IXS) spectrum. IXS is able to probe a variety of excitations over a broad range of energies. Adapted from [24].

dispersion, for example, this process would be repeated with the analyzer positioned at various points along the desired reciprocal space path of the phonon while scanning an appropriate energy range at each point.

3.5 Resonant Inelastic X-ray Scattering

The final technique being discussed is *resonant inelastic x-ray scattering* (RIXS). The most straightforward way to understand the RIXS technique is through a comparison to XAS. In Section 3.1, it was discussed that one of the common ways to measure an absorption spectrum is by the total fluorescence yield, in which all photons emitted by the core hole decay are indiscriminately collected by the detector as a function of incident beam energy. RIXS may be thought of as an extension of XAS, whereby the spectrum of emitted photons within the total fluorescence yield signal is measured for each incident beam energy. In other words, integrating the RIXS spectra yields the absorption spectrum.

Similar to reflection-mode XAS, the RIXS process involves the excitation of a core electron to an empty valence state, creating a core hole, and measures the products of the core hole decay. Unlike XAS, however, the Auger electron decay channel is not relevant to RIXS as only the fluorescence is measured. RIXS processes are distinguished as being either *direct* or *indirect*, as illustrated in Figure 3.16.

In both RIXS processes, an incident x-ray with wavevector $\boldsymbol{k}_{in}$ and energy $\hbar\omega_{in}$ is absorbed by a core electron, creating a core hole. In the direct RIXS process, the core electron is promoted to an empty valence state near the Fermi energy, E_F. An electron in a different valence state decays into the core hole, emitting a photon with wavevector $\boldsymbol{k}_{out}$ and energy $\hbar\omega_{out}$ while also creating a hole in the valence band. This hole and the initially photoexcited electron form an electron-hole excitation with momentum $\hbar\mathbf{Q} = \hbar(\boldsymbol{k}_{out} - \boldsymbol{k}_{in})$, where $\mathbf{Q}$ is the momentum transfer vector, and energy $\hbar\omega = \hbar(\omega_{out} - \omega_{in})$ which can propagate through the system. Both the initial photoexcitation and subsequent decay must involve dipole-allowed transitions in order for this direct RIXS process to be observed. In these cases, direct processes dominate the measured RIXS spectra with any indirect processes only provide higher-order contributions.

In the indirect RIXS process, the core electron is excited into an empty state several eV above E_F. A different electron in the valence band scatters from the potential of the core hole, creating an electron-hole excitation in the valence band. The initially photoexcited electron then decays into the core hole, emitting a photon with with wavevector $\boldsymbol{k}_{out}$ and energy $\hbar\omega_{out}$. If not for the electron-hole excitation induced by scattering from the core hole potential, this process would be elastic with $\boldsymbol{k}_{out} = \boldsymbol{k}_{in}$ and $\hbar\omega_{out} = \hbar\omega_{in}$. Thus, the momentum and energy of the electron-hole valence band excitation is again $\hbar\mathbf{Q} = \hbar(\boldsymbol{k}_{out} - \boldsymbol{k}_{in})$ and $\hbar\omega = \hbar(\omega_{out} - \omega_{in})$, respectively. This indirect process only dominates the RIXS spectra in cases where direct processes are forbidden.

In either process, the change in energy and momentum (and polarization) of the scattered x-ray photon is transferred to excitations that are intrinsic to the system. Information about these excitations is therefore obtained by measuring the changes between the incident and emitted

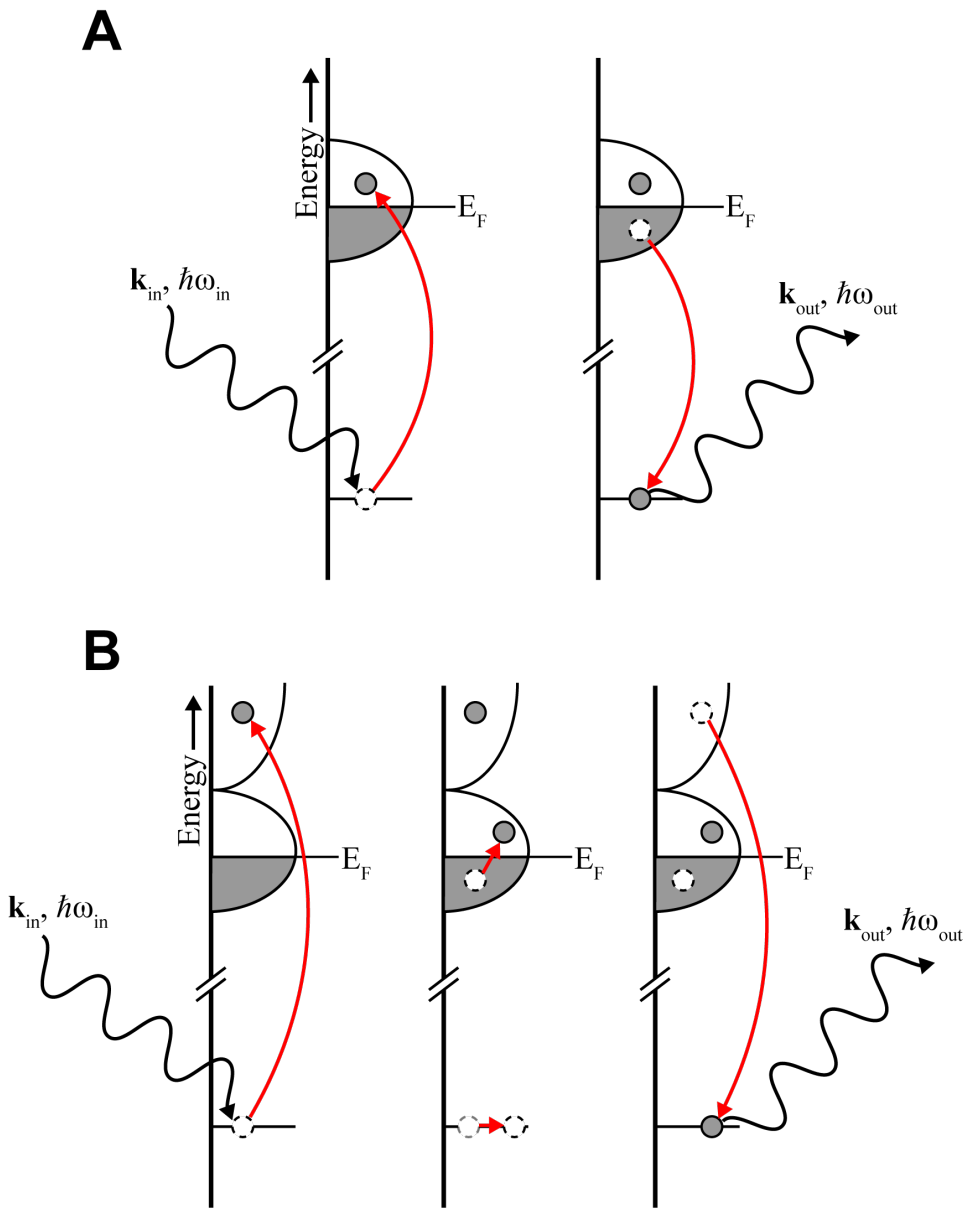

Figure 3.16: In both resonant inelastic x-ray scattering (RIXS) processes, an incident x-ray with wavevector $\boldsymbol{k}_{in}$ and energy $\hbar\omega_{in}$ is initially absorbed by a core electron, creating a core hole (left). In both final states, a photon with wavevector $\boldsymbol{k}_{out}$ and energy $\hbar\omega_{out}$ is emitted by the core hole decay, resulting in a valence band excitation with momentum $\hbar\mathbf{Q} = \hbar(\boldsymbol{k}_{out} - \boldsymbol{k}_{in})$ and energy $\hbar\omega = \hbar(\omega_{out} - \omega_{in})$ (right). **A** In the direct RIXS process, the core electron is excited into an empty valence state near the Fermi energy, E_F. A different electron in the valence band decays into the core hole. **B** In the indirect RIXS process, the core electron is excited into an empty state several eV above E_F. The valence band excitation arises in an intermediate state due to scattering by the potential of the core hole (middle). The initially photoexcited electron decays back into the core hole. Adapted from [47].

photons. Because the incident beam energy is tuned to an absorption edge, the inelastic scattering cross section may be greatly enhanced, as described by the final term in Equation 3.2. As similarly discussed in Section 3.3, this resonance condition can result in a significantly enhanced sensitivity to phenomena arising from the charge, orbital, or spin degrees of freedom of a small fraction of valence electrons which may be otherwise difficult to observe with non-resonant x-rays in which the scattering interactions are mostly dominated by core electrons. Some intrinsic excitations that can be probed by RIXS include phonons, magnons, plasmons, charge-transfer excitations (i.e., electrons hopping from one site to another), and *dd* excitations (i.e., crystal-field transitions between different *d* orbitals) [47]. A generic RIXS spectrum illustrating the typical energy range and lineshape of some commonly measured excitations is shown in Figure 3.17 as a function of incident x-ray energy loss. Because different excitations may dominate the spectrum for slightly different resonant energies, a typical RIXS experiment generally involves measuring the RIXS spectrum over a range of different incident beam energies around an absorption edge.

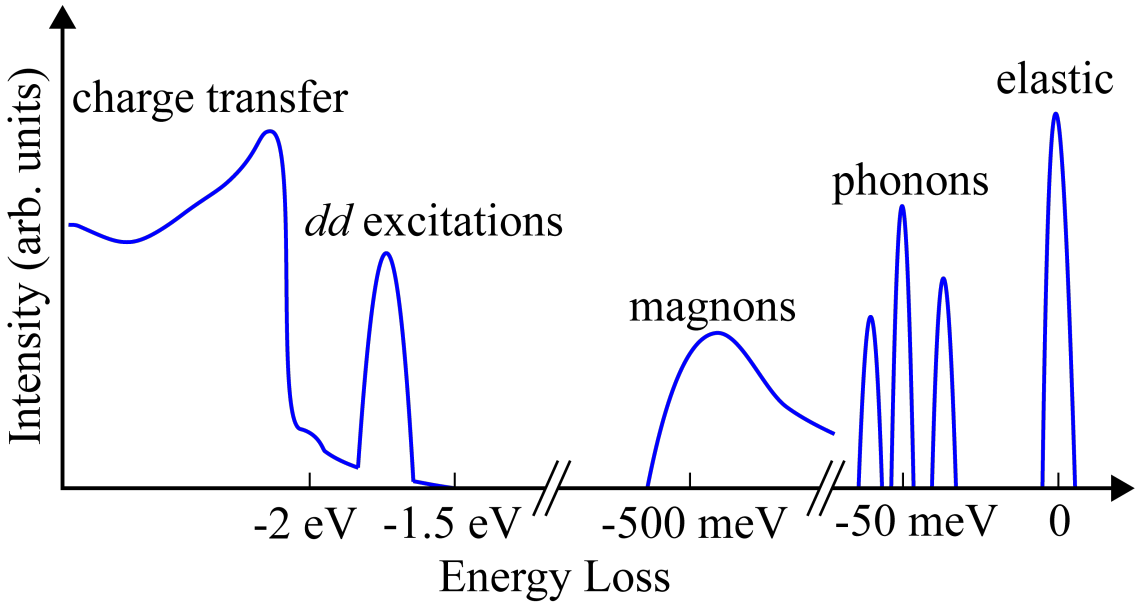

Figure 3.17: A generic resonant inelastic x-ray scattering (RIXS) spectrum as a function of incident x-ray energy loss. The typical energy range and lineshape are illustrated for various excitations that are commonly measured by RIXS. Adapted from [47].

Chapter 4

Pr Substitution in YBCO

4.1 The Cuprates

The cuprates, which, in this context, refer specifically to the subclass of inorganic oxides with the generalized formula $XYCu_mO_n$, became the most heavily studied class of materials practically overnight, following the discovery of high-temperature superconductivity (SC) in a Ba–La–Cu–O system by German physicist Georg Bednorz and Swiss physicist Alex Müller in 1986 [38] that would define the focal point of condensed matter research in the late 1980's and early 1990's. Unlike conventional SC, which was discovered unintentionally decades earlier by Dutch physicist Kamerlingh Onnes while liquefying helium [48], there is no known theoretical framework which completely describes the mechanisms responsible for stabilizing the high-temperature version of SC, which remains as one of the most enigmatic outstanding problems in condensed matter physics to this day.

The cuprate phase diagram (Figure 4.1) has proven to be far more extensive and complex than initially assumed, hosting a multitude of exotic phases beyond just high-temperature SC, including charge order [50], spin [51] and pair [52] density waves, pseudogap states [53], and nematicity [54]. The origin of these diverse electronic phases emanates from the intricate

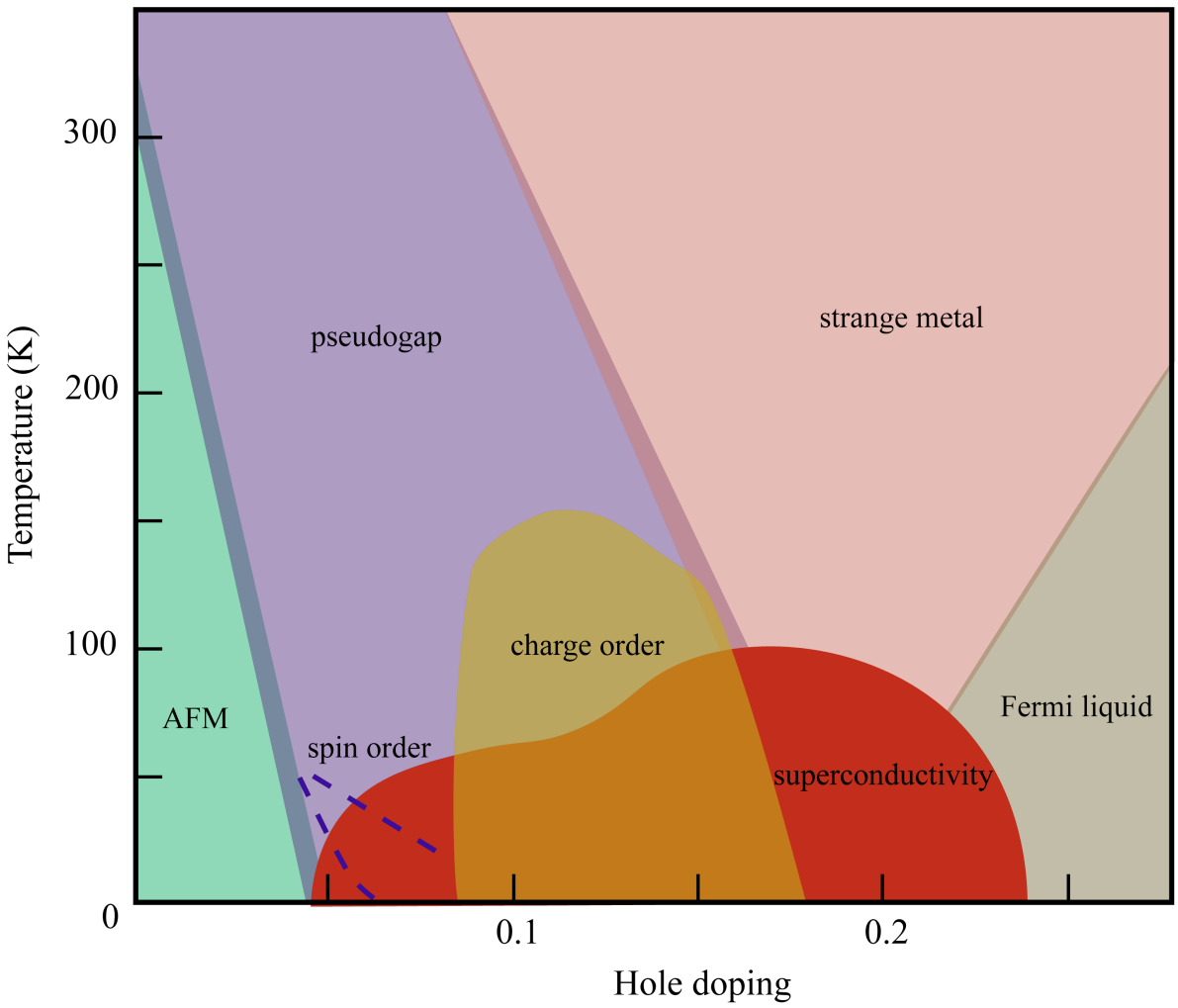

Figure 4.1: A generic cuprate phase diagram is illustrated as a function of temperature versus hole doping and contains many distinct phases, including antiferromagnetism (AFM), superconductivity (SC), and spin and charge order. Adapted from [49].

interactions between competing charge, spin, orbital, and lattice degrees of freedom which govern the physics of the quasi-two-dimensional (2D) CuO_2 planes (Figure 4.2) that are ubiquitous to all cuprates [55]. While the CuO_2 planes are initially in an antiferromagnetic (AFM) state due to strong Coulomb repulsion that localizes electrons to lattice sites, SC and other phases can be induced by doping the system with holes, allowing the interaction of itinerant charge carriers. These interactions within the CuO_2 planes are predominately influenced by the underlying

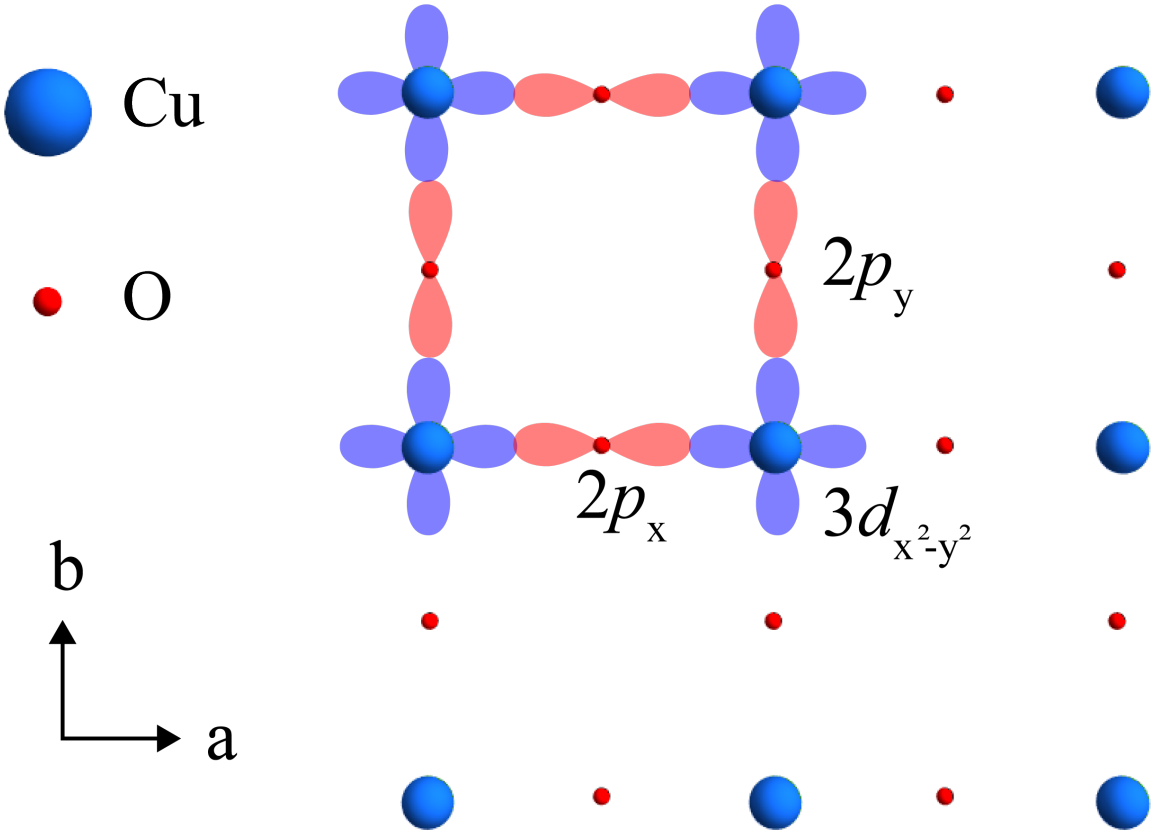

Figure 4.2: The CuO_2 plane is ubiquitous to all cuprates. The orientation of Cu and O atoms, along with their active $3d_{x^2-y^2}$ and $2p_{x,y}$ orbitals, respectively, is shown.

characteristics of the planar Cu $3d_{x^2-y2}$ orbitals that dominate the density of states near the Fermi surface as a result of a substantial energy splitting of the e_g orbitals [56]. The 2D character of the surviving $d_{x^2-y^2}$ orbital can be directly observed by transport measurements, as evidenced by the anisotropy between the in-plane and out-of-plane electrical and thermal conductances [57]. Understanding the interplay between the phases arising from the interactions of these electronic states remains an active focus of condensed matter research.

4.1.1 The PYBCO System

The most heavily studied cuprate is undoubtedly $YBa_2Cu_3O_{6+\delta}$ (YBCO). Although the SC critical temperature (T_c) of YBCO is not the highest of the cuprates at $T_c \approx 92$ K [58], it does

have some unique features which set it apart from other members of its family. One interesting property of YBCO is that its unit cell contains two CuO_2 planes, whereas most other cuprates only contain one per unit cell. The most notable unique property of YBCO, however, is the formation of Cu-O chains upon oxygen doping. As shown in Figure 4.3, $YBa_2Cu_3O_6$ has a tetragonal perovskite structure belonging to the *P4/mmm* point group with lattice constants $a = b \approx 3.86$ Å and $c \approx 11.82$ Å [59]. Adding additional oxygen results in the formation of Cu-O chains along the *b* axis, as can be seen for the $YBa_2Cu_3O_7$ unit cell. The formation of these chains causes the *b* lattice parameter to expand while the *a* and *c* lattice parameters contract, causing the unit cell to eventually become orthorhombic with a point group of *Pmmm*. The loss of tetragonality in $YBa_2Cu_3O_{6+\delta}$ occurs for $\delta \gtrsim 0.35$, culminating in the lattice parameter *a*=3.82 Å, *b*=3.89 Å, and *c*=11.67 Å for $\delta \approx 1$ [60], as shown in Figure 4.4, which yields an orthorhombic distortion of $\frac{b-a}{b+a} = 0.009$.

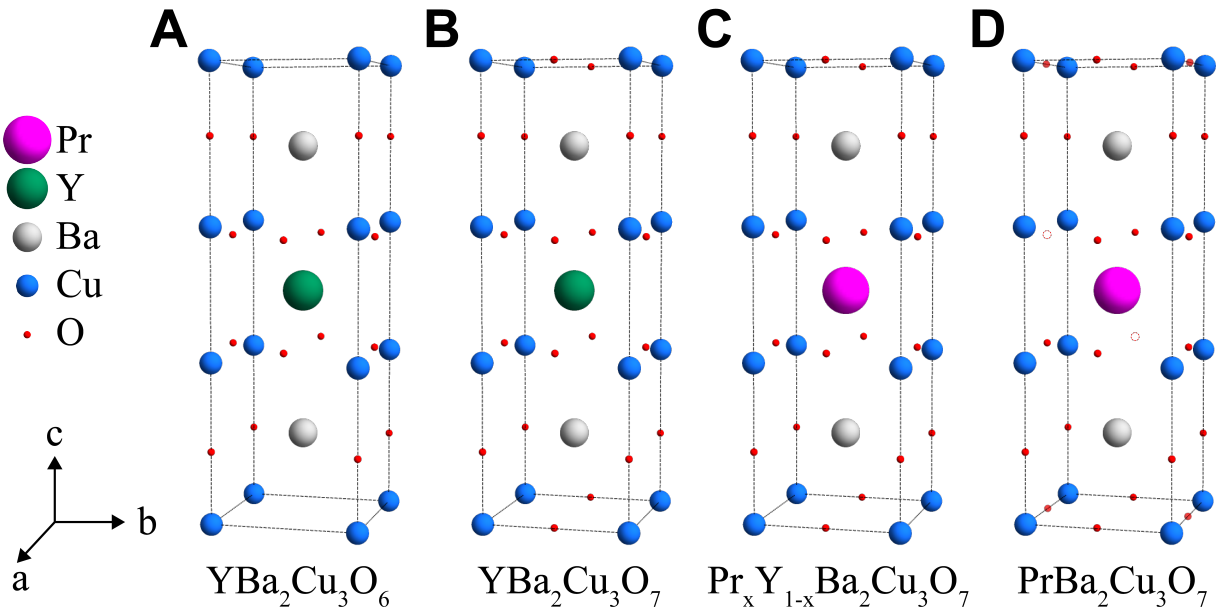

Figure 4.3: **A** The tetragonal unit cell for $YBa_2Cu_3O_6$. **B** The unit cell for $YBa_2Cu_3O_7$ is orthorhombic due to the additional O atoms forming Cu-O chains along the **b** direction. **C** For for $x \lesssim 0.9$, the $Pr_xY_{1-x}Ba_2Cu_3O_7$ system has a percentage, *x*, of the $YBa_2Cu_3O_7$ cells in which the central Y atom has been replaced by Pr. **D** The $PrBa_2Cu_3O_7$ unit cell becomes tetragonal again due to relocating O from the CuO_2 planes to the anti-chain sites.

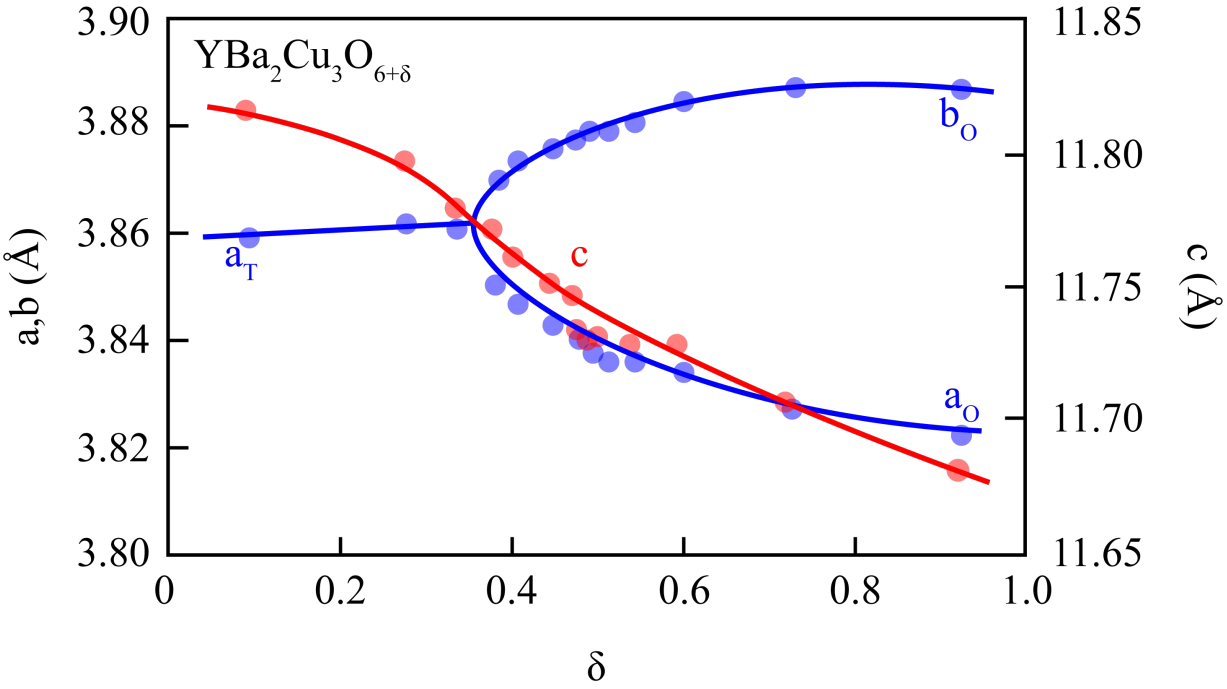

Figure 4.4: The evolution of the a, b and c lattice parameters are shown for $YBa_2Cu_3O_{6+\delta}$ as a function of O content, δ. Adapted from [59].

The majority of the research contained within this dissertation involves studying the $YBa_2Cu_3O_7$ system with some percentage, x, of the yttrium (Y) sites substituted by praseodymium (Pr), forming $Pr_xY_{1-x}Ba_2Cu_3O_7$ (PYBCO). This material was chosen because, unlike substituting Y by any other rare-earth element (except for Ce and Tb, which do not form the YBCO structure, instead forming the non-isostructural perovskites $BaCeO_3$ and $BaTbO_3$, respectively [61]), Pr-substitution does not yield a similar transition temperature ($T_c \approx 90$ K) but instead continuously decreases it until destroying the transition altogether for $x \gtrsim 0.5$, as shown in Figure 4.5, which compares the phase diagrams of $YBa_2Cu_3O_{6+\delta}$ and $Pr_xY_{1-x}Ba_2Cu_3O_7$ as functions of O and Pr content, respectively. Therefore, $PrBa_2Cu_3O_7$ (PBCO) constitutes the singular material homomorphic to YBCO which uniquely demonstrates a complete lack of SC, resulting in one of the most controversial findings within the field of cuprate SC [62, 63].

The suppression of T_c has been demonstrated not to be a result of simple hole filling due to an enhanced valency of the Pr ion [66]. The loss of SC resulting from Pr-substitution at

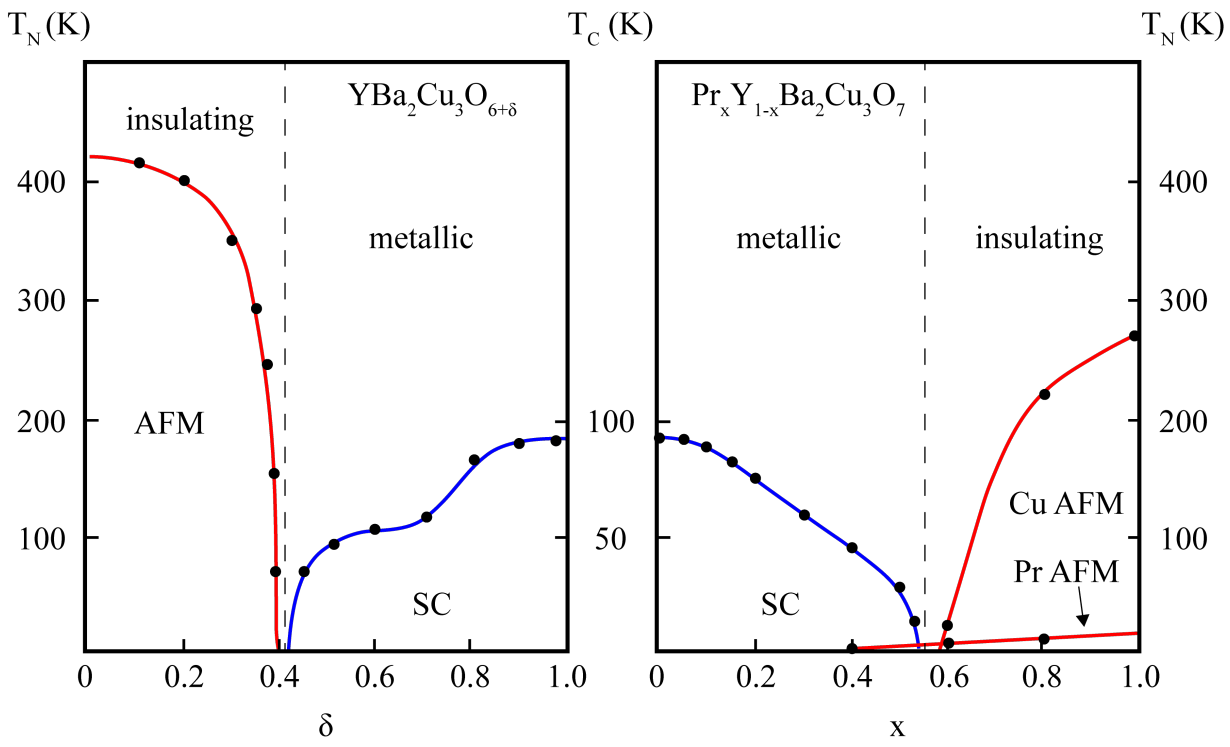

Figure 4.5: The phase diagrams for $YBa_2Cu_3O_{6+\delta}$ (left) and $Pr_xY_{1-x}Ba_2Cu_3O_7$ (right) are shown as functions of O, δ, and Pr, x, respectively. Adapted from [64, 65].

the Y site is instead largely attributed to orbital hybridization between the Pr $4f$ and planar O $2p_\pi$ electronic states [67, 68]. In YBCO, the planar O $2p_\sigma$ and Cu $3d_{x^2-y^2}$ orbitals hybridize to form so-called Zhang-Rice singlets, which are thought to play a crucial role in the mechanism of cuprate SC [69]. It has been shown that Pr-substitution localizes initially itinerant holes from these Zhang-Rice states into energetically favorable O $2p_\pi$ states that are hybridized with Pr $4f$ orbitals, known as Fehrenbacher-Rice states [70–72]. However, despite the successfulness of this theoretical framework, it remains actively debated whether the effects of hybridization alone can account for the high rate of T_c suppression observed in $Pr_xY_{1-x}Ba_2Cu_3O_7$ [73].

As the Pr content increases, the orthorhombic symmetry is initally preserved but the degree of orthorhombic distortion is continuously reduced until the lattice eventually becomes tetragonal. Figure 4.6 displays the data collected by [74], in which a tetragonal phase is observed for $x \geq 0.9$

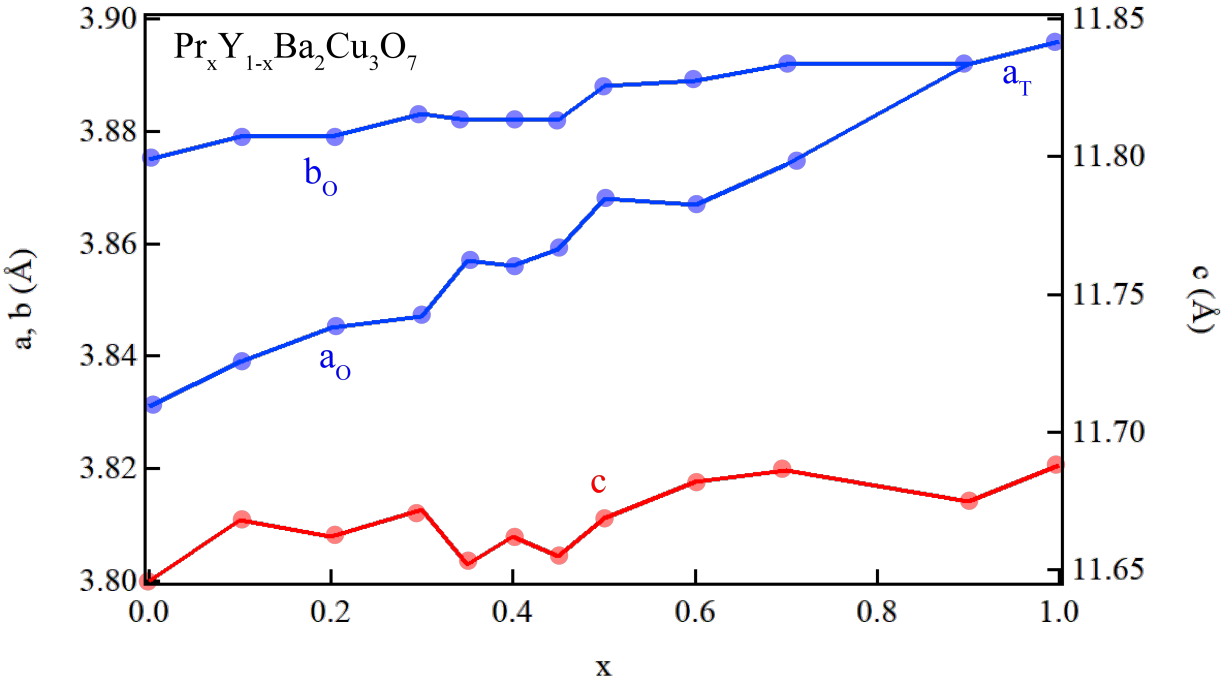

Figure 4.6: The evolution of the a, b and c lattice parameters are shown for $Pr_xY_{1-x}Ba_2Cu_3O_7$ as a function of Pr content, x.. Adapted from [74].

with lattice parameters $a = b = 3.896$ Å and $c = 11.688$ Å for $PrBa_2Cu_3O_7$. Wile most studies report observing a tetragonal phase for $x \gtrsim 0.9$ [74–77], it has been shown that the loss of orthorhombicity is heavily influenced by the growth and cooling procedures employed during the material synthesis [63] and that it is possible to produce PBCO which remains orthorhombic [78], ultimately depending upon the macroscopic ordering of the Cu-O chains [79]. For example, [80] reports finding that the orthorhombic distortion is drastically reduced to $\frac{b-a}{b+a} = 0.0007$ with a Pr content of only $x = 0.3$, which decreases further to 0.0006 for PBCO ($x = 1$), rather than becoming fully tetragonal.

Although both $YBa_2Cu_3O_6$ and $PrBa_2Cu_3O_7$ share a tetragonal symmetry, the a and b lattice parameters are larger in $PrBa_2Cu_3O_7$, being roughly equal to the b lattice parameter of $YBa_2Cu_3O_7$. This is because, although the tetragonality is lost or obtained by alteration of the Cu-O chain layer for both $YBa_2Cu_3O_{6+\delta}$ and $Pr_xY_{1-x}Ba_2Cu_3O_7$, respectively, the underlying mechanisms are slightly different. Tetragonality is lost in $YBa_2Cu_3O_{6+\delta}$ as the O content

increases, resulting in the formation of Cu-O chains along the b direction, hence $YBa_2Cu_3O_6$ is tetragonal because these Cu-O chains are absent, being instead replaced by a simple Cu plane. In contrast, as Pr is substituted into $YBa_2Cu_3O_7$, which already contains fully formed Cu-O chains, rather than O atoms being lost from the chain sites, O is instead added to the anti-chain sites, effectively forming Cu-O chains along the a direction, as well, resulting in what is essentially another CuO_2 plane [78]. This explains why the b lattice parameter remains nearly constant with increased Pr content, while the a lattice parameter continuously increases until $a = b$ and tetragonality is induced. Unlike for YBCO, the source of the O which populate the anti-chain sites in PYBCO is non-trivial, since it occurs when substituting Pr into the system instead of adding O. Thus, because the Pr-substitution does not significantly alter the O content [74, 78], the O which induces tetragonality by population of the anti-chain sites must come from within the lattice. Because the O within the Ba-O layer is necessary for structural integrity, the only remaining option is that the O is taken from the CuO_2 planes, which has been experimentally verified by scanning tunneling microscopy measurements [80].

It has been argued that the creation of O vacancies in the CuO_2 planes that is necessary to induce tetragonality is resultant from an aliovalent substitution, with the only two possibilities being $Pr^{4+} \rightarrow Y^{3+}$ or $Pr^{3+} \rightarrow Ba^{2+}$ [80]. As discussed earlier, it has been shown that the substituted Pr is trivalent, suggesting that $Pr^{3+} \rightarrow Ba^{2+}$ substitution is responsible for this phenomenon. Subsequently, there have been several reports of unintended substitution by some of the Pr ions at the Ba sites [81–83]. Furthermore, it has been shown that, by intentional substitution Pr at the Ba site instead of the Y site, tetragonality can be induced with as little as 10% Pr content [84]. Additionally, the 10% Pr substitution at the Ba site was accompanied by a reduction of T_c to only 10.2 K, compared to a T_c of 76.6 K for the same Pr content when substituted at the Y site. It has been hypothesized that Pr-substitution at the Ba site may be responsible for the lack of SC in PBCO through magnetic pair breaking and that SC in PBCO may be achieved by reducing Ba-site solubility of the Pr ion [84, 85]. Interestingly, there have been two such reports of observed

inhomogeneous SC in PBCO [85, 86]. However, there are no reports that these results have been reproduced and, even if the observations are true, the inhomogenous SC is not commensurable to the bulk SC observed in YBCO and when substituted by other rare-earths.

4.2 Results

4.2.1 Experimental Details

Sample Synthesis

All samples of $Pr_xY_{1-x}Ba_2Cu_3O_7$ were grown as single crystals by collaborator Prof. Brian Maple's group (UC San Diego) using the methods described in [87]. The starting materials used for the crystal growth consisted of 99.99% pure CuO, $BaCO_3$, Pr_6O_{11}, and Y_2O_3 powders. The crystals were annealed in flowing O to maintain full oxygenation. The SC transition temperatures were determined by magnetization measurements performed with a vibrating sample magnetometer in a Quantum Design DynaCool Physical Property Measurement System.

Experimental Setup

All x-ray scattering and spectroscopy experiments were conducted at synchrotron light sources using a horizontal scattering geometry, as shown in Figure 4.7. The scattering plane is defined by the plane spanned by the incident and scattered wavevectors, $\boldsymbol{k}_{in}$ and $\boldsymbol{k}_{out}$, respectively, which are typically aligned to the HK or KL reciprocal space planes, which correspond to the ac and bc crystal lattice planes of the sample, respectively. X-rays with σ polarization are oriented such that the electric field of the incident x-ray oscillated within the CuO_2 planes, whereas the electric field of incident x-rays with π polarization oscillate along the c crystal axis. The scattering vector, $\mathbf{Q}$, is defined by $\boldsymbol{k}_{out} - \boldsymbol{k}_{in}$. A schematic of the four-circle geometry used in the x-ray scattering experiments can be seen in Figure 3.10.

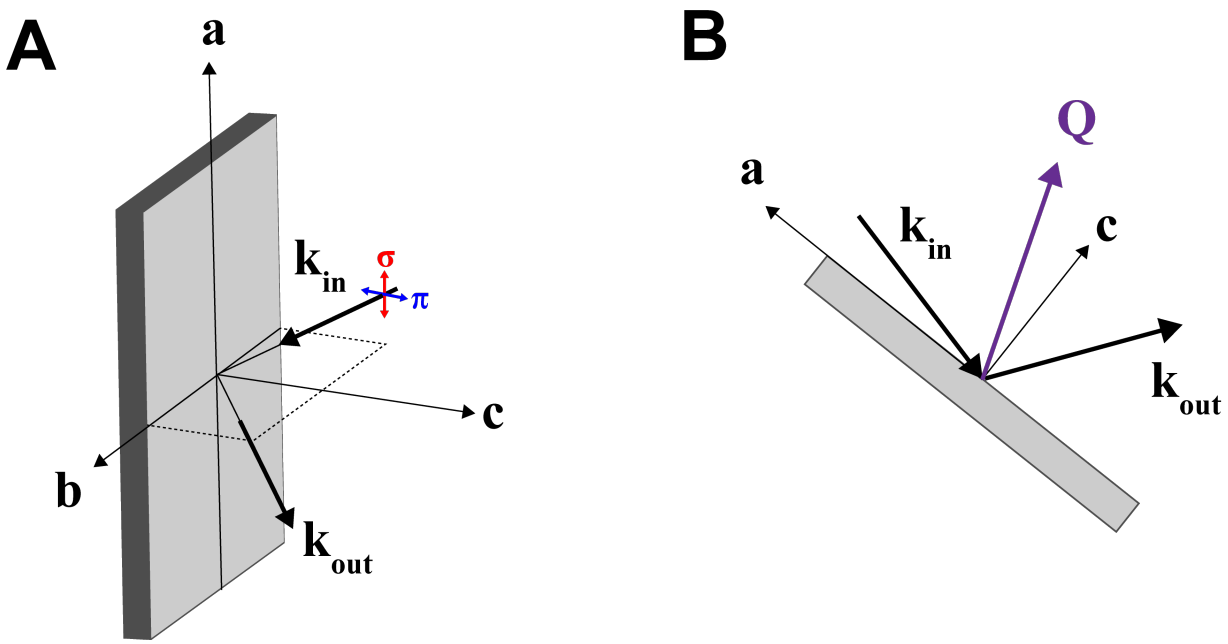

Figure 4.7: **A** An example experimental setup scattering into the *KL* plane is shown. The directions of oscillation of the electric field of the incident x-ray photon with wavevector $\boldsymbol{k}_{in}$ is indicated by arrows for σ (red) and π (blue) polarization. The incident and scattered (wavevector $\boldsymbol{k}_{out}$) x-rays define the scattering plane (dotted lines). **B** A side view of the scattering geometry. The scattering vector, **Q**, is defined by $\boldsymbol{k}_{out} - \boldsymbol{k}_{in}$.

4.2.2 Comparison of PBCO and YBCO

As discussed in Section 4.1.1, Pr is the only rare earth element which suppresses SC in the YBCO system while retaining its structure [62, 63]. From a comparison of the YBCO and PYBCO phase diagrams (Figure 4.5), parallels can be drawn between the behaviors of decreasing O in YBCO with increasing Pr in PYBCO, though by a different mechanism than simple hole filling [66]. To obtain further insights about the differences in electronic structure of these two systems, x-ray absorption spectroscopy (XAS) and resonant inelastic x-ray scattering (RIXS) techniques were used to compare samples of $YBa_2Cu_3O_7$ and $PrBa_2Cu_3O_7$.

XAS

The samples of YBCO and PBCO measured by XAS are shown in Figure 4.8. The x-ray absorption spectra can be seen in Figure 4.9 both π and σ polarizations. The XAS spectra were

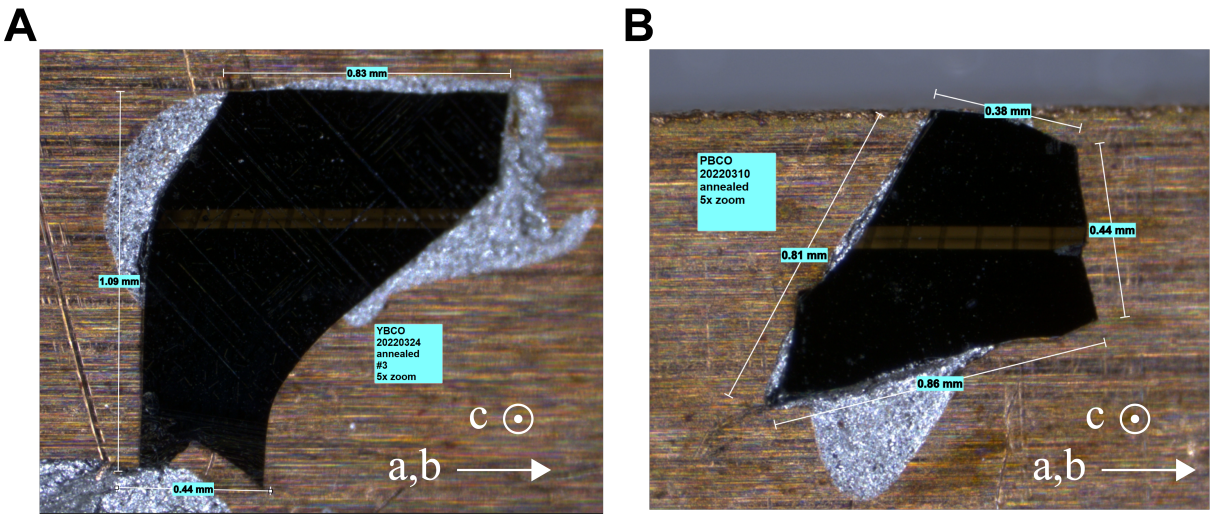

Figure 4.8: The **A** YBCO and **B** PBCO samples measured by XAS are shown.

collected at the ADRESS X03MA beamline of the Swiss Light Source at the Paul Scherrer Institute (PSI, Switzerland). The XAS data was normalized using Larch [88]. All spectra were collected at $T = 16$ K under ultrahigh vacuum in the TEY channel at grazing incidence (15°). Both samples were polished to reduce surface defects. All XAS measurements were normalized by the incident photon flux. The YBCO sample that was measured yielded a SC critical temperature of $T_c = 86$ K, indicating that the O content is slightly below optimal doping levels. No T_c was measured for PBCO as it is not superconductive.

In the YBCO spectra, both the Cu L_3 (931.2 eV) and L_2 (951.5 eV) absorption edges can be seen, corresponding to the $2p_{\frac{3}{2}} \rightarrow 3d$ and $2p_{\frac{1}{2}} \rightarrow 3d$ transitions, respectively. It may be easily observed that the absorption coefficient, μ, is significantly higher for incident x-rays in which the electric field oscillates in-plane (σ-polarization) than for incident x-rays in which the electric field oscillates out-of-plane (π-polarization). This anisotropy directly highlights the quasi-2D character of the dominant $3d_{x^2-y^2}$ orbital. A weaker satellite peak can be observed at higher energy for both the L_3 934.4 eV and L_2 edges at 934.4 eV and 954.2 eV, respectively, which corresponds to the decreased valency of the Cu^{1+} ($3d^{10}$) ions in the Cu-O chain layer compared to the Cu^{2+} ($3d^9$) ions in the CuO_2 plane layers [89]. Because the Cu^{1+} valence state only occurs for Cu ions which

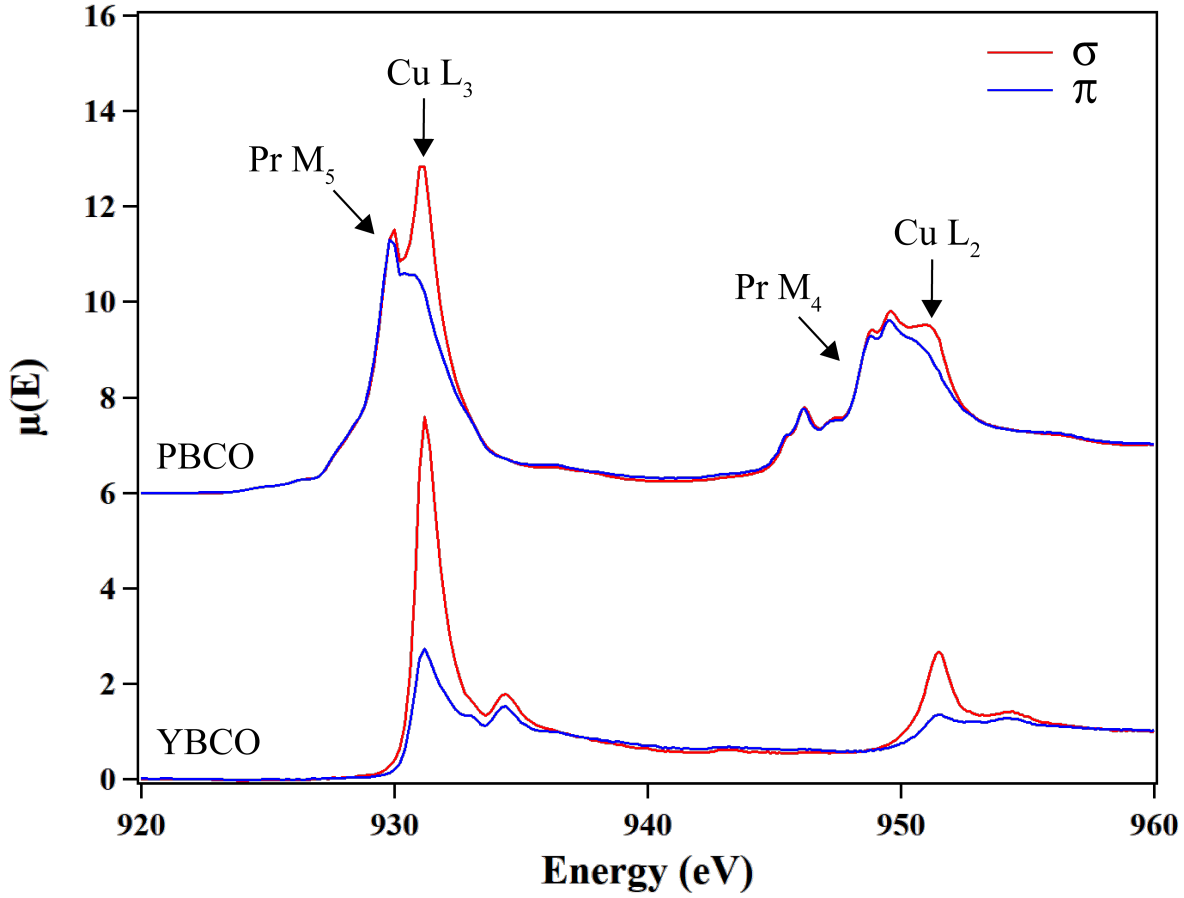

Figure 4.9: The normalized x-ray absorption spectra measured by the total electron yield channel is shown for YBCO (bottom) and PBCO (top). The π polarization (blue) aligns the electric field of the incoming x-ray photon with the *c*-axis, whereas the electric field oscillates in-plane for the σ polarization (red).

have not formed Cu-O chains, this confirms that the O content is below optimal doping levels.

The absorption spectra for PBCO unsurprisingly display similar features at the Cu L_3 and L_2 edges as for YBCO. The satellite peaks corresponding to unfilled Cu-O chains is absent, confirming that the sample is fully oxygenated, as expected. In addition to the Cu edges are the Pr M_5 (930.0 eV) and M_4 (949.6 eV) absorption edges, corresponding to the $3d_{\frac{5}{2}} \rightarrow 4f$ and $3d_{\frac{3}{2}} \rightarrow 4f$ transitions, respectively, which partially overlap with the Cu edges at slightly lower energies. Unlike for the Cu edges, the Pr edges display no signs of in-plane versus out-of-plane anisotropy due to the dominant $4f_{z(x^2-y^2)}$ orbital shape being uniformly weighted along all three

axes rather than along just two, as is the case for the Cu $3d_{x^2-y^2}$ orbital.

A simulated absorption spectrum for Pr was computed using Quanty [90] in collaboration with Prof. Yi Lu (Nanjing University). The spectrum was calculated for a Pr^{3+} in the presence of a crystal field using the crystal field splittings found in [91]. As shown in Figure 4.10, the simulated Pr^{3+} spectra is in excellent agreement with the experimentally measured XAS, further confirming that the Pr in $Pr_xY_{1-x}Ba_2Cu_3O_7$ is indeed trivalent. There is considerable structure at the Pr edges, which is especially pronounced for the M_4 edge, due to coupling of the spin and orbital moments between the $3d$ and $4f$ electrons [92].

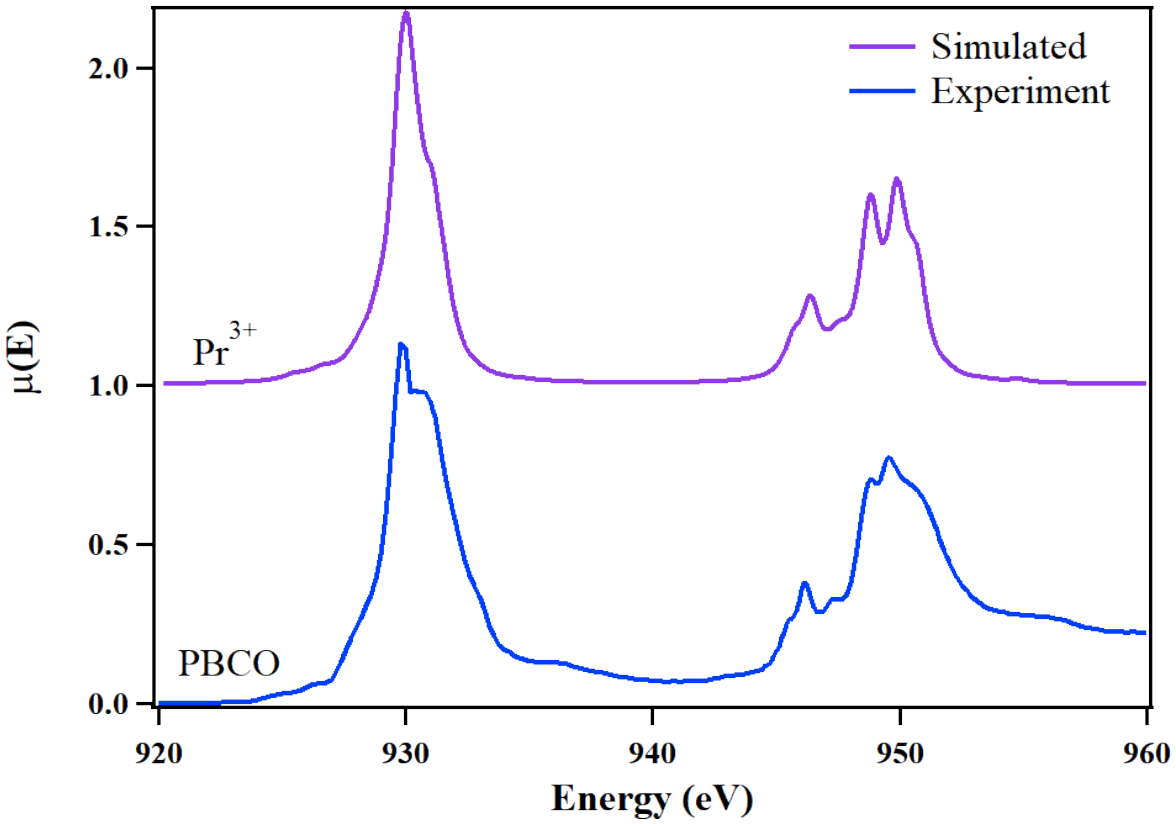

Figure 4.10: A simulated absorption spectrum for an isolated Pr^{3+} ion simulated using Quanty (purple) is in excellent agreement with the experimentally measured XAS for PBCO (blue), confirming that the Pr is trivalent.

RIXS

As discussed in Section 3.1, all decay channels are integrated in the absorption spectrum. To obtain further information about the electronic processes constituting the XAS spectra, RIXS was measured for the same YBCO and PBCO samples as shown in Figure 4.8. The RIXS spectra were collected at the ADRESS X03MA beamline of the Swiss Light Source at the Paul Scherrer Institute (PSI, Switzerland) using the SAXES spectrometer. The spectra were measured at 16 K under ultrahigh vacuum at grazing incidence (15°) with an energy resolution of ∼130 meV, as estimated by the full width at half maximum of the elastic line. Both samples were polished to reduce surface defects. All RIXS measurements were normalized by the incident photon flux.

RIXS maps were measured for both π and σ polarizations over an incident x-ray energy range of 929-934 eV, spanning both the Pr M_5 and Cu L_3 absorption edges at 930.0 eV and 931.2 eV, respectively, as shown in Figure 4.11. The data has been normalized such that the maximum intensity is unity for the RIXS maps only. A more detailed quantification of the spectral features and their corresponding intensities may be seen in Figure 4.12, which displays the RIXS spectra measured at the Pr M_5 (930.0 eV) and Cu L_3 (931.2 eV) energies.

The YBCO spectra measured at the Cu L_3 edge is known to contain an elastic peak (0 eV) (i.e., $3d_{x^2-y^2} \rightarrow 3d_{x^2-y^2}$), a local spin-flip excitation (-0.23 eV), and dd excitations (-1.5 eV) that correspond to transitions between the $3d_{x^2-y^2}$ and $3d_{xy}$ (-1.5 eV), $3d_{yz}$ and $3d_{xz}$ (-1.6 eV), or $3d_{z^2-r^2}$ (-2.0 eV) orbitals [93]. The spin and dd excitations are largely suppressed for incident x-rays in which the electric field oscillates out-of-plane (π polarization) compared to incident x-rays which oscillate in-plane (σ polarization), illustrating the quasi-2D nature of the active $3d_{x^2-y^2}$ orbital. The RIXS spectra for YBCO measured at the Pr M_5 edge are featureless, as can be seen in Figure 4.11, due to both a lack of Pr content and a beam energy which is below the Cu L_3 absorption edge and are not shown in Figure 4.12.

The PBCO spectra measured at the Cu L_3 edge displays the same features as YBCO, which are also suppressed for the π polarization, as well as five additional features between the

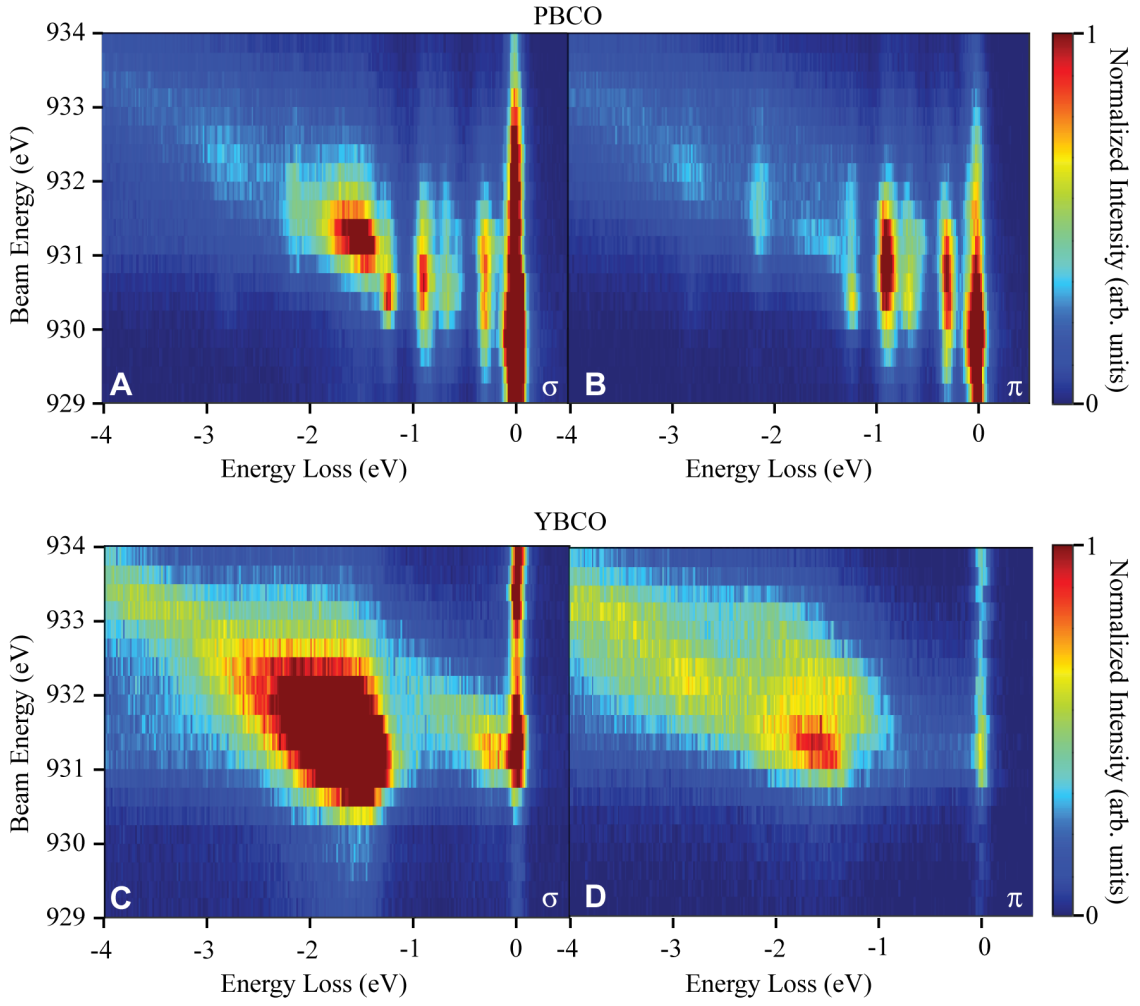

Figure 4.11: Normalized RIXS maps are shown as a function of incident beam energy versus energy loss of the scattered photon for PBCO in **A** σ and **B** π incident x-ray polarizations, as well as for YBCO in **C** σ and **D** π polarizations.

elastic line and *dd* excitations (-0.28 eV, -0.55 eV, -0.67 eV, -0.88 eV, and -1.22 eV) and a feature at the tail of the *dd* excitations (-2.12 eV). The RIXS spectra measured at the Pr M_5 edge displays a similar set of features, but without the features at -0.55 eV and -1.22 eV, as well as the features arising from the Cu 3*d* orbitals.

To discern the nature of these additional features that are present for PBCO, RIXS spectra for Pr were simulated using Quanty [90] in collaboration with Prof. Yi Lu (Nanjing

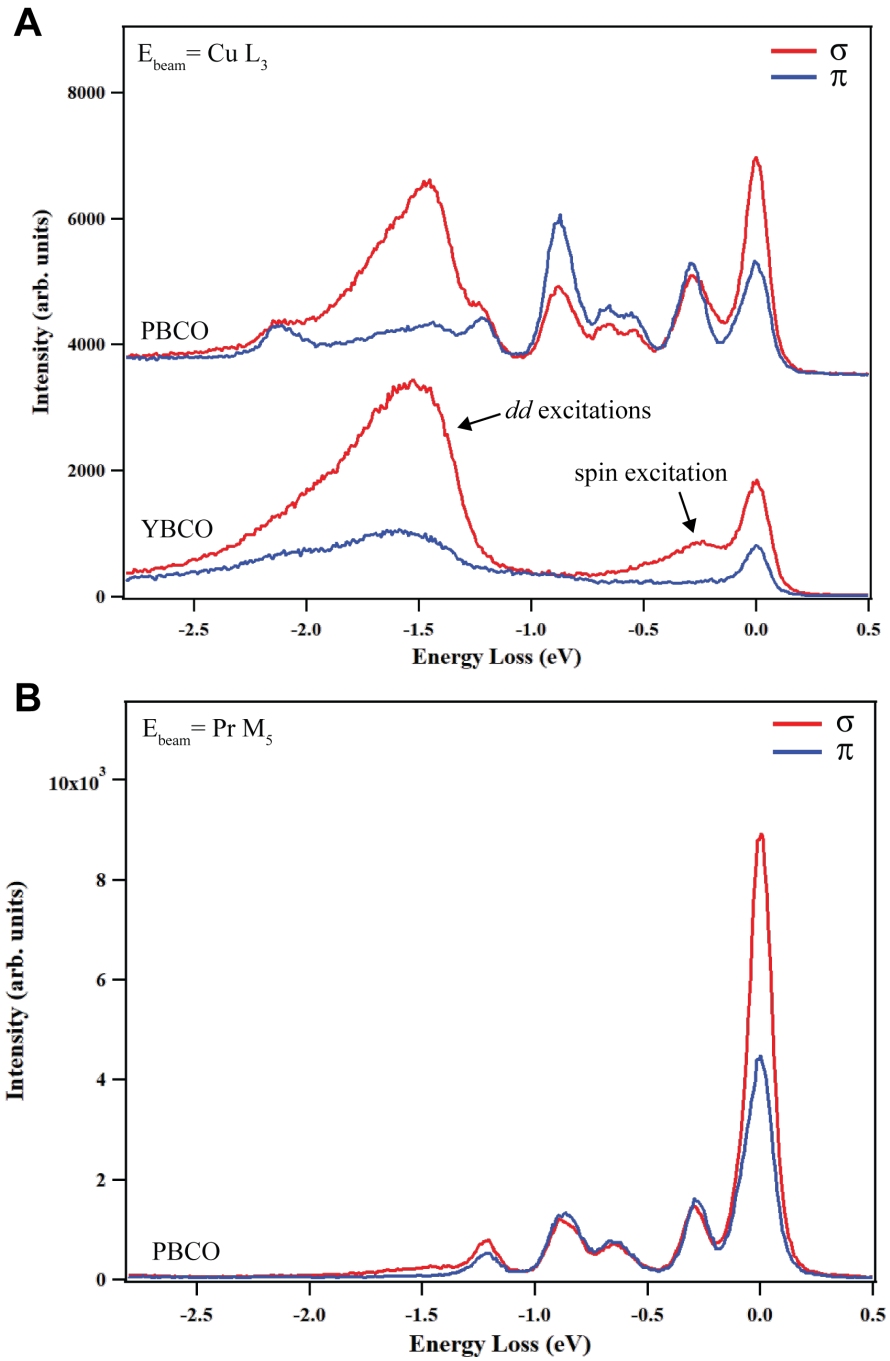

Figure 4.12: The RIXS spectra measured as a function of intensity versus scattered photon energy loss for σ (red) and π incident x-ray polarizations is shown for **A** PBCO and YBCO measured with the beam energy tuned to the Cu L_3 edge (931.2 eV), as well as for **B** PBCO with the the beam energy tuned to the Pr M_5 edge.

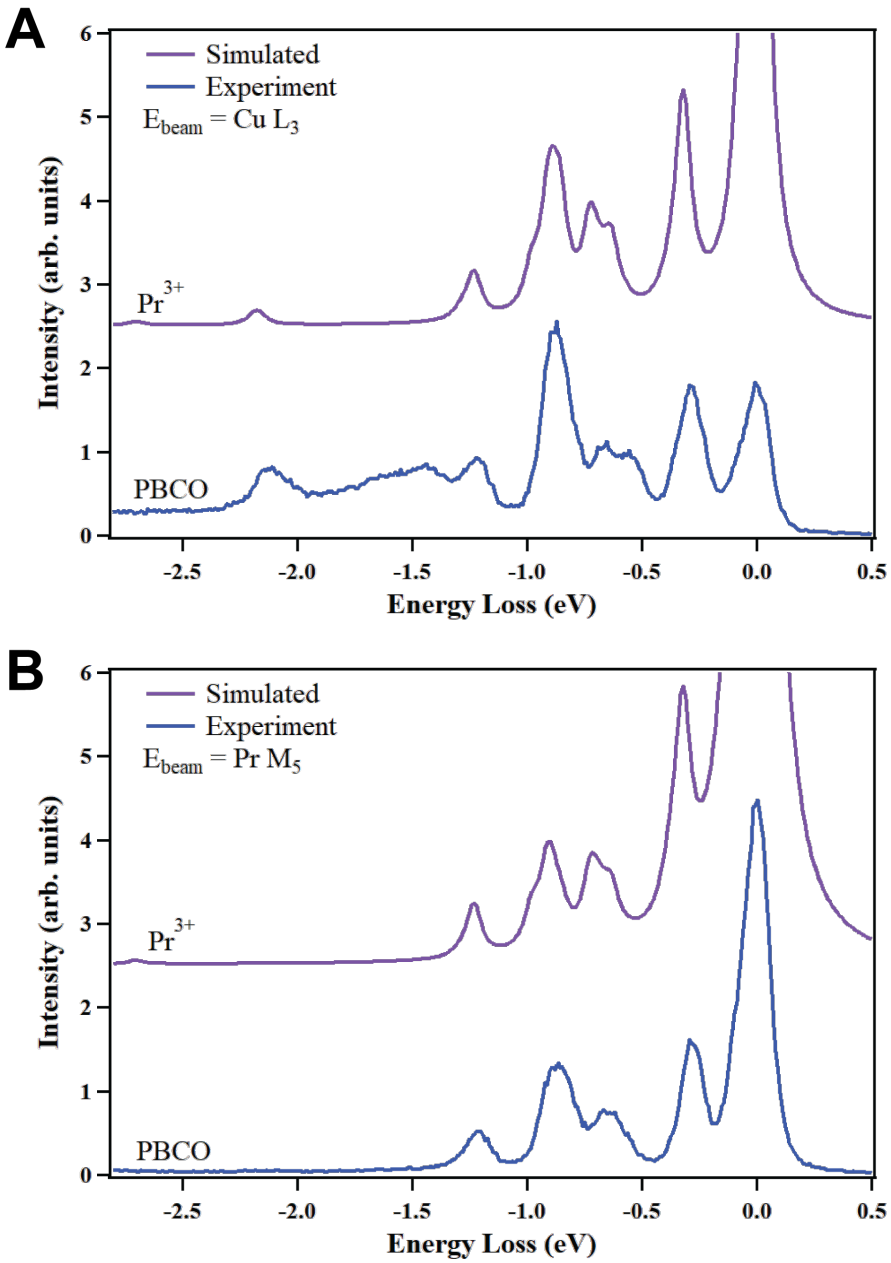

Figure 4.13: The experimentally measured RIXS spectra for PBCO (blue) is compared to simulated spectra for a Pr^{3+} atom in the presence of a crystal field for incident beam energies tuned to the **A** Cu L_3 and **B** Pr M_5 resonances.

University). The RIXS spectra were simulated for a Pr^{3+} atom within the presence of a crystal field, using the crystal field splittings found in [91]. As shown in Figure 4.13, it can be seen that the simulated RIXS spectra are in excellent agreement with the experimentally measured data,

capturing all features present in the measured RIXS spectra at both the Pr M_5 and Cu L_3 incident energies. While there may be discrepancies between the peak intensities in the simulated and measured spectra, especially for the elastic peaks, this effect is likely a result of the experimental geometry. Because only Pr is included in the simulations, it can be concluded that the additional features observed in the PBCO spectra that are absent in the YBCO spectra do not emanate from the interaction between Pr and other atoms in the unit cell and are most likely the result of multiplet effects that are commonly observed in rare-earth spectra originating from the Coulomb interactions between the two valence electrons in Pr^{3+}.

4.2.3 Cu 3*d* Orbital Imaging

The richness of the cuprate phase diagram (Fig 4.1) emanates from the combination of complex interactions between various degrees of freedom within the quasi-2D CuO_2 planes. These interactions are largely influenced by the characteristics of the planar Cu 3*d* orbitals that dominate the density of states near the Fermi surface. The character of these 3*d* orbitals are, for example, responsible for the in-plane versus out-of-plane anisotropy observed in electrical and thermal conductances [57]. To gain insights about the character of the active Cu 3*d* state in PYBCO, inelastic x-ray scattering (IXS) techniques were used to directly discern the shape of the active orbital hole density.

IXS

Non-resonant inelastic x-ray scattering (IXS) has recently emerged as a powerful tool that is capable of imaging the orbital shape of local *d* hole densities in single-crystal transition metal compounds [94–96]. The orbital imaging method involves measuring the intensity of a peak in the IXS spectrum that corresponds to a particular transition between electronic orbitals at different angles. This technique was utilized to determine the shape of the active Cu 3*d* orbital hole within the CuO_2 planes of $Pr_{0.8}Y_{0.2}Ba_2Cu_3O_7$ (Figure 4.14) that is responsible for much of

the underlying physics of the parent compound [57].

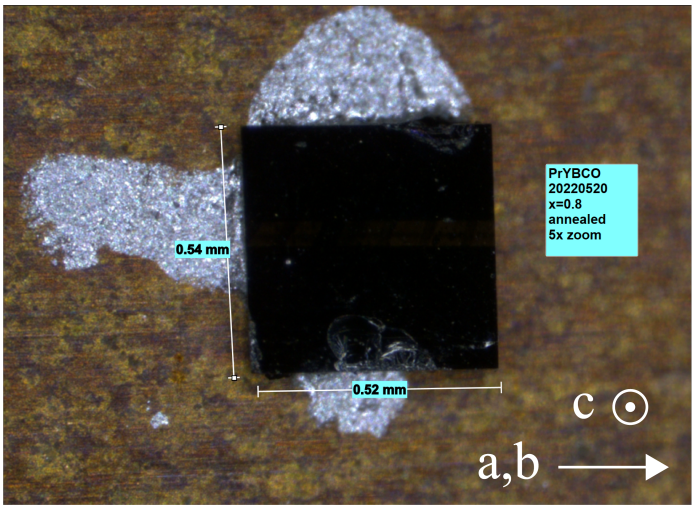

Figure 4.14: The sample of $Pr_{0.8}Y_{0.2}Ba_2Cu_3O_7$ used to image the Cu $3d_{x^2-y^2}$ orbital by IXS measurements is shown.

The Cu $3d$ orbital was directly probed by selecting out photons from the IXS spectra at the Cu M_1 edge, which corresponds to the dipole-forbidden $3s \rightarrow 3d$ transition, as shown in Figure 4.15. Although the Cu M_1 signal partially overlaps with the Pr $N_{4,5}$ edges, there is sufficient separation between these features such that the spectral intensity of the Cu M_1 signal could be easily extracted with simple Gaussian fitting procedures. The shape of the orbital hole was discerned by changing the relative angle between the electric field polarization vector of the incident photon and the $3d$ orbital by virtue of rotating the sample along various high-symmetry directions, namely along the [100]→[010], [001]→[100], and [001]→[110] directions. Because the spherically symmetric $3s$ orbital is isotropic upon any rotation, this ensures that any measured angular dependence of the Cu M_1 intensity is determined exclusively by the $3d$ orbital shape.

The IXS measurements were collected at the P01 High Resolution Dynamics beamline of PETRA-III at the Deutsches Elektronen-Synchrotron (DESY, Germany). The incident x-ray beam energy was tuned using a Si(311) double-reflection crystal monochromator. The scattered photons were analyzed by a 3x4 array of spherically bent Si(660) crystal analyzers fixed to an energy of 9.69 keV. The energy loss spectra were measured by continuously sweeping the monochromator

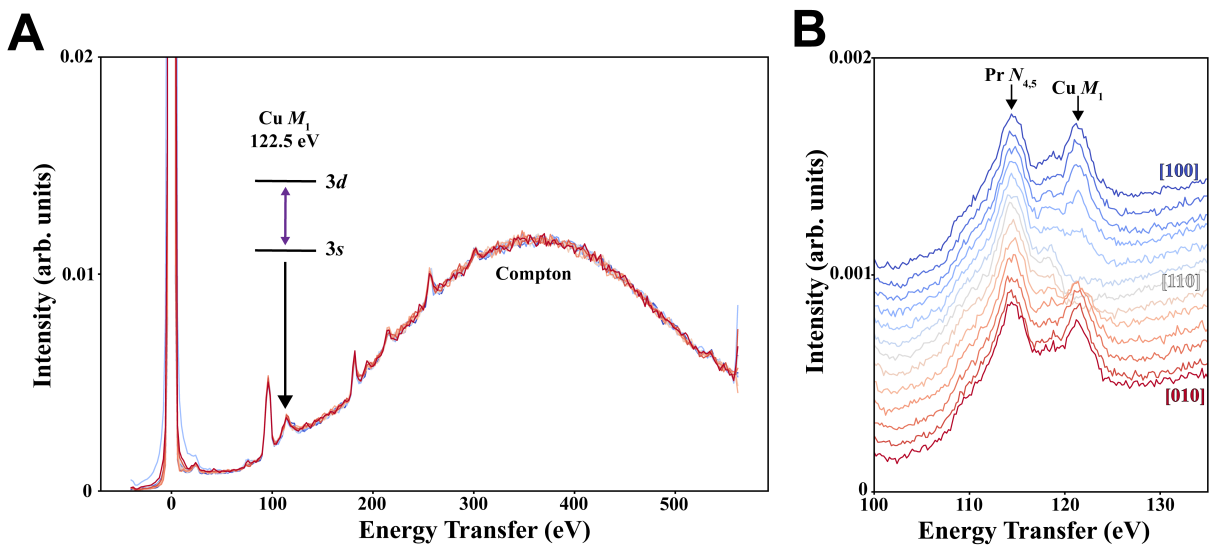

Figure 4.15: **A** The entire IXS spectra measured in PYBCO along the [100]→[010] direction are shown, including the Compton profile. The dipole-forbidden Cu M_1 ($3s \rightarrow 3d$) transition is highlighted at 122.5 eV. **B** The Pr $N_{4,5}$ peaks partially overlap with the Cu M_1 peak, which disappears when **Q** is parallel to the [110]-direction, directly between the lobes of the $3d_{x^2-y2}$ orbitals.

from 9.69 keV (the elastic line) to higher energies, thus scanning the energy transferred in the inelastic scattering process. The experimental resolution, which is estimated by the full width at half maximum of the elastic line, was measured to be ∼1.4 eV. Fixing the scattering angle to $2\theta = 155^\circ$ yields a momentum transfer vector **Q**≈9.6 Å^{-1}. All samples were polished to reduce surface defects and measured under ultrahigh vacuum at a temperature of 20 K. All IXS spectra were normalized by the spectral weight of the Compton background.

The angular dependence of the Cu M_1 peak parameterized along various high-symmetry paths through the Brillouin zone in $Pr_{0.8}Y_{0.2}Ba_2Cu_3O_7$ are shown in Figure 4.16, outlined by the best fit linear combination of one-electron atomic wavefunctions. From these plots, the shape of the planar Cu $3d$ orbital was inferred. Due to the $3d^9$ electronic configuration of the planr Cu^{2+} ions and approximately tetragonal symmetry of the underlying $Pr_{0.8}Y_{0.2}Ba_2Cu_3O_7$ crystal lattice [63, 74, 80], the $3d_{xy}$, $3d_{xz}$, and $3d_{yz}$ orbitals are fully occupied in the ground state with the only hole occupying a mixed superposition state composed of the remaining $3d_{x^2-y^2}$ and

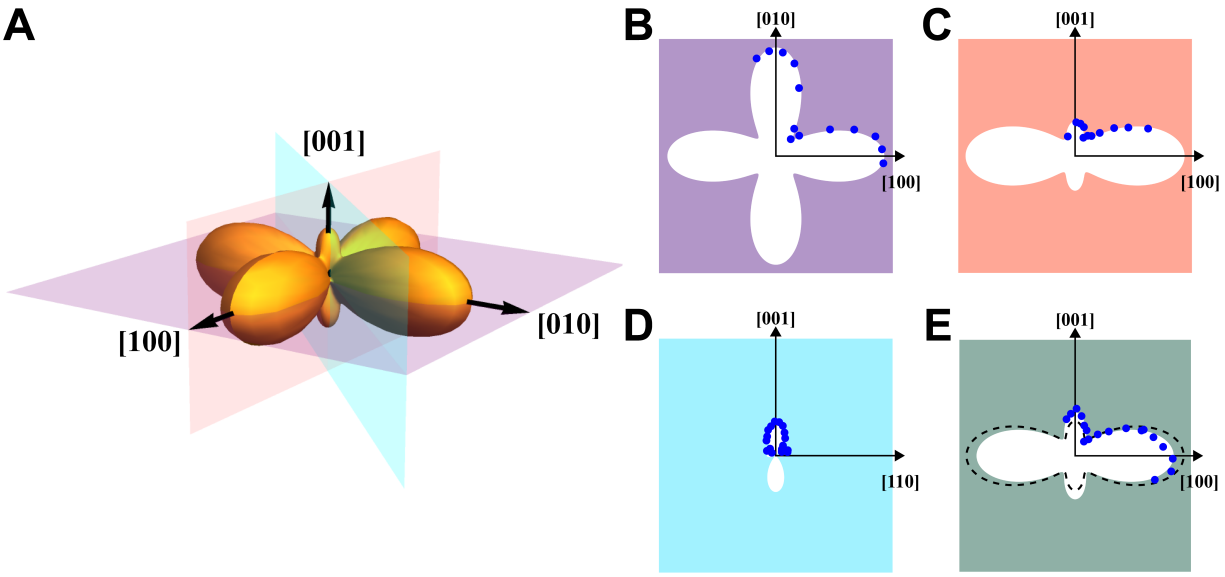

Figure 4.16: **A** The Cu 3*d* hole density in PYBCO was reconstructed by integrating the Cu M_1 peak intensity as **Q** sweeps through: **B** the [010]-[100] plane, **C** the [001]-[100] plane, and **D** the [001]-[110] plane. **E** The measured projection of the 3*d* orbital shape of YBCO in the [001]-[100] plane compared to for PYBCO (black dashes) reveals that the relative proportion of holes increasingly favors the $3d_{x^2-y^2}$ state over the $3d_{z^2}$ state as the Pr content increases.

$3d_{z^2-r^2}$. Because the spectral intensity is integrated over contributions from all final states in the IXS process, only these active $3d_{x^2-y^2}$ and $3d_{z^2-r^2}$ orbitals containing the initial-state holes are expected to contribute to the imaging [94].

Scanning along the [100]→[010] direction reveals the familiar shape of the $3d_{x^2-y^2}$ orbital, with its characteristic lobes lying parallel to the *a* and *b* crystallographic axes, albeit with a small constant contribution from the rotationally invariant equatorial lobe of the $3d_{z^2-r^2}$ orbital. Although this sample is fully oxygenated, no significant difference is expected for these lobes due to the loss of orthorhombicity in $Pr_xY_{1-x}Ba_2Cu_3O_7$ for high Pr concentrations, as discussed in section 4.1.1.

The sample was rotated and scanned along the [001]→[100] direction to obtain the out-of-plane projection of the active Cu 3*d* orbital. The resulting orbital shape clearly exhibits components from both the $3d_{x^2-y^2}$ and $3d_{z^2-r^2}$, with lobes lying parallel to the *a* and *c* crystallographic axes, respectively. From the fitting analysis, the observed mixed 3*d* orbital is weighted

88.6% by the $3d_{x^2-y^2}$ orbital and 11.4% by the $3d_{z^2-r^2}$. As expected from the quasi-2D nature of the CuO_2 planes, the in-plane orbital is weighted significantly greater than the out-of-plane orbital.

To eliminate any contribution from the $3d_{x^2-y^2}$ orbital, the sample was rotated azimuthally by 45°an scanned along the [001]→[110] direction which lies parallel to the nodal plane of the $3d_{x^2-y^2}$ orbital. As expected, only the $3d_{z^2-r^2}$ orbital is observed.

Measurement along the [001]→[100] direction was repeated for a sample of $YBa_2Cu_3O_7$, from which the $3d_{x^2-y^2}$ and $3d_{z^2-r^2}$ orbital contributions were extracted. The resulting mixed-state orbital sppears similar to $Pr_{0.8}Y_{0.2}Ba_2Cu_3O_7$, but with a proportionally smaller contribution from the $3d_{x^2-y^2}$ orbital and larger contribution from the $3d_{z^2-r^2}$ orbital, weighted 84.3% and 15.7%, respectively. This indicates that the relative proportion of holes increasingly favors the $3d_{x^2-y^2}$ state over the $3d_{z^2-r^2}$ state as the Pr content increases, even though the concentration of itinerant hole carriers has been shown to decrease overall [97, 98]. This result is consistent with the observed increase in anisotropy of resistivity when measured along the *c*-axis versus in the basal *ab*-plane, $\frac{\rho_c}{\rho_{ab}}$, with increasing Pr content [99].

While there are two symmetrically inequivalent Cu ions in the $Pr_xY_{1-x}Ba_2Cu_3O_7$ unit cell (i.e., those located in the CuO_2 planes and those in the CuO chains), only the planar Cu orbitals in the CuO_2 planes are captured by the imaging process. Due to the high Pr content of $Pr_{0.8}Y_{0.2}Ba_2Cu_3O_7$, the Cu signal from the CuO chains is largely suppressed, as can be seen in the absorption spectra shown in Figure 4.9. Furthermore, even in the case that a Cu signal from the CuO chains is present, such as in the absorption spectra for YBCO shown in Figure 4.9, the spectral intensity is considerably weaker than for the Cu signal emanating from the CuO_2 planes. The quadrupolar M_1 signal has sufficiently less scattering strength than the dipole-allowed $L_{3,2}$ edges, implying that any signal originating from the CuO chains will be negligibly small, especially when the x-ray polarization is perpendicular to the CuO chain direction (π polarization). When the x-ray polarization is kept in-plane (σ polarization), where the signal between Cu ions in

the chains and planes is most comparable, no satellite peaks analogous to those observed by XAS are detected, either by inspection of by peak fitting algorithms. Because the full width at half maximum of the measured M_1 signal is $\lesssim$4.2 eV and the separation between Cu chain and plane signals is $\sim$3 eV, an M_1 satellite peak of non-negligible intensity should be located outside of the full width of the primary peak and, therefore, be resolvable, at least computationally. Additionally, subtraction of the measured Cu M_1 spectra measured along the two in-plane directions, [100] and [010], does not display any features at energies where a satellite peak would be expected, as shown in Figure 4.17. This implies that the imaged Cu 3*d* orbital has four-fold symmetry rather than two-fold symmetry, as would be the case if considerable signal from the CuO chains were present, confirming that only the Cu residing in the CuO_2 planes contribute significantly to the imaged orbital.

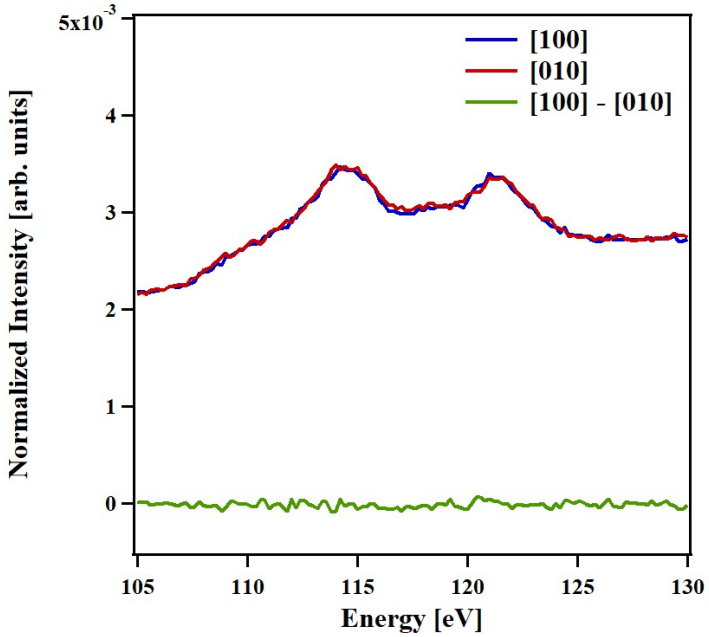

Figure 4.17: The Cu M_1 signal measured along the [100] (blue) and [010] (red) are shown. Subtraction of these two spectra (green) does not show any features near the Cu M_1 energy where a contribution from the Cu ions in the CuO chains would be expected.

4.2.4 3D Charge Ordering

One of the most intriguing states found within the cuprate phase diagram (Figure 4.1) is the charge order (CO) phase which has been observed in nearly all cuprate systems at moderate doping levels [50]. CO is not unique to the cuprates and may also be found in other material families, such as in manganites [100] and nickelates [101]. CO consists of a periodic modulation of the electronic charge density which is typically arranged in either a stripe or checkerboard pattern [102], as shown in Figure 4.18, with a periodicity that is not necessarily commensurate with that of the underlying lattice [103].

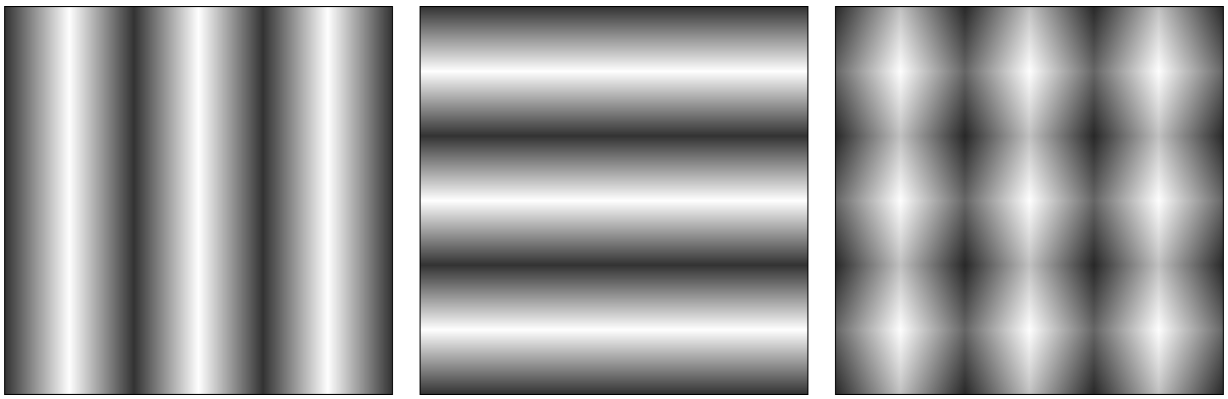

Figure 4.18: Charge order (CO) consists of the periodic modulation of the electronic charge density which is typically arranged in either stripe (left, middle) or checkerboard (right) patterns.

The simplest example of CO arises as a consequence of the Peierls' theorem [104], which states that a one-dimensional (1D) chain of equally spaced ions with one electron per ion is unstable and will inevitably undergo a Peierls transition, as shown in Figure 4.19 [105]. For an evenly spaced chain of ions with one electron per ion, the band will be half-filled, resulting in $\boldsymbol{k}_F = \pm\frac{2\pi}{a}$, where $\boldsymbol{k}_F$ is the Fermi wavevector, which corresponds to the highest filled state located at the Fermi energy, E_F, and a is the 1D lattice spacing. Undergoing the Peierls transition, the ionic lattice distorts such that the periodicity doubles from $a \rightarrow 2a$, producing a periodic fluctuation in the charge density, $\rho(x)$. By doubling the lattice periodicity, the Brillouin zone boundary is reduced from $\pm\frac{\pi}{a} \rightarrow \pm\frac{\pi}{2a}$, resulting in the opening of an energy gap through the

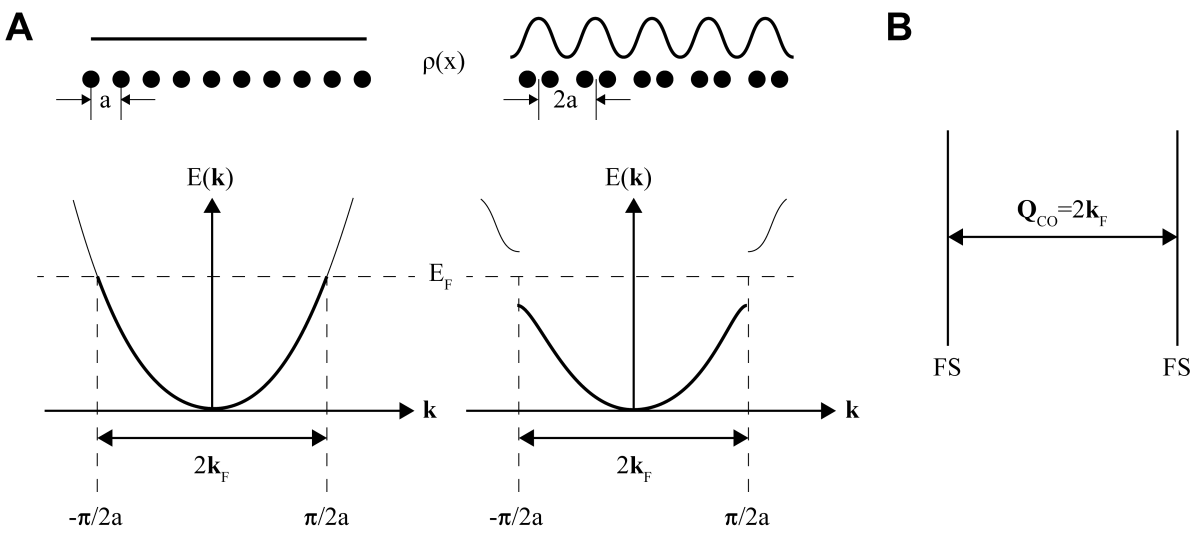

Figure 4.19: **A** According to the Peierl's theorem, a 1D chain of ions with one electron per ion will undergo a Peierls transition in which a lattice distortion doubles the periodicity from $a \rightarrow 2a$, which induces a periodic modulation in the charge density, $\rho(x)$, and reduces the Brillouin zone boundary from $\pm\frac{\pi}{a} \rightarrow \pm\frac{\pi}{2a}$, resulting in the lowering of the energy of the electronic states near the Fermi energy, E_F. **B** The Fermi surface (FS) is nested by the CO wavevector, $\mathbf{Q}_{CO} = 2\boldsymbol{k}_F$. Adapted from [105].

formation of standing waves. Thus, the energy of the states near E_F are lowered and this transition becomes energetically favorable when the energy reduction of these electronic states outweighs the elastic energy cost of distorting the lattice. The CO wavevector, $\mathbf{Q}_{CO} = 2\boldsymbol{k}_F$, connects two large, parallel regions of the Fermi surface (FS), known as FS nesting. While the Peierls transition is said to be driven by FS nesting, this is not necessarily the case for all CO formation [106].

The most enigmatic property of CO in the cuprates is that it competes directly with high-T_c SC [50, 107]. Evidence of these phases being intertwined was first observed through a deviation of the empirical Obertelli-Cooper-Tallon law [108], which relates T_c to hole doping, where the observed T_c was lower than expected for $\sim \frac{1}{8}$ hole doping, known as the "plateau anomaly". An example of this plateau may be seen in the YBCO phase diagram (Figure 4.5) for $\delta \approx 0.7$. Investigation of this anomalous suppression of T_c is what led to the initial discovery of cuprate CO [109]. The competition between CO and SC is further illustrated by measuring the temperature dependence of the CO signal. As the temperature decreases for $T > T_c$, the

scattering amplitude of CO signal monotonically increases. However, once the temperature is decreased such that $T < T_c$, the CO signal begins to decrease, producing a cusp-like maximum in the CO temperature dependence at $T = T_c$ [110]. Moreover, the lost CO scattering amplitude below T_c may be restored by suppressing SC with an applied magnetic field [111]. This complex relationship between CO and SC is yet to be fully understood and remains an active focus of research that may prove crucial to comprehending the underlying mechanisms behind high-T_c SC.

Cuprate CO generally manifests with a quasi-2D structure [107] that is confined within the basal plane, with the ordering vector parallel to the Cu-O-Cu bond direction [50]. This is evidenced by the observation of CO peaks centered at half-integer L values in reciprocal space that are overwhelmingly broad along the L direction [112], resulting from the truncation of the charge density by the inert buffer layers which surround the CuO_2 planes [113]. However, it is has recently been discovered that a three-dimensional (3D) CO can be induced in YBCO as a result of various external perturbations. So far, it has been shown that the application of high magnetic fields [114], uniaxial strain [115], and epitaxial strain [112] have all stabilized a 3D CO. The 3D character is indicated by the scattering features located at integer L values in reciprocal space with relatively sharp peaks along the L direction, compared to the broad diffraction rods observed for 2D CO peaks. It is not yet known if the 3D CO is universal to all cuprate families as it has only been observed in YBCO to date. This may either be a result of 3D CO being intrinsically unique to the YBCO system, or it may just be a consequence of the CO state having a high propensity for sensitivity to disorder [50] and has only yet been observed in YBCO because it is the least disordered cuprate when hole-doped by virtue of its ordered CuO chain formation.

A primary result of this dissertation is the discovery that 3D CO may additionally be stabilized in the YBCO system by Pr-substitution. Unlike applied magnetic fields, uniaxial strain, or epitaxial strain, the Pr-substitution is not implemented externally but is instead achieved internally at a chemical level during the synthesis stage. This offers an inherent advantage to studying the 3D CO phenomenon with x-rays as applying either magnetic fields or uniaxial strain

can be experimentally prohibitive and utilizing epitaxial strain is restricted to thin films and the ability to tune the strain parameter is limited by the choice of compatible substrates. As will be discussed in detail, the 3D CO induced by Pr-substitution has some interesting properties compared to those induced by these other mechanisms.

The 3D CO was first observed in a sample of $Pr_{0.3}Y_{0.7}Ba_2Cu_3O_7$, shown in Figure 4.20. The SC transition temperature for this sample was measured to be $T_c = 55$ K, which is approximately the same T_c for which the Obertelli-Cooper-Law anomaly is observed in YBCO (Figure 4.5) and the CO phase is maximal [110]. The lattice parameters were measured to be a=3.8675 Å, b=3.8727 Å, and c=11.6661 Å, which yields a very small orthorhombic distortion of $\sim$0.00067, which is nearly tetragonal and comparable to that observed by [80] for this Pr concentration (x=0.3). Although this sample has not been detwinned, it was measured by x-ray diffraction at beamline ID28 of the European Synchrotron Radiation Facility (ESRF, France) where no satellite peaks were observed down to a resolution of 0.001 Å. Additionally, the 3D CO is only observable along the b direction, suggesting that the sample is not twinned.

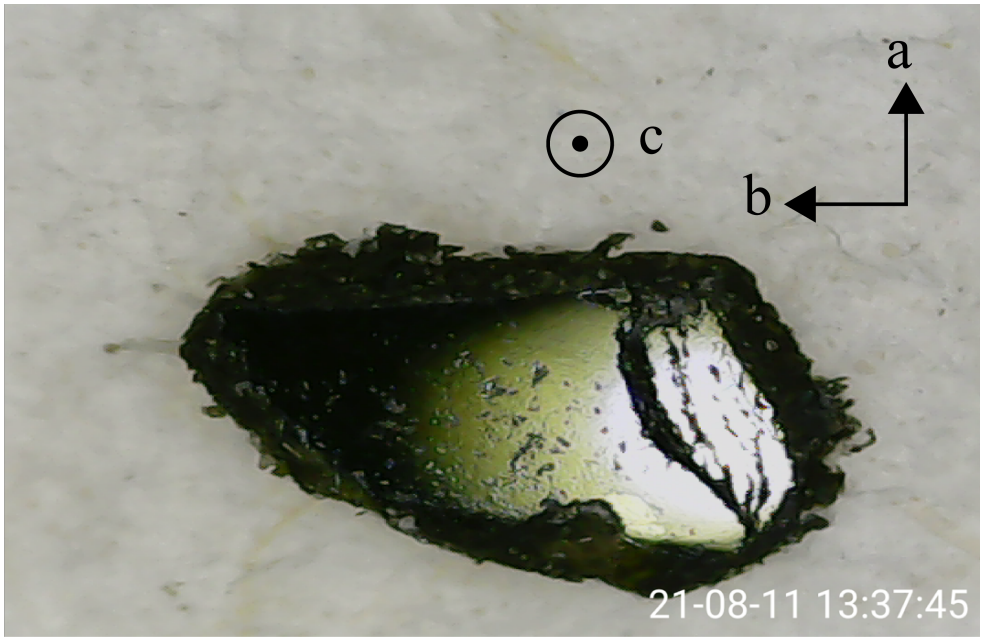

Figure 4.20: The sample of $Pr_{0.3}Y_{0.7}Ba_2Cu_3O_7$ in which 3D CO was first observed is shown.

REXS

The XAS and REXS data were collected under ultrahigh vacuum at beamline 13-3 of the Stanford Synchrotron Radiation Lightsource (SSRL) at the Stanford Linear Accelerator Center (SLAC, USA) using a four-circle goniometer. The sample temperature was controlled using an open-circle helium cryostat and the temperature was fixed at $T_c = 55$ K for all scans, except when measuring the temperature dependence. The incident x-ray polarization was fixed to σ polarization. Scattered photons were measured using a 256×1024 pixel CCD detector with a pixel size of 26 μm×26 μm. Dark images and scattering signal measured outside of the region-of-interest were used to subtract any background fluorescence contributions, which were generally small compared to the 3D CO scattering signal, except when at high temperature or off resonance. The XAS data was collected in fluorescence mode using the CCD as a fluorescence detector and was normalized using Athena [116]. The energy resolution of the incident x-rays was ∼0.1 eV near the Pr M_5 and Cu L_3 edges. The (0 K L) scattering plane was determined by aligning to the (002), (011), and (0$\bar{1}$1) reflections with an incident x-ray energy of 1746 eV. The reciprocal space structure of the 3D CO was determined by compiling many rocking curve scans. The trajectory of a single rocking curve may be seen in Figure 4.21. The structure along H was determined by mapping each pixel of the CCD detector to an HKL coordinate, allowing the collection of volumetric data as the face of the detector sweeps through the KL-plane.

The 3D CO was observed at the scattering vector $\mathbf{Q}_{CO}$ =(0 -0.335 1) reciprocal lattice unites (r.l.u.). A schematic of the corresponding FS nesting by $\mathbf{Q}_{CO}$ is shown in Figure 4.22. The L and K coordinates of $\mathbf{Q}_{CO}$ correspond to a periodicity of one unit cell along the c direction (as is the case for all observations of 3D CO [112, 115, 117]) and a nearly commensurate periodicity of three unit cells along the b direction, respectively. No 3D CO was observed along the H direction, making the 3D CO stabilized by Pr-substitution uniaxial, as has been similarly reported for 3D CO stabilized by magnetic fields [117].

The reciprocal space structure of the 3D CO in PYBCO appears to have a rod-like shape

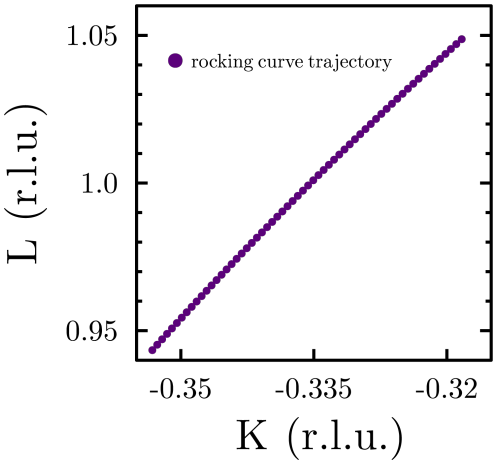

Figure 4.21: The rocking curve trajectory through the center of the 3D CO in the *KL*-plane is shown.

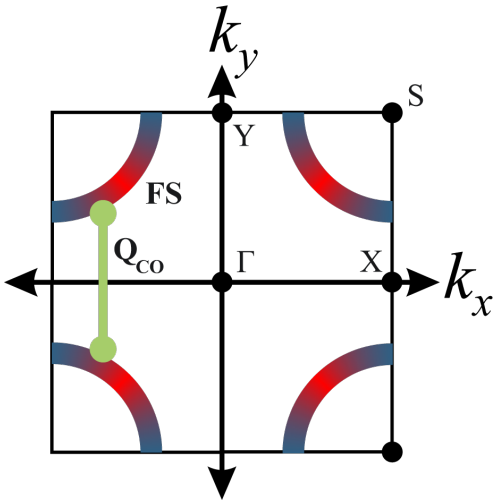

Figure 4.22: An illustration of Fermi surface (FS) nesting by $\mathbf{Q}_{CO}$.

that is very broad along the modulation vector (K) direction but narrow along both other (H, L) directions. Figure 4.23 illustrates the shape of the 3D CO projected onto the KL, HL, and HK planes, in addition to displaying the peak profile through the center of the 3D CO along the L, H, and K directions. All data shown was measured at $T_c = 55$ K with the x-ray beam tuned to 932.4 eV, near the energy where the 3D CO scattering is most intense.

This structure is unique compared to the other observations of 3D CO for a couple of reasons. The 3D CO observed in PYBCO has a significantly narrower line width measured

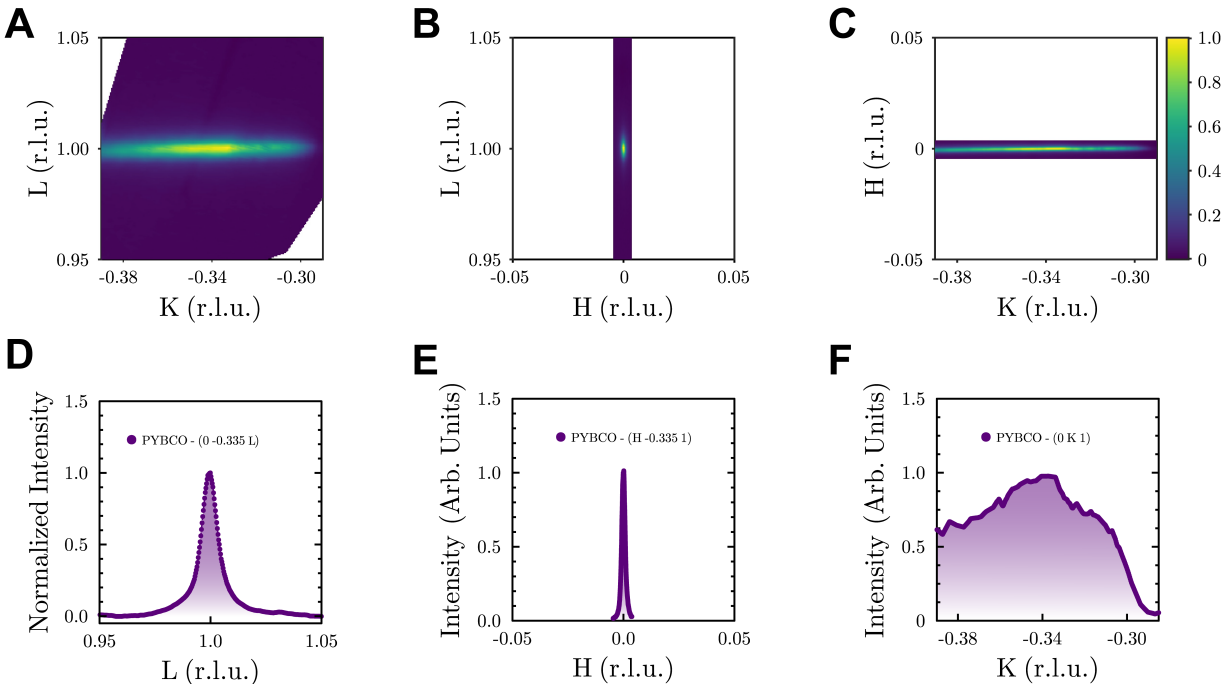

Figure 4.23: Reciprocal space maps of the **A** *KL* plane, **B** *HL* plane, and **C** *HK* plane collected at $T_c = 55$ K and 932.4 eV display a diffraction peak centered at $\mathbf{Q}_{CO}$=(0 -0.335 1) reciprocal lattice unites (r.l.u.) resulting from the 3D CO. Cuts measured along the **D** *L*, **E** *H*, and **F** *K* axes through $\mathbf{Q}_{CO}$ demonstrate that the 3D CO is narrow along the *L* and *H* axes but broad along the *K* axis.

along the *L* direction. This is a significant finding because the peak width can be related to the correlation length, ξ, which quantifies the range in real space over which the CO is ordered, through the formula [110, 118]

$$\xi_{a_i} = \frac{a_i}{\pi} \frac{1}{\text{FWHM}}$$

where a_i is the lattice constant corresponding to the direction along which the correlation length is being measured and FWHM is the full width at half maximum of the measured peak. As a starting reference, the highest reported out-of-plane correlation length for 2D CO in YBCO is only $\xi_c = 10$ Å [50]. The out-of-plane correlation length for the 3D CO in PYBCO has thus been calculated to be $\xi_c = 364$ Å. This is considerably longer than the highest reported correlation lengths for 3D CO when induced by magnetic field ($\xi_c = 55$ Å) [117], epitaxial strain ($\xi_c = 61$

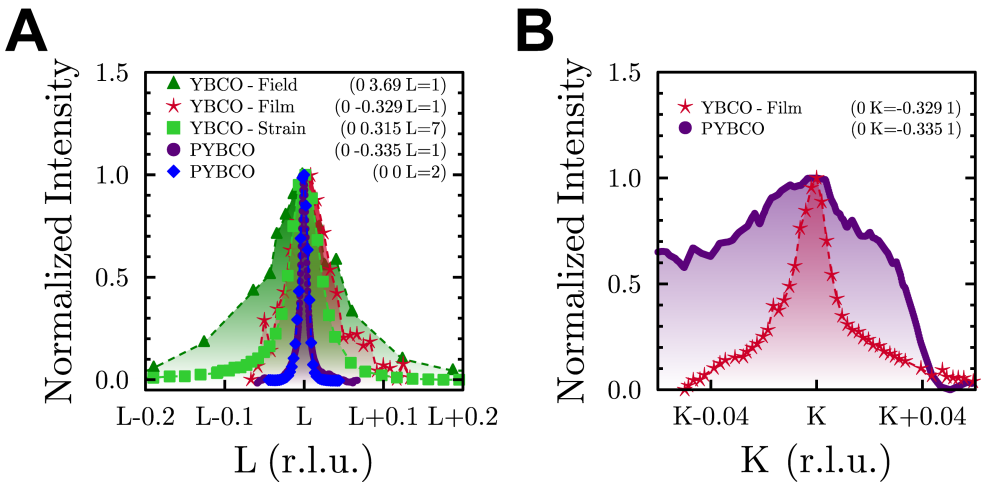

Figure 4.24: **A** A comparison of 3D CO peak widths stabilized by magnetic field [114] (dark green triangles), epitaxial strain [112] (red stars), uniaxial strain [115] (lime green squares), and Pr-substitution (present work) along the out-of-plane (L) direction. The structural (002) reflection in PYBCO (blue diamonds) is also shown. **B** A comparison of the 3D CO peaks stabilized by epitaxial strain [112] and Pr-substitution along the in-plane (K) direction parallel to $\mathbf{Q}_{CO}$.

Å) [112], or uniaxial strain ($\xi_c = 94$ Å) [115], indicating that the 3D CO is significantly more correlated along the c-axis when stabilized by Pr-substitution than by any other method. The value of ξ_c is similar to the penetration depth at this energy ($\sim$930 eV) and angle of incidence ($\sim 10^\circ$), implying that the observed correlation length may be limited by the finite penetration depth. However, the line width of the 3D CO in PYBCO along the L direction is comparable to (002) structural Bragg reflection, which was measured at a higher energy ($\sim$1750 eV) and angle of incidence ($\sim 38^\circ$), resulting in a significantly longer penetration depth. This suggests that the observed 3D CO is instead bounded by the coherence of the crystal lattice. The peak profile of the 3D CO measured along the L direction for PYBCO is compared to the other stabilization methods, as well as to the PYBCO (002) reflection, in panel A of Figure 4.24.

Interestingly, the acute narrowness of the 3D CO along the out-of-plane direction is compensated by an extremely broad peak along the in-plane direction parallel to the modulation vector direction, K. The correlation length along this direction was calculated to be $\xi_b = 70$ Å. While this is significantly broader than the other observations of 3D CO, as shown in a comparison

with the 3D CO stabilized by epitaxial strain in panel B of Figure 4.24, it is consistent with the broad peaks observed in many cuprates [111, 119–121] that has been associated with a fluctuating component in YBCO [122], implying that the static contribution may be narrower than observed. For example, the highest reported in-plane correlation length for YBCO is $\xi_b = 95$ Å [50].

Strikingly, the PYBCO 3D CO peak is actually narrowest along the in-plane direction that is perpendicular to the modulation vector, H, yielding a correlation length that is nearly double that of the c-axis at $\xi_a = 688$ Å. Unfortunately, the other reports of 3D CO do not appear to have measured the 3D CO structure along this direction, presumably due to using a different detector type, so no direct comparison can be made. The 3D CO correlation lengths are summarized in Table 4.1.

Table 4.1: The correlation lengths of the 3D CO along the a, b, and c axes.

Axis	Correlation length (ξ)
a	$\xi_a = 688$ Å
b	$\xi_b = 70$ Å
c	$\xi_c = 364$ Å

From the correlation lengths along the a, b, and c axes, a 3D CO domain size may be estimated. The result is a planar domain which spans $\sim$18 unit cells along the direction of modulation (b-axis) and $\sim$178 unit cells along the a-axis, with an out-of-plane correlation that spans $\sim$31 unit cells. The in-plane asymmetry of the domains, coupled with being uniaxial, suggests the 3D CO is nematic, similar to the magnetic-field-induced 3D CO observed in YBCO with a comparably weak orthorhombicity [117]. A schematic of the real space 3D CO structure is shown in Figure 4.25.

One of the most distinct features which differentiates the 3D CO in PYBCO from other stabilization methods is the absence of any 2D CO. Both the H and K axes were searched

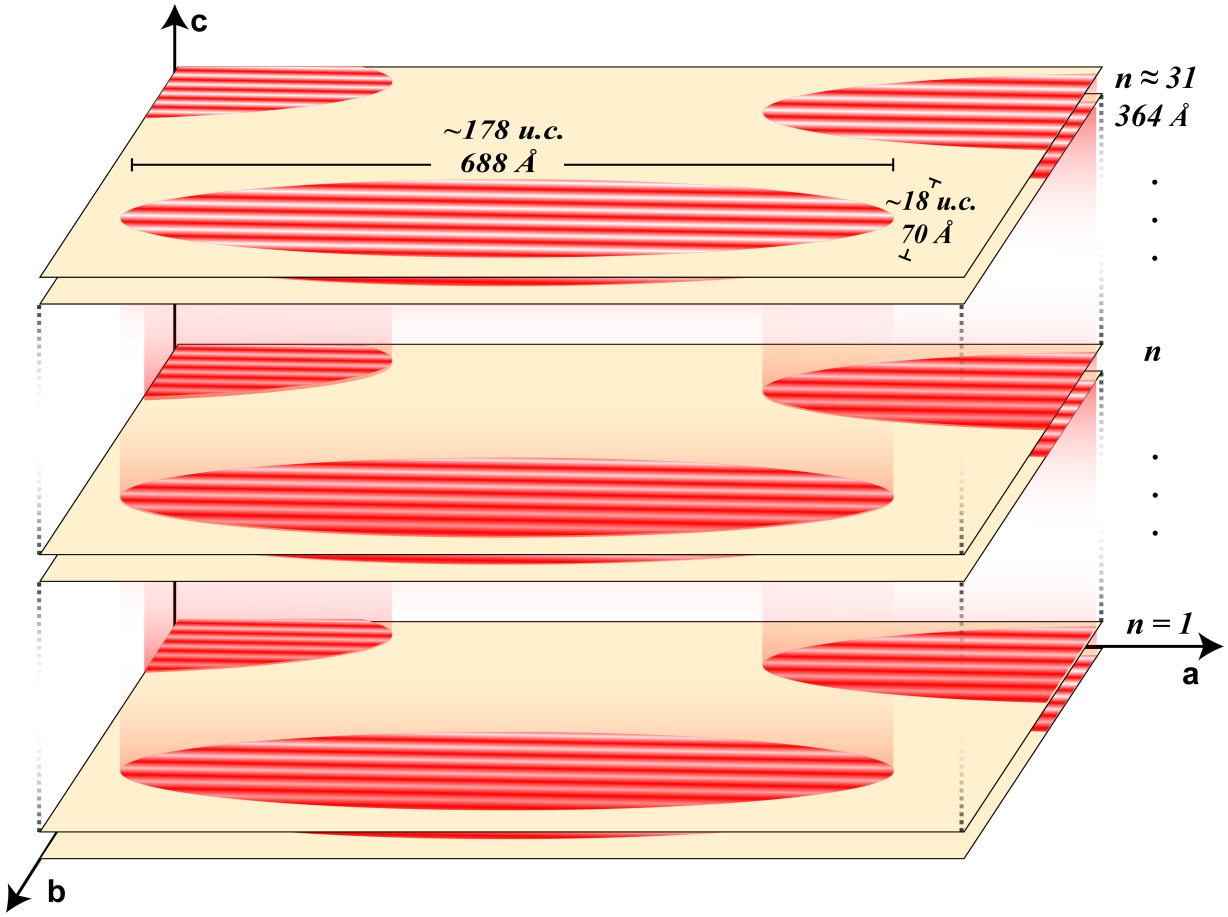

Figure 4.25: A schematic depiction of the 3D CO domains defined by the in-plane and out-of-plane correlation lengths in PYBCO. The planar domains span approximately 18×178 unit cells (u.c.) with a 3D coherence of ∼31 sets of CuO_2 planes.

extensively in the region where 2D CO is expected ($L \approx 1.5$) but no scattering intensity was observed. This is illustrated in Figure 4.26 which displays the data from two rocking curves scanned over different L values. Although $L = 1.5$ lies outside of the Ewald sphere at the Pr M_5 and Cu L_3 energies, any existing 2D CO should still be detected due to the broadness of 2D CO peaks along L [112, 115]. While all other reports of 3D CO also observe the coexistence of 2D CO [112, 115, 117], it is believed that the 2D and 3D versions of CO are separate entities due to drastically differences in their qualitative behaviors, such as their dimensionality, directionality, and dependencies on temperature and applied magnetic fields [117]. The apparent lack of any coexisting 2D CO in PYBCO seems to support this hypothesis. It is possible that the lack of 2D

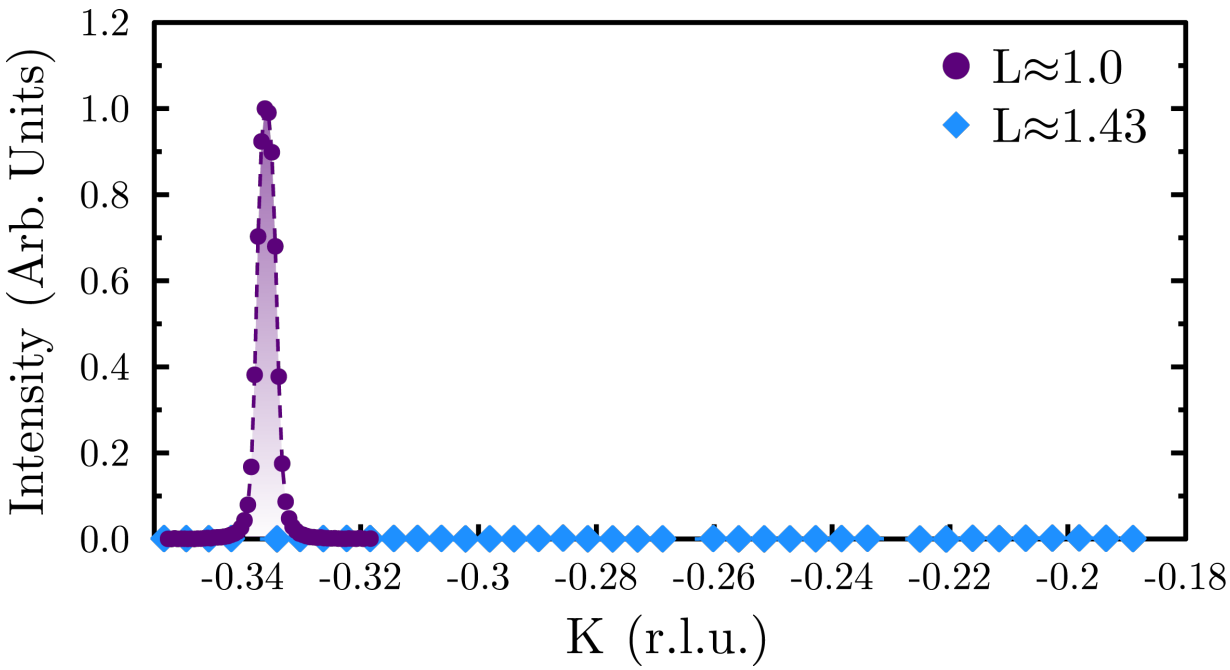

Figure 4.26: Two rocking curve scans measured in the vicinity of L=1.0 (purple circles), where the 3D CO is observed, and L=1.43 (blue diamonds), where any existent 2D CO would be observed.

CO in $Pr_{0.3}Y_{0.7}Ba_2Cu_3O_7$ is a result of being full oxygenated as the 2D CO state has been shown to be fully suppressed in $YBa_2Cu_3O_{6+\delta}$ for $\delta = 0.99$ [110]. It would be interesting to measure a sample of $Pr_xY_{1-x}Ba_2Cu_3O_{6+\delta}$ where the Pr content is fixed at $x = 0.3$ but with the O content reduced to δ =0.6-0.75, where the 2D CO phase is maximal. If no 2D CO is observed, keeping the O content fixed at δ =0.6-0.75 and varying $0 < x < 0.3$ could determine the minimum Pr concentration required to destroy the 2D CO state.

The energy dependence of the 3D CO was measured by tuning the incident beam energy from 925-940 eV while keeping the temperature fixed. Panel A of Figure 4.27 shows the energy dependence of the 3D CO overlaid with the absorption spectrum. The XAS displays two overlapping peaks corresponding to the Pr M_5 ($3d_{\frac{5}{2}} \rightarrow 4f$) and Cu L_3 ($2p_{\frac{3}{2}} \rightarrow 3d$) transitions at 930.9 eV and 932.6 eV, respectively. The energy dependence of the 3D CO also displays two features corresponding to the Pr and Cu resonances at 930.3 eV and 932.8 eV, respectively. Interestingly, even though the fluorescence signal in the XAS is slightly weaker at the Pr edge

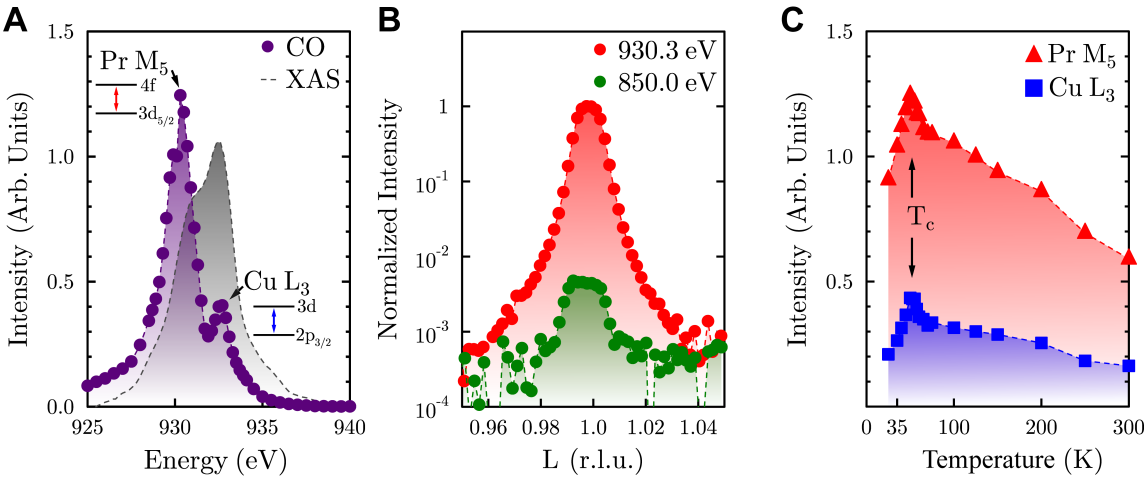

Figure 4.27: **A** The x-ray absorption spectrum (XAS) of PYBCO (gray) displays the Cu L_3 absorption edge with a shoulder at lower energy corresponding to the Pr M_5 absorption edge. The dipole-allowed transitions corresponding to each absorption edge are labeled as inserts. The energy dependence of the 3D CO peak (purple) measured at $T_c = 50$ K displays two features corresponding to the Cu L_3 and Pr M_5 resonant energies. **B** A semi-log plot of the measured 3D CO scattering intensity at the Pr M_5 resonance (red) and far below the resonance (green). **C** The temperature dependence of the 3D CO measured at the Pr M_5 (red) and Cu L_3 resonance energies is shown. A cusp-like maximum is observed at the superconducting critical (SC) temperature, $T_c = 50$ K, with a reduction of intensity within the SC phase.

than at the Cu edge, the 3D CO scattering intensity is significantly higher at the Pr resonance than at the Cu resonance, suggesting strong involvement by the Pr ion in the 3D CO formation.

Unlike other reports of 3D CO, the 3D CO in PYBCO is observable without resonant enhancement. The semi-log plot in panel B of Figure 4.27 compares rocking curve scans measured through the 3D CO at 930.3 eV, where the 3D CO resonates most strongly, and at 850.0 eV, far below the Pr M_5 and Cu L_3 absorption edges. Although the scattering intensity off-resonance is multiple orders of magnitude weaker than at the Pr resonance, it is still distinctly observable, alluding to the robustness of the 3D CO phase when stabilized by Pr-substitution. This is further corroborated by the temperature dependence of the 3D CO, which is displayed in panel C of Figure 4.27 while measured at both the Pr (930.3 eV) and Cu (932.8 eV) resonant energies. The 3D CO is still observable at room temperature (300 K) at both energies, constituting another aspect which sets the 3D CO in PYBCO apart from other observations.

While the reciprocal space dependence suggests this observed scattering signal is most likely 3D CO, the decisive affirmation of this phenomenon arises from the temperature dependence. Starting at room temperature (300 K), it can be seen that the scattering intensity increases until $T = T_c$, where a cusp-like maximum is observed, followed by a reduced scattering intensity for $T < T_c$. As previously discussed, this behavior is a hallmark signature of the competition between the SC and CO phases and is universally observed for all reported 2D and 3D CO observations in the YBCO system, thereby confirming that the observed scattering signal indeed results from CO (with the dimensionality confirmed by the L coordinate of $\mathbf{Q}_{CO}$, as well as by ξ_c).

The energy dependence of the width of the 3D CO is shown in panel A of Figure 4.28 up to 935 eV, after which the fits become non-representative of the actual signal widths due to low scattering intensity. The temperature dependence of the width of the 3D CO is shown in panel B of Figure 4.28 for all measured temperatures. The 3D CO peak width does not appear to vary significantly with either photon energy or temperature, likely due to the 3D CO correlation length being bounded by the coherence length of the crystal lattice.

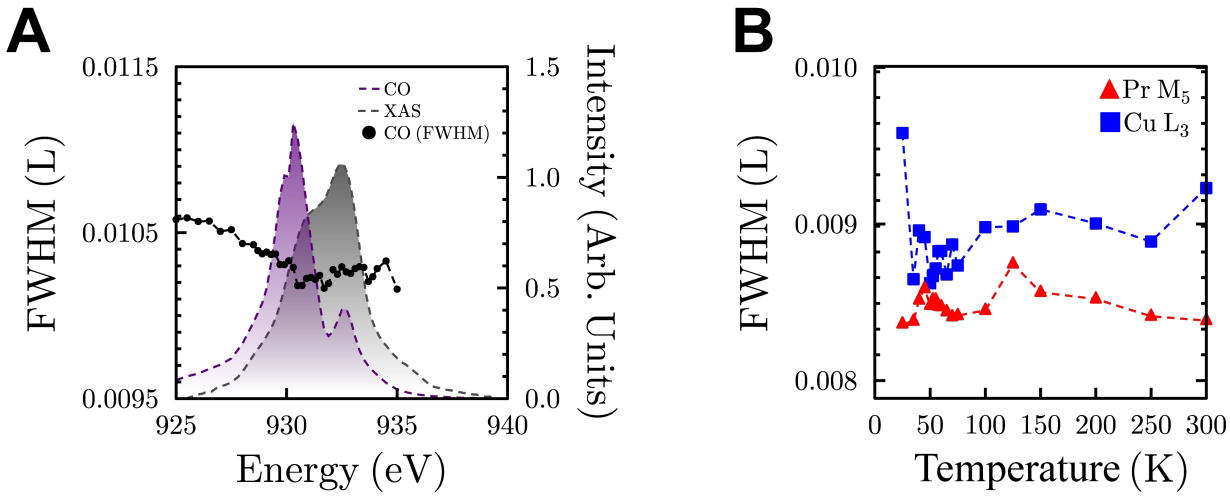

Figure 4.28: The full width at half maximum (FWHM) of the 3D CO peak in PYBCO measured along the out-of-plane (L) direction is displayed as a function of **A** energy (black), overlaid by the intensities of the x-ray absorption spectrum (XAS) (gray) and 3D CO energy dependence (purple), and **B** temperature, as measured at the Pr M_5 (red) and Cu L_3 (blue) resonance energies.

The dependence of the 3D CO scattering intensity on incident photon polarization is shown in Figure 4.29 at both the Pr (930.3 eV) and Cu (932.8 eV) resonant energies, for x-rays polarized in-plane (σ-polarized) and out-of-plane (π-polarized). The 3D CO scattering intensity is significantly stronger for σ-polarized x-rays than for π-polarized x-rays for both energies. This is certainly to be expected at the Cu resonance, due to the 2D symmetry of the dominant $3d_{x^2-y^2}$ orbital which yields a similar in-plane versus out-of-plane anisotropy in the observed absorption spectra (Figure 4.9). This result is more interesting for the Pr resonance, in which no such anisotropy in the XAS is observed and suggests that, although the Pr ions are somehow involved, it is still principally the planar Cu charge density that is ordering.

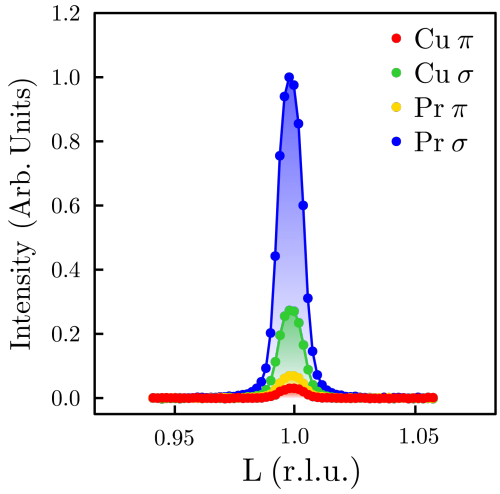

Figure 4.29: Rocking curve scans measured with incident photon π and σ polarizations at the Cu L_3 (red and green) and Pr M_5 (yellow and blue) resonant energies are shown.

To confirm the phenomenon of the stabilization of 3D CO by Pr-substitution, a second sample of PYBCO was measured using identical methods and a 3D CO was also observed. The SC transition temperature for this sample was measured to be $T_c = 50$ K due to having a slightly lower Pr content. This is corroborated by the XAS shown in panel A of Figure 4.30, which has an overall similar lineshape of overlapping Pr M_5 and Cu L_3 absorption edges as the XAS measured for the primary sample (Figure 4.27), but with a proportionally smaller contribution from the Pr edge. This is mirrored in the energy dependence of the 3D CO (also shown in panel A of Figure

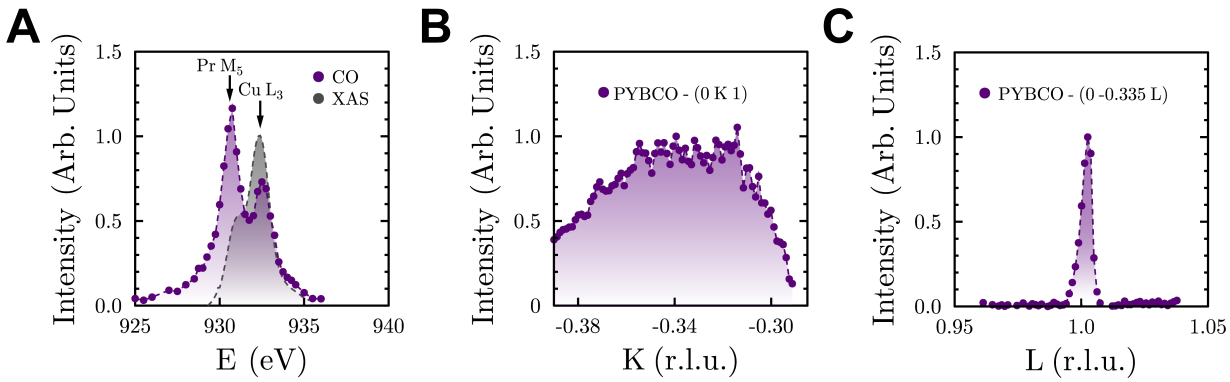

Figure 4.30: A 3D CO was observed in a second sample of PYBCO with a lower Pr concentration, corresponding to a critical temperature of T_c=55 K. **A** The x-ray absorption spectrum (XAS) (gray) and energy dependence of the 3D CO (purple) are similar to that of the first sample (Figure 4.27 A), but with greater spectral weight at the Cu L_3 resonance. Compared to the first sample (Figure 4.23 B,C), the 3D CO is similarly broad along the **B** K direction and narrow along the **C** L direction.

4.30), in which the relative proportions of scattering intensities at the Pr and Cu resonances is also shifted in favor of the Cu resonance, compared to the primary sample (Figure 4.27).

The reciprocal space structure of the 3D CO observed in the second sample is highly similar to the structure observed in the primary sample. Panels B and C of Figure 4.30 display the profile through the center of the 3D CO peak along the K and L axes, respectively. The 3D CO observed in the second sample is also very broad along the K direction and very narrow along the L direction. However, due to sample misalignment during the experiment, the correlation lengths cannot be extracted. Nonetheless, the qualitative characteristics of the energy, K, and L dependencies are consistent with the observations in the primary, confirming the existence of the 3D CO phenomenon in this system.

Now that the 3D CO in PYBCO has been established, the discussion turns to possible mechanisms by which the Pr-substitution may stabilize the 3D CO. Considering the known hybridization between Pr $4f$ and O $2p$ orbitals [70–72], in addition to Pr having the largest ionic radius of any lanthanide that may be substituted into the YBCO system without changing its structure [123], it is conceivable that substitution of the Pr ion may create an orbital bridge which

couples adjacent CuO_2 planes, as shown in Figure 4.31. The additional connectivity provided by the Pr $4f-$O $2p$ hybridization may provide the additional connectivity needed for a CO with 3D coherence to develop.

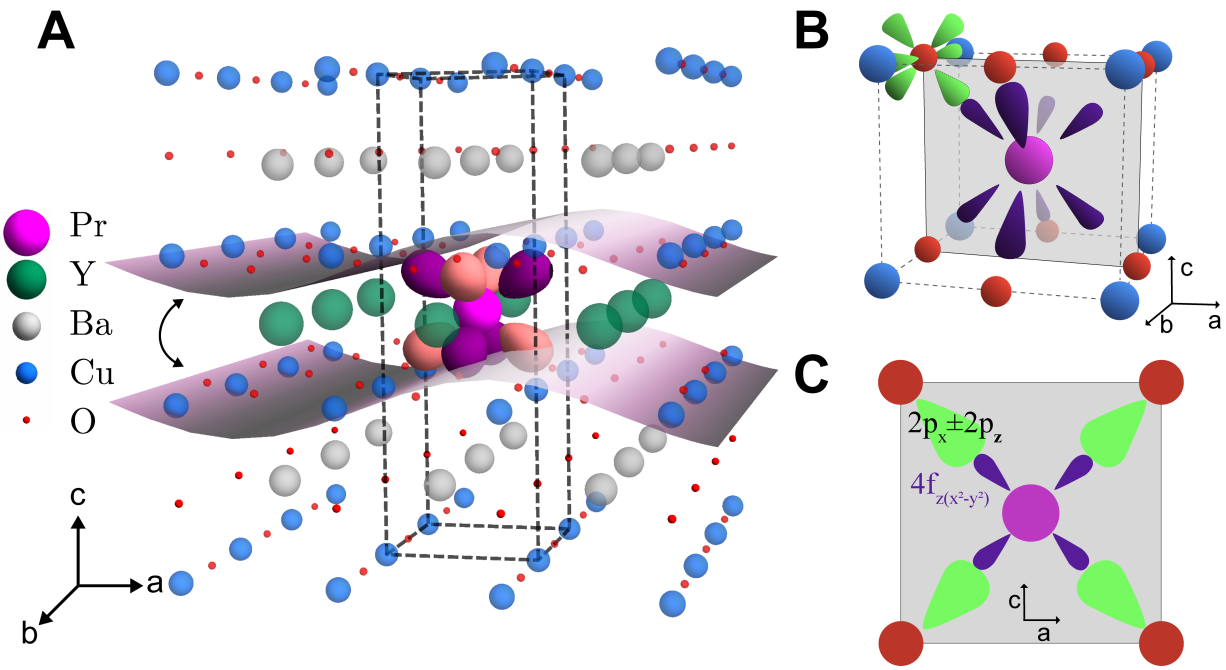

Figure 4.31: **A** A unit cell (dashed lines) within a PYBCO lattice is shown, illustrating the possible CO coupling (purple waves) between adjacent CuO_2 planes stabilized by Pr-substitution. The Pr $f_{z(x^2-y^2)}$ orbital is shown, which hybridizes with the planar O atoms. **B** The region of the unit cell between the CuO_2 planes is shown. The Pr $4f$ orbital can be seen hybridizing with the $2p$ orbital of an O atom within the adjacent CuO_2 plane. **C** The hybridization of Pr $4f_{z(x^2-y^2)}$ and O $2p_x \pm 2p_y$ orbitals is shown within the *ac*-plane through the center of the unit cell along the *b* direction.

DFT

To investigate the role of hybridization on 3D CO formation and its competition with SC, density-function theory (DFT) (Appendix C) calculations were performed (in this chapter only) by collaborator Prof. Yi Lu (Nanjing University) using WIEN2k [124, 125] for both $PrBa_2Cu_3O_{6+\delta}$ (PBCO) and $DyBa_2Cu_3O_{6+\delta}$ (DBCO). Because Pr-substitution in YBCO only yields 3D CO, while Dy-substitution in YBCO only yields 2D CO [126], performing DFT for

these two systems provides a more direct comparison of 2D CO versus 3D CO than a comparison against YBCO, in which both 2D and 3D CO have been observed. To reduce the computational complexity, $\delta = 0$ was used for both PBCO and DBCO. The resulting electronic band structures are shown in Figure 4.32 where the bands possessing O $2p$, Cu $3d$, and Pr/Dy $4f$ orbital character have been colored green, blue, and red, respectively.

The structure of the bands near the Fermi energy are overall similar for PBCO and DBCO. For example, the characteristic $pd\sigma$ bands of the CuO_2 planes responsible for observed 2D phenomena is easily seen for both compounds, with its 2D character verified by the lack of dispersion along the S→R points. However, there is one distinct and substantially relevant difference between the PBCO and DBCO band structures, which is the presence of an additional band with clear $4f$ character which crosses E_F in PBCO but not in DBCO. This difference is more clearly highlighted in Figure 4.33, which displays the planar band structures while only highlighting O $2p$ and Pr/Dy $4f$ orbital characters.

The most obvious difference between the planar band structures is the lack of any $4f$ character anywhere near E_F in DBCO, presumably resulting from the difference in electron configurations and lack of $4f - 2p$ hybridization in DBCO. It is clearly seen that the additional band which crosses E_F in PBCO has both Pr $4f$ and O $2p$ character. It has been shown that this band takes holes from the superconducting band as a result of the antibonding coupling between the Pr $4f_{z(x^2-y^2)}$ and O $2p_\pi$ states, yielding the observed T_c suppression [71]. It is possible that this orbital coupling synchronizes the phase of the 3D CO on adjacent CuO_2 planes, yielding the observed diffraction signal at L=1. In contrast, the top of the corresponding band in DBCO is buried deep below E_F at approximately -0.8 eV, effectively leaving the charge carriers in adjacent planes decoupled. This difference is illustrated schematically in panel C of Figure 4.33.

Another possible mechanism by which Pr-substitution stabilizes 3D CO may result from the observed unintentional substitution of Pr at the Ba sites and associated migration of O from the CuO_2 plane layers to the CuO chain layers, as discussed in Section 4.1.1. In principle, this should

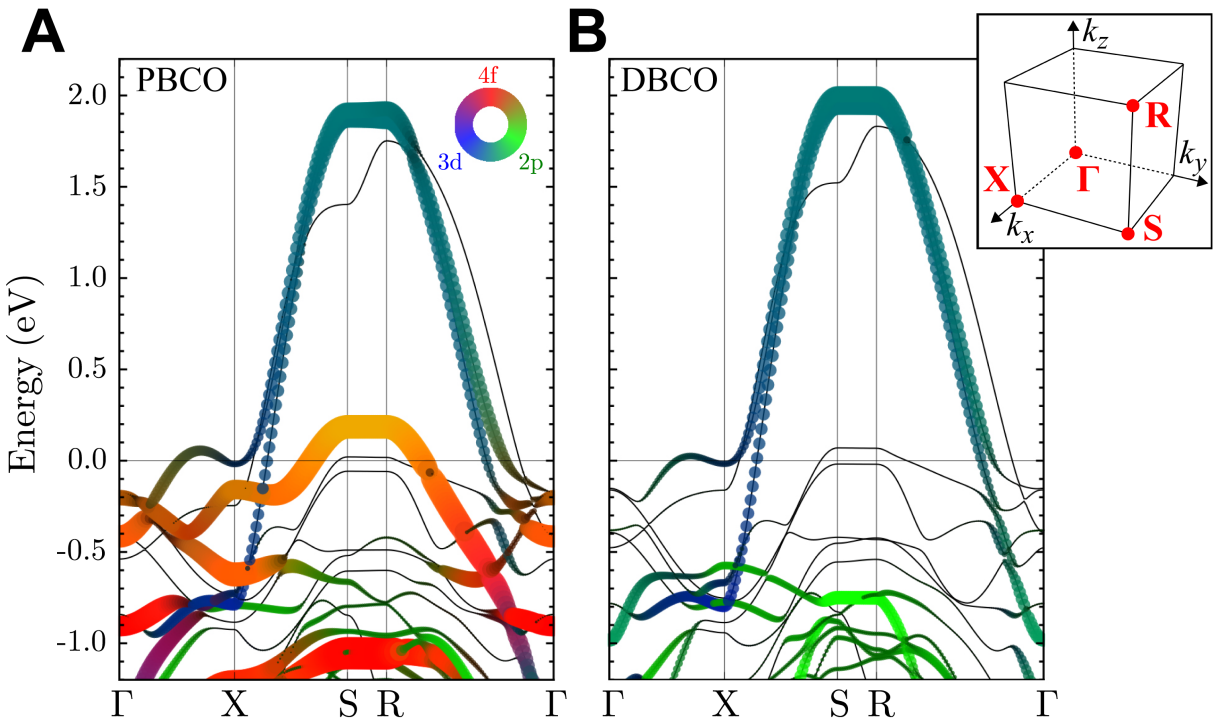

Figure 4.32: The three-dimensional band structures calculated by density-functional theory are shown for **A** PBCO and **B** DBCO in the majority spin channel. The Pr/Dy $4f$, Cu $3d_{x^2-y^2}$, and O $2p$ orbital characters of each band are represented with red, blue, and green colors, respectively. Unlike for DBCO, a band with mixed $4f$ and $2p$ character crosses the Fermi level near the S and R points in PBCO.

aid the 3D coherence of the CO formation. The O migration effectively creates a third CuO_2 plane per unit cell, though this is partially compensated by the loss of O from the existing CuO_2 layers. Furthermore, any Pr located at the Ba sites may undergo similar $4f-2p$ orbital hybridization with the O located in the existing and newly created CuO_2 layers, potentially providing a direct coupling pathway through the entire unit cell for cells in which the Y site and both Ba sites have been substituted by Pr. This potential hybridization is not straightforward to assume, however, as the O environments at the Y and Ba sites are slightly different due to the additional O located at the cell corners in the Ba layer. While it is difficult to directly assess its influence, it is likely that the samples of PYBCO measured in this work contain some degree of Pr-substitution at the Ba sites, based on comparing the degree of orthorhombic distortion with literature values [80].

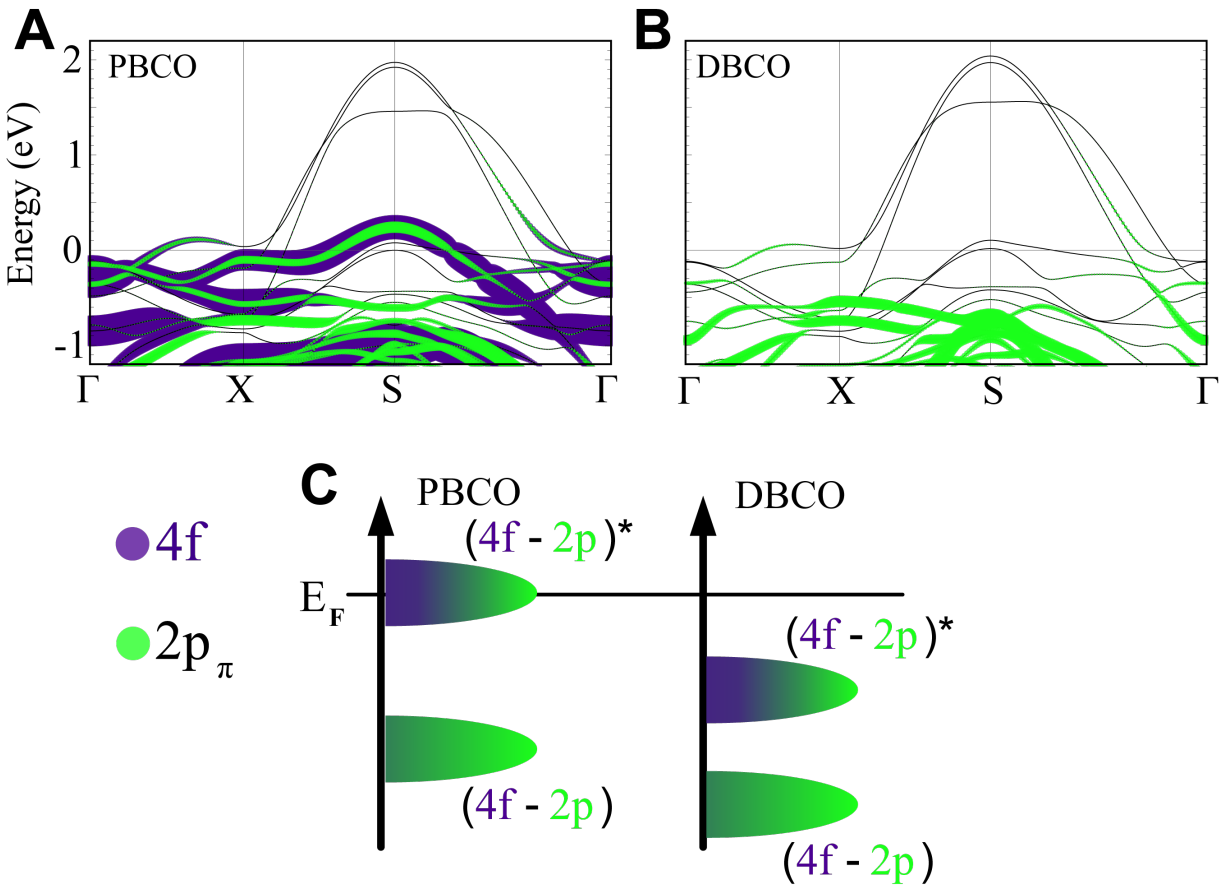

Figure 4.33: The two-dimensional band structures calculated by density-functional theory are shown for **A** PBCO and **B** DBCO in the majority spin channel. The Pr/Dy $4f$ and O $2p$ orbital characters of each band are represented with purple and green colors, respectively. The additional band which crosses the Fermi energy (E_F) in PBCO, but is buried deep below E_F in DBOCO, has both Pr $4f$ and O $2p_\pi$ character. **C** A schematic comparison of the proximity of the density of states from the $4f-2p$ bonding and anti-bonding (*) bands to E_F.

Similar to the hypothesis that the suppression of SC in PYBCO is a composite effect of Pr $4f-$O $2p$ hybridization and the aliovalent substitution of Pr at the Ba sites [84], it is possible that the stabilization of 3D CO by Pr-substitution is also due to a composite of these two effects. Further studies may provide clarity on this issue by comparing any observed 3D CO in samples synthesized under two different growth conditions in order to enhance/suppress the Ba-site solubility of the Pr ions.

IXS

While the mechanism of photon-mediated pairing, which was so effective at describing conventional SC, was quickly dismissed as being capable of inducing high-temperature SC due to the weak effects predicted by theoretical calculations, electron-phonon interactions (EPI) have recently regained attention as new theoretical works have shown that the incorporation of strong electron-electron interactions and antiferromagnetic correlations may strongly enhance the EPI effects, potentially constituting a large contribution to the pairing glue [127, 128].

Fingerprints of EPI effects have recently been observed in cuprates within the vicinity of CO, clearly elucidating the intertwinement of these two phases. One set of studies has revealed a giant phonon anomaly which displays a strong renormalization of both energy and linewidth across the CO ordering temperature [129, 130]. Another study on YBCO has observed a pronounced softening, known as a Kohn anomaly [131], of an acoustic phonon mode that is associated with 2D CO. However, applying uniaxial strain to stabilize 3D CO suppresses the Kohn anomaly in the acoustic mode while inducing a Kohn anomaly in an optical mode [115].

To investigate any phonon anomalies associated with the 3D CO formation in PYBCO, inelastic x-ray scattering (IXS) techniques were used to measure the phonon dispersion in $Pr_xY_{1-x}Ba_2Cu_3O_7$ for $x = 0.4$ in the vicinity of $\mathbf{Q}_{CO}$. The IXS measurements were measured at Sector 30 ID of the Advanced Photon Source at Argonne National Laboratory (ANL, USA). The IXS data was collected using the HERIX spectrometer using a beam energy of 23.71 keV with an energy resolution of 1.5 meV. The temperature fixed at $T_c = 43K$, where the 3D CO scattering intensity should be maximal. The phonon dispersion measured along the K direction at $L = 9$ (r.l.u.) is shown in Figure 4.34.

Although no Kohn anomalies can be observed in either of the measured acoustic or optical phonon modes, this result is inconclusive because no 3D CO could be found in this sample. However, there are some insights to be gained from the inconclusive result. Even though the IXS data was collected in reflection mode, the experiment was initially designed to be performed

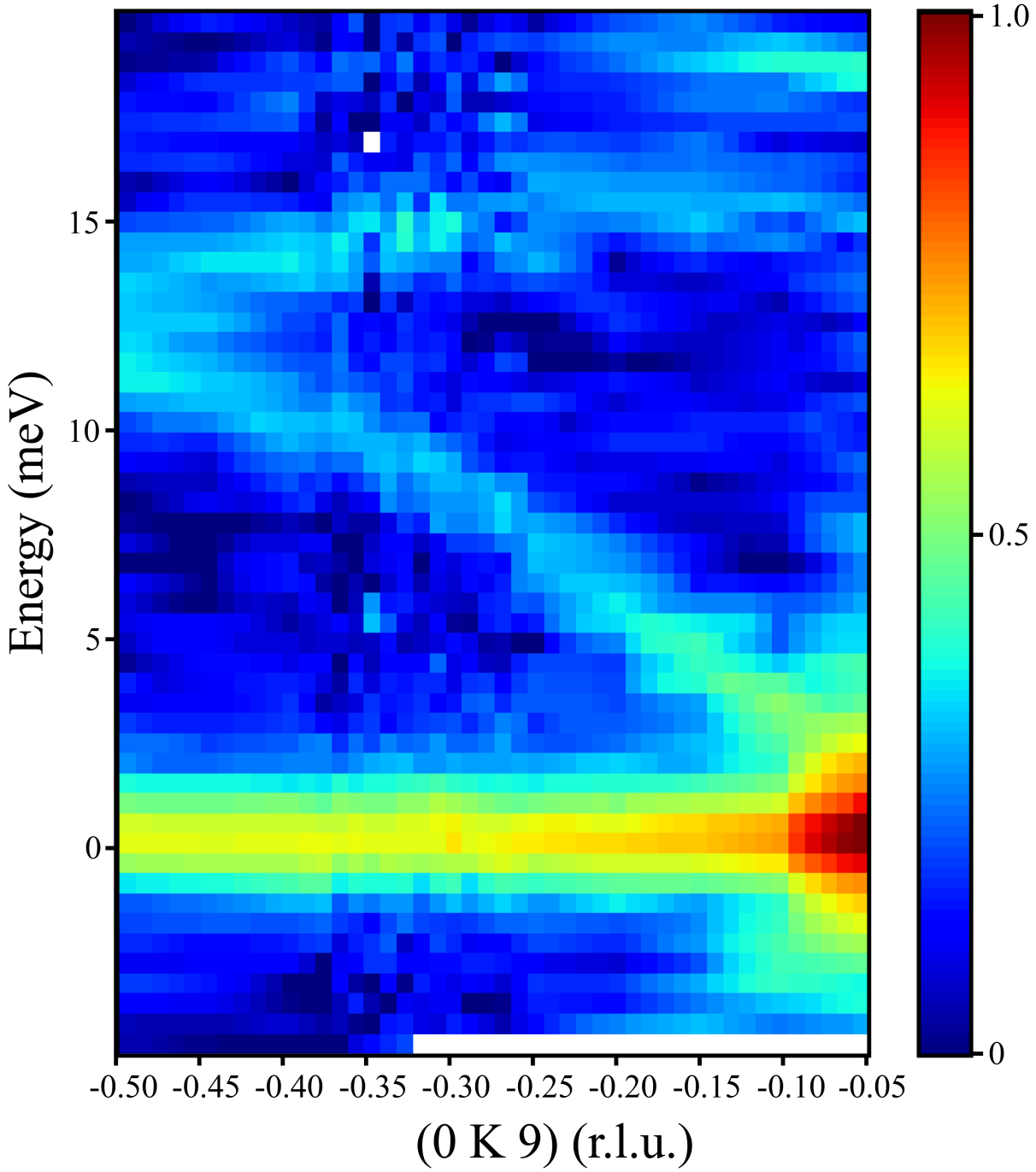

Figure 4.34: Dispersion of optical and acoustic phonon modes in PYBCO near the expected 3D CO wavevector.

in transmission mode, which required thinning the sample to $\sim$100 μm. Because the thinning process is not reversible, a different sample of PYBCO was used for this experiment rather than either of the samples in which the 3D CO had already been observed.

There are a few possible explanations for why no 3D CO was observed in this sample. It is possible that the 3D CO formation is a surface or near-surface effect that was disrupted by the thinning procedure. This could be further investigated by measuring a sample with 3D CO after polished away different amounts of material to see how the 3D CO changes with depth from the surface. Although the Pr content in this sample ($x = 0.4$) is relatively close to the the samples where the 3D CO was observed ($x = 0.3$), it is possible that the lack of CO is a result of the increased Pr content. Alternatively, it may not be the Pr concentration that has suppressed the 3D CO but rather some unintended variation in the sample synthesis which has altered the degree of Pr-substitution at the Ba sites. Further studies measuring the 3D CO as functions of Pr content and Ba stoichiometry could provide clarity to these conjectures.

Chapter 4.2.4, in full, is a reprint of the material as it appears in Nature Communications in Stabilization of three-dimensional charge order through interplanar orbital hybridization in $Pr_xY_{1-x}Ba_2Cu_3O_{6+\delta}$. A. Ruiz, B. Gunn, Y. Lu, K. Sasmal, C. M. Moir, R. Basak, H. Huang, J.-S. Lee, F. Rodolakis, T. J. Boyle, M. Walker, Y. He, S. Blanco-Canosa, E. H. da Silva Neto, M. B. Maple, and A. Frañó, Nature Communications, 2022. The dissertation author was a primary investigator and author of this paper.

Chapter 5

Charge Order in FeGe

5.1 The Kagome Lattice

The rich physics of condensed matter systems emerge from the strong correlations of its constituent electrons. Often, these electronic correlations are created by localizing electrons to enhance Coulomb interactions, from which exotic quantum many-body phases may emerge, depending on the Fermiology of the material. The two-dimensional kagome lattice, which is formed by corner-sharing triangles, as shown in Figure 5.1, and belongs to the same *P6/mmm* space group as graphene [132], constitutes one such example which has been demonstrated to support a multitude of quantum phases, such as superconductivity (SC) [133], charge order (CO) [134], and nematicity [135].

The electronic band structure of the kagome lattice is replete with many notable features, as shown in Figure 5.2. At the Brillouin zone corners (K points) lie Dirac cones, which promote non-trivial topology by protecting the associated Dirac bands from hybridization due to the lattice symmetry [134]. Additionally, a pair of van Hove singularities (VHSs) lead to a substantial increase of the density of states at the Brillouin zone edges, driving Fermi surface instabilities which give rise to various correlated phenomena [137]. Perhaps most notably, a perfectly flat band

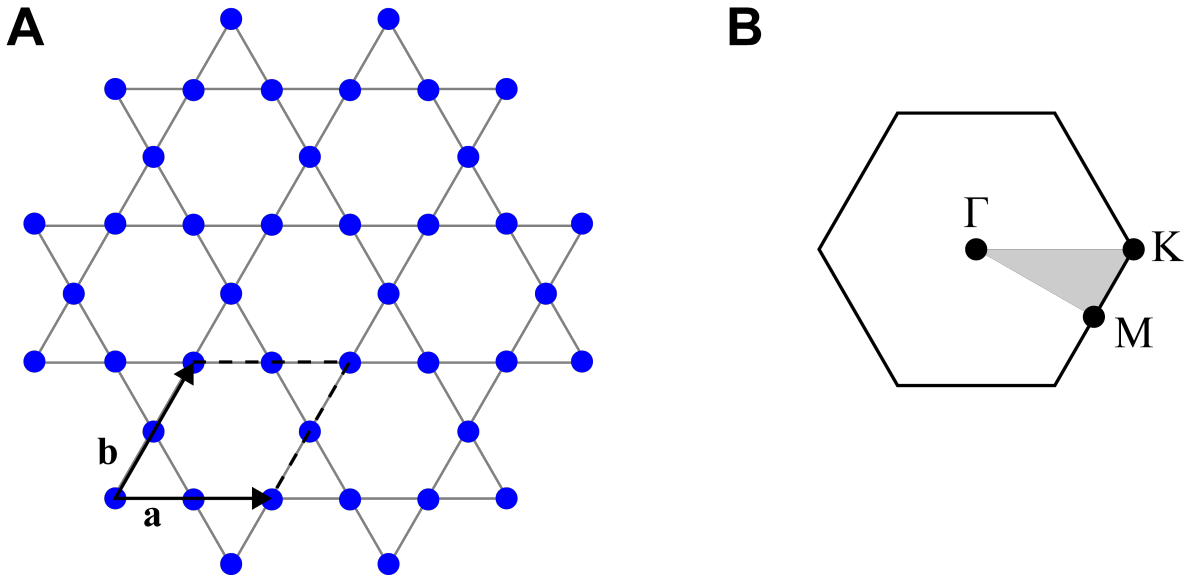

Figure 5.1: **A** The hexagonal kagome lattice is formed by corner-sharing triangles. The conventional unit cell (dashed) is constructed with the **a** and **b** lattice vectors. **B** The Brillouin zone of the kagome lattice. The irreducible Brillouin zone is highlighted in gray. Adapted from [136].

crosses the entire Brillouin zone which results from the exact cancellation of eigen-wavefunction hoppings arising from the unique lattice geometry [138]. The three corners of each triangle yield a geometrically frustrated structure for spin systems which generates a large number of degenerate ground states within the nearest-neighbor antiferromagnetic (AFM) Heisenberg model [133, 139], making the kagome system a promising candidate for hosting quantum spin liquid states [133, 140, 141]. The unique combinations of features embedded within the kagome band structure makes kagome materials ideal candidates for the exploration of novel physics arising from the interplay between geometry, topology, and magnetism at the quantum level.

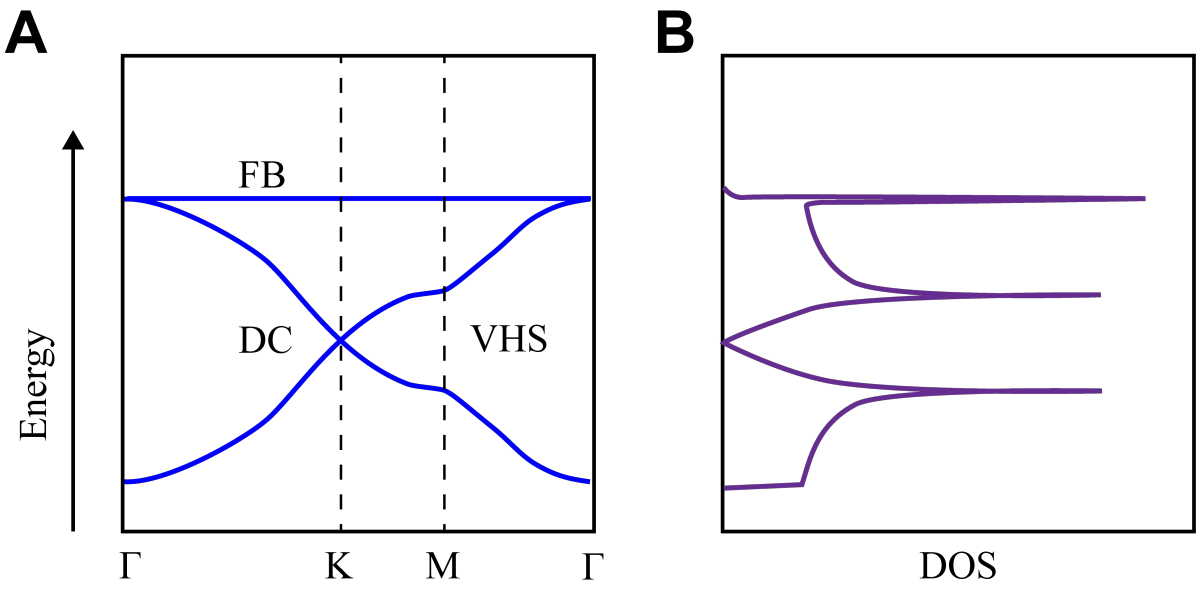

Figure 5.2: **A** The electronic band structure of the kagome lattice contains a flat band (FB) across the Brillouin zone, Dirac cone (DC) at the Brillouin zone corner (K points), and pair of van Hove singularities (VHSs) at the Brillouin zone edges (M points). **B** The FB and VHSs result in significant enhancements in the density of states (DOS) at these points. Adapted from [142, 143].

5.1.1 The FeGe System

Hexagonal FeGe consists of alternating stacks of iron (Fe) kagome layers and germanium (Ge) honeycomb layers, as shown in Figure 5.3. Below a Néel temperature $T_N = 410$ K, A-type AFM order appears with the Fe moments aligned ferromagnetically within individual kagome layers, and anti-aligned between layers. Two distinct COs emerge below $T_{CO} \approx 110$ K — one in-plane with $\mathbf{Q}_{CO1}$=($\frac{1}{2}$ 0 0), and the other out-of-plane with $\mathbf{Q}_{CO2}$=(0 0 $\frac{1}{2}$). Finally, below $\sim$60 K, the Fe magnetic moments become canted from the c-direction, forming a c-axis double cone AFM structure. Enhancement of the magnetic moment at the onset of the CO suggests that the CO and AFM orders may be strongly coupled. Moreover, density-functional theory (DFT) calculations observe an interaction-driven magnetic splitting of the spin-minority and spin-majority kagome bands within each Fe layer, resulting in an upshift of the spin-minority VHS towards the Fermi energy (E_F) with temperature, until the VHS ultimately opens a gap at

E_F with the onset of CO [142, 144]. However, due to the high degree of electronic correlations in FeGe, DFT calculations cannot capture all details of experimental observations. Because DFT alone cannot stabilize CO in FeGe, in addition to the absence of CO in another A-type AFM kagome system, FeSn [145], a purely nesting-driven origin to the CO seems unlikely [142]. Hints of its exotic nature continue to surface, as recent scanning tunneling microscopy experiments have shown that the CO within individual Fe kagome layers exhibits a chirality which alternates with the AFM ordering [135].

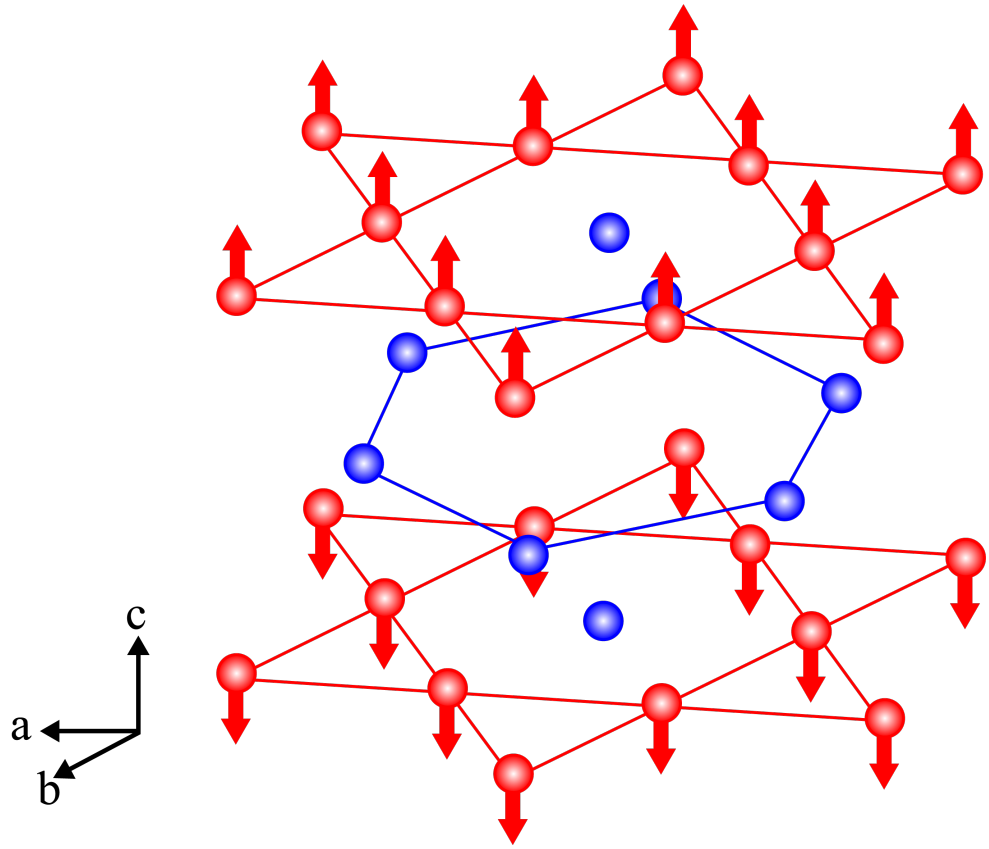

Figure 5.3: The hexagonal FeGe structure consists of alternating stacks of iron (Fe) kagome layers (red) and germanium (Ge) honeycomb layers (blue). Below a Néel temperature $T_N = 410$ K, A-type AFM order appears with the Fe moments aligned ferromagnetically within individual kagome layers, and anti-aligned between layers. Adapted from [135].

Furthermore, angle-resolved photoemission spectroscopy (ARPES) measurements observe a kink in the CO dispersion, as observed in many unconventional superconductors [146],

suggesting an electron-boson coupling to either phonons or magnons. The nature of this coupling was investigated by inelastic neutron scattering, which did not observe an acoustic phonon mode softening at the CO scattering vectors and ruled out the possibility for electron-magnon coupling. However, hardening of an optical phonon mode was observed through the CO transition temperature at the exact energy ($\sim$30 meV) where the kink is observed in the ARPES spectra upon opening of the CO gap [142]. The identified A_{2u} optical phonon mode corresponds to motion involving both Fe atoms with the kagome layers, as well as Ge atoms between the kagome layers, indicating active involvement by the Ge atoms in the CO formation. Furthermore, it has been hypothesized that entwinement between magnetism and CO interactions yields a generalized Kekulé distortion within the Ge honeycomb, in which the honeycomb lattice distorts from its planar structure, similar to that observed in graphene [147], without affecting the positions of the Fe atoms in the kagome layers [148].

5.2 Results

5.2.1 Charge Ordering at the Ge *K* Edge

REXS

To further investigate the role of the Ge honeycomb in the CO formation in FeGe, resonant elastic x-ray scattering (REXS) measurements were performed on a sample of hexagonal FeGe, shown in Figure 5.4. The sample was grown as a single crystal by collaborator Prof. Pengcheng Dai's group (Rice University) by the chemical vapor transport method described in [149]. The sample is grown with the *a* axis parallel to the surface normal and the lattice parameters are a=b=5.0 Å and c=4.1 Å. The crystal orientation and the absence of impurity phases, such as Fe_2Ge_3 and Fe_6Ge_5, were confirmed by x-ray diffraction measurements.

The REXS experiment was conducted at Sector 6 ID of the Advanced Photon Source

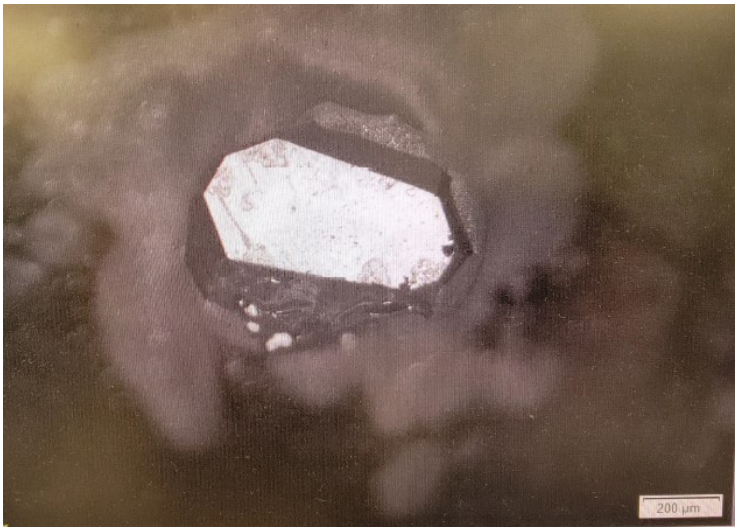

Figure 5.4: The sample of FeGe that was measured by REXS.

at Argonne National Laboratory (ANL, USA) using the same scattering geometry shown in Figure 3.10. The measurements were performed by tuning the incident beam energy across the Ge K edge ($1s \rightarrow 2p$ transition) from approximately 11.05 keV to 11.15 keV while keeping the scattering vector fixed at $\mathbf{Q}_{CO1}$=($\frac{1}{2}$ 0 0). The measurements were repeated in 5 K decrements from 110 K to 90 K. Upon cooling below $T_{CO} \approx 110$ K, a peak emerges at 10.077 keV, as shown in panel A of Figure 5.5. The integrated area of this peak is plotted as a function of temperature in panel B of Figure 5.5 and is suggestive of a second-order phase transition. In addition to the scattering vector and observed transition temperature being in agreement with literature reports, this further corroborates that the origin of this peak is due to CO.

The CO peak is located 25.0 eV below the Ge K step edge and matches the step edge scattering intensity for temperatures below $T \approx$95 K. The observed pre-edge separation and similar scattering intensity relative to the step edge bears a striking resemblance to the pre-edge structure observed in the carbon (C) K x-ray absorption spectrum (XAS) of highly oriented pyrolytic graphite (HOPG), which is composed of 2D C honeycomb layers. The pre-edge peak observed in the HOPG XAS is associated with dipole-allowed transitions of C $1s$ electrons into empty $\pi 2p_z$ orbitals that are oriented perpendicular to the C honeycomb layers and is

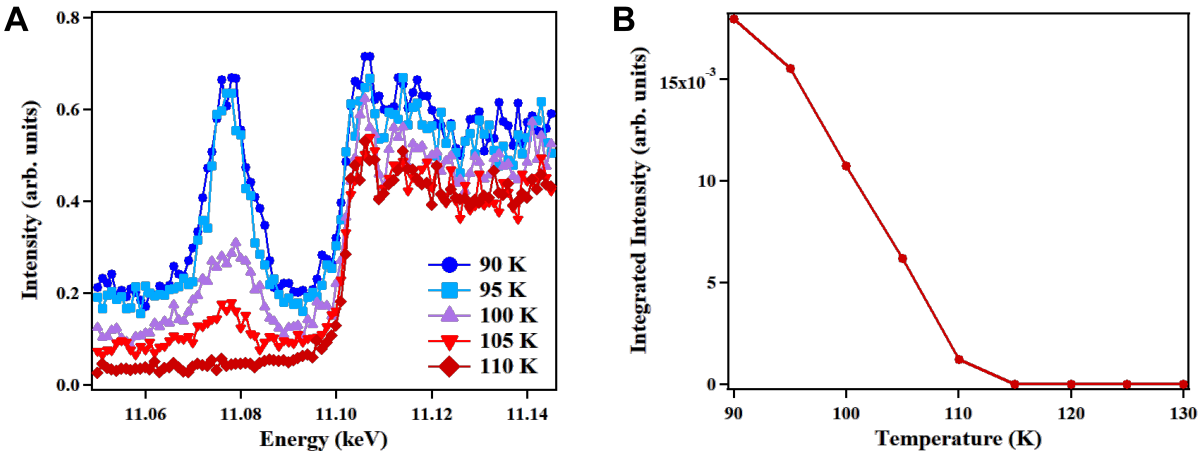

Figure 5.5: **A** Resonant elastic x-ray scattering measurements at **Q**=(1.5, 0, 0) near the Ge *K*-edge are shown for various temperatures between 90-110 K. As the temperature decreases, a feature emerges roughly 25 eV below the edge step. **B** Plotting the integrated area of this features as a function of temperature is suggestive of a second-order phase transition around 115 K.

considered a fingerprint of the trigonal coordination of C atoms in graphene-like structures [150]. Considering the similarities between C in HOPG and Ge in FeGe, namely, both sharing the same 2D honeycomb structure and belonging to Group 14 of the periodic table of elements, this provides further support that the Ge atoms are involved in the CO formation.

DFT

To obtain further insight about the electronic character of the observed CO peak, DFT calculations (Appendix C) were performed to obtain the band structure for FeGe. The DFT calculations were performed using WIEN2k [124, 125] using the Perdew-Burke-Ernzerhof generalized-gradient approximation for the exchange-correlation potential [151]. The calculated FeGe band structure is shown in Figure 5.6. The most notable feature is a set of relatively flat bands that are located approximately 25 eV below E_F, which is in close agreement with the energy of the emergent CO peak observed in the REXS measurements. Furthermore, the DFT calculations show that these bands have predominately Ge 3*d* character, providing further evidence of the involvement by Ge atoms in the FeGe CO formation and supporting the the generalized Kekulé

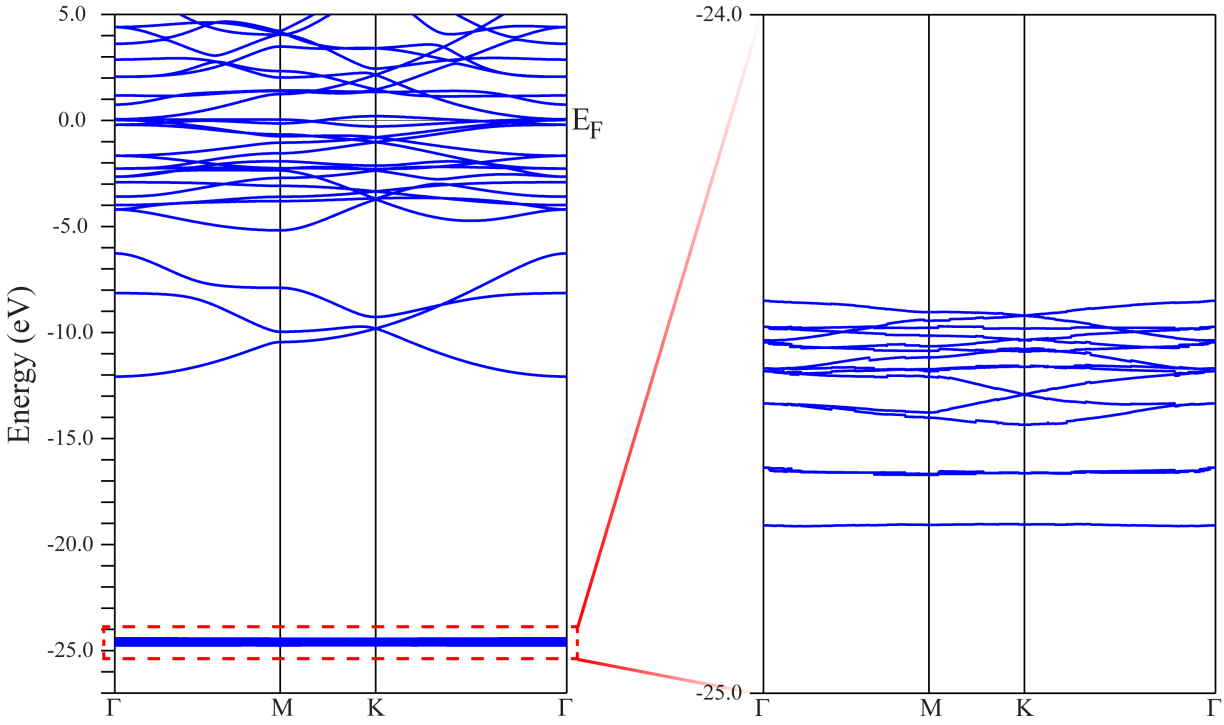

Figure 5.6: The band structure of FeGe calculated from density-function theory is shown. A flat pocket of Ge 3*d* bands is observed nearly 25 eV below the Fermi energy.

distortion hypothesis.

Future Work

At the time of writing, this research project is still ongoing. Future experiments will examine the temperature dependence of the $\mathbf{Q}_{CO1}$ peak at the Ge *K* edge to lower temperatures, below the canted AFM transition, as well as its energy dependence. These measurements will be repeated at the Fe *K* edge (∼7.1 keV) and for $\mathbf{Q}_{CO2}$. The aim of these experiments is to answer the following questions:

1. What are the fundamental differences in characteristics (e.g., correlation lengths, modulation size) of the in-plane versus out-of-plane COs?

2. What is the role of the Fe kagome lattice versus the role of the Ge honeycomb lattice on each type of CO formation?

3. How are the charge and magnetic orders intertwined? How does each type of CO interact with each type of AFM order?

Hosting two distinct COs, two AFM orders, and two unique band structures arising from geometric frustration, all of which show signs of intertwinement, the FeGe system is clearly replete with interactions between geometry, topology, and magnetism at the quantum level. The REXS measurements and DFT results illustrate that the CO formation in this system is highly non-trivial, warranting further investigation.

Appendix A

Fermi's Golden Rule

The transition rates between electronic states, such as in the cases of x-ray absorption and resonant x-ray scattering, are described by Fermi's golden rule (adapted from [152]):

Let $|\Psi_{t_0}\rangle$ be an unperturbed quantum state at time $t = t_0$. At time t, it evolves to the state $|\Psi_t\rangle$ by the unperturbed Hamiltonian operator, $\hat{H}_0$, according to the time-dependent Schrödinger equation

$$i\,\hbar\frac{\partial}{\partial t}|\Psi_t\rangle = \hat{H}_0|\Psi_t\rangle$$

If $|\Psi_{t_0}\rangle = |i\rangle$ is an eigenstate with the eigenvalue E_0 such that

$$\hat{H}_0|\Psi_{t_0}\rangle = E_0|\Psi_{t_0}\rangle$$

then

$$|\Psi_t\rangle = e^{-i\frac{E_0}{\hbar}(t-t_0)}|\Psi_{t_0}\rangle$$

Thus, its eigenvector rotates in Hilbert space with frequency $\omega_0 = \frac{E_0}{\hbar}$. $|\Psi_t\rangle$ is a stationary state because $\langle\Psi_t|\Psi_t\rangle = \langle\Psi_{t_0}|\Psi_{t_0}\rangle$ does not vary with time. Let $\hat{W}_t$ be a time-dependent

perturbation. Then, the Schrödinger equation describing the time evolution of $|\Psi_t\rangle$ is

$$i\,\hbar\frac{\partial}{\partial t}|\Psi_t\rangle = [\hat{H}_0 + \hat{W}_t]|\Psi_t\rangle$$

While any quantum state at future time t may be determined by solving this equation, it is, in general, not solvable. Due to the perturbation, the state $|\Psi_t\rangle$ is no longer stationary, resulting in a particle being scattered from initial state $|i\rangle$ to final state $|f\rangle$. Using the transformation

$$|\Psi_t\rangle = e^{-i\frac{\hat{H}_0}{\hbar}t}|\Psi(t)\rangle$$

we can change from the *Schrödinger picture* to the *interaction picture*, where the unperturbed state vectors do not change with time. Applying this transformation to the Schrödinger equation yields

$$\begin{aligned} i\,\hbar\left(-\frac{i}{\hbar}\hat{H}_0 e^{-i\frac{\hat{H}_0}{\hbar}t}|\Psi(t)\rangle + e^{-i\frac{\hat{H}_0}{\hbar}t}\frac{\partial}{\partial t}|\Psi(t)\rangle\right) &= [\hat{H}_0 + \hat{W}_t]e^{-i\frac{\hat{H}_0}{\hbar}t}|\Psi(t)\rangle \\ i\,\hbar\frac{\partial}{\partial t}|\Psi(t)\rangle &= e^{+i\frac{\hat{H}_0}{\hbar}t}\hat{W}_t e^{-i\frac{\hat{H}_0}{\hbar}t}|\Psi(t)\rangle \\ i\,\hbar\frac{\partial}{\partial t}|\Psi(t)\rangle &= \hat{W}(t)|\Psi(t)\rangle \end{aligned}$$

where $\hat{W}(t) = e^{+i\frac{\hat{H}_0}{\hbar}t}\hat{W}_t e^{-i\frac{\hat{H}_0}{\hbar}t}$. We can confirm the unperturbed state vectors do not vary in time in this representation by setting $\hat{W}_t = \hat{W}(t) = 0$, which yields $i\,\hbar\frac{\partial}{\partial t}|\Psi(t)\rangle = 0$. By integrating the Schrödinger equation, we obtain the recursive relation

$$|\Psi(t)\rangle = |\Psi(t_0)\rangle + \frac{1}{i\,\hbar}\int_{t_0}^{t} dt'\,\hat{W}(t')|\Psi(t')\rangle$$

Upon successive iteration, we obtain the perturbation series

$$|\Psi(t)\rangle = |\Psi(t_0)\rangle + \frac{1}{i\,\hbar}\int_{t_0}^{t} dt'\,\hat{W}(t')|\Psi(t_0)\rangle + \frac{1}{(i\,\hbar)^2}\int_{t_0}^{t} dt'\,\hat{W}(t')\int_{t_0}^{t'} dt''\,\hat{W}(t'')|\Psi(t_0)\rangle + ...$$

The first term in this sum is proportional to W^0, the second is proportional to W^1, the third is proportional to W^2, and so on. Because the perturbation, W, is necessarily small, each term in the sum contributes less than the term before it. Keeping only the terms up to first order yields

$$|\Psi(t)\rangle \approx |\Psi(t_0)\rangle + \frac{1}{i\,\hbar}\int_{t_0}^{t} dt'\,\hat{W}(t')|\Psi(t_0)\rangle$$

Let $|\Psi_{t_0}\rangle = |i\rangle$ be the initial state at $t = t_0$. The probability amplitude of the system being in the final state $|f\rangle$ at time $t > t_0$ is

$$\langle f|\Psi_t\rangle = \langle f|e^{-i\frac{\hat{H}_0}{\hbar}t}\Psi(t)\rangle = e^{-i\frac{E_0}{\hbar}t}\langle f|\Psi(t)\rangle$$

This implies that $|\langle f|\Psi_t\rangle|^2 = |\langle f|\Psi(t)\rangle|^2$. Let $\hat{W}_t = e^{\eta t}W(\boldsymbol{r})$ such that $\hat{W}$ slowly turns on from 0 as $t_0 \to -\infty$ to $W(\boldsymbol{r})$ for $t \geq 0$ in the limit that $\eta \to 0^+$. Then

$$
\begin{aligned}
\langle f|\Psi(t)\rangle &\approx \langle f|i\rangle + \frac{1}{i\,\hbar}\int_{t_0}^{t} dt'\ \langle f|\hat{W}(t')|i\rangle \\
&= 0 + \frac{1}{i\,\hbar}\int_{t_0}^{t} dt'\ \langle f|e^{+i\frac{\hat{H}_0}{\hbar}t'}\hat{W}_{t'}e^{-i\frac{\hat{H}_0}{\hbar}t}|i\rangle \\
&= \frac{1}{i\,\hbar}\int_{-\infty}^{t} dt'\ \langle f|e^{+i\frac{\hat{H}_0}{\hbar}t'}e^{\eta t'}We^{-i\frac{\hat{H}_0}{\hbar}t'}|i\rangle \\
&= \frac{\langle f|W|i\rangle}{i\,\hbar}\int_{-\infty}^{t} dt'\ e^{i\frac{E_f-E_i}{\hbar}t'}e^{\eta t'} \\
&= \frac{\langle f|W|i\rangle}{i\,\hbar}\frac{e^{i\frac{E_f-E_i}{\hbar}t'}e^{\eta t'}}{i\frac{E_f-E_i}{\hbar}+\eta}\Bigg|_{-\infty}^{t} \\
&= \langle f|W|i\rangle\frac{e^{i\frac{E_f-E_i}{\hbar}t}e^{\eta t}}{E_i-E_f+i\,\hbar\eta}
\end{aligned}
$$

Then, the probability of transitioning from state $|i\rangle$ to state $|f\rangle$ at time t is

$$
\begin{aligned}
|\langle f|\Psi_t\rangle|^2 &= |\langle f|\Psi(t)\rangle|^2 \\
&\approx |\langle f|W|i\rangle|^2\frac{e^{2\eta t}}{(E_i-E_f)^2+(\hbar\eta)^2}
\end{aligned}
$$

and the transition rate from $|i\rangle \to |f\rangle$ is given by

$$
\begin{aligned}
T_{i\to f} &= \frac{d}{dt}|\langle f|\Psi(t)\rangle|^2 \\
&\approx |\langle f|W|i\rangle|^2\frac{2\eta}{(E_i-E_f)^2+(\hbar\eta)^2}e^{2\eta t}
\end{aligned}
$$

We now take the limit as $\eta \to 0^+$. It is straightforward to evaluate $\lim_{\eta\to 0^+} e^{2\eta t} = 1$, but $\lim_{\eta\to 0^+}\frac{2\eta}{(E_i-E_f)^2+(\hbar\eta)^2}$ yields the indeterminate $\frac{0}{0}$ in the case that $E_i = E_f$. The quantity can be evaluated using the identities $\lim_{\eta\to 0^+}\frac{2\eta}{x^2+\eta^2} = \lim_{\eta\to 0^+}\frac{1}{i}\left[\frac{1}{x-i\eta}-\frac{1}{x+i\eta}\right] = 2\pi\delta(x)$ and

$\delta(ax) = \frac{\delta(x)}{|a|}$ to yield *Fermi's golden rule*

$$T_{i\to f} \approx \frac{2\pi}{\hbar}|\langle f|W|i\rangle|^2\delta(E_i - E_f)$$

A.1 Oscillating Perturbations

Let us now calculate Fermi's golden rule for a perturbation which oscillates in time with frequency ω, such as in the case of an electron interacting with the electric field of an x-ray. Following the same arguments as before, let

$$W_t = 2We^{\eta t}cos(\omega t) = e^{\eta t}W(e^{i\omega t} + e^{-i\omega t})$$

The transition amplitude is then

$$\begin{aligned}
\langle f|\Psi(t)\rangle &\approx \frac{\langle f|W|i\rangle}{i\,\hbar}\int_{-\infty}^{t} dt'\, e^{\eta t'}\left(e^{i\frac{E_f-E_0+\hbar\omega}{\hbar}t'} + e^{i\frac{E_f-E_0-\hbar\omega}{\hbar}t'}\right) \\
&= \langle f|W|i\rangle e^{\eta t'}\left(\frac{e^{i\frac{E_f-E_0+\hbar\omega}{\hbar}t'}}{E_i - E_f + \hbar\omega + i\,\hbar\eta} + \frac{e^{i\frac{E_f-E_0-\hbar\omega}{\hbar}t'}}{E_i - E_f - \hbar\omega + i\,\hbar\eta}\right)\Bigg|_{-\infty}^{t} \\
&= \langle f|W|i\rangle e^{\eta t}\left(\frac{e^{i\frac{E_f-E_0+\hbar\omega}{\hbar}t}}{E_i - E_f + \hbar\omega + i\,\hbar\eta} + \frac{e^{i\frac{E_f-E_0-\hbar\omega}{\hbar}t}}{E_i - E_f - \hbar\omega + i\,\hbar\eta}\right)
\end{aligned}$$

and the transition probability is

$$|\langle f|\Psi(t)\rangle|^2 \approx |\langle f|W|i\rangle|^2 e^{2\eta t}\left(\frac{1}{(E_i-E_f+\hbar\omega)^2+(\hbar\eta)^2}+\frac{1}{(E_i-E_f 0\hbar\omega)^2+(\hbar\eta)^2}\right.$$
$$+\frac{e^{2i\omega t}}{(E_i-E_f+\hbar\omega+i\,\hbar\eta)(E_i-E_f-\hbar\omega-i\,\hbar\eta)}$$
$$\left.+\frac{e^{-2i\omega t}}{(E_i-E_f+\hbar\omega-i\,\hbar\eta)(E_i-E_f-\hbar\omega+i\,\hbar\eta)}\right)$$

The transition rate is then

$$\frac{d}{dt}|\langle f|\Psi(t)\rangle|^2 \approx |\langle f|W|i\rangle|^2 e^{2\eta t}\left(\frac{2\eta}{(E_i-E_f+\hbar\omega)^2+(\hbar\eta)^2}+\frac{2\eta}{(E_i-E_f 0\hbar\omega)^2+(\hbar\eta)^2}\right.$$
$$+\frac{2(\eta+i\omega)e^{2i\omega t}}{(E_i-E_f+\hbar\omega+i\,\hbar\eta)(E_i-E_f-\hbar\omega-i\,\hbar\eta)}$$
$$\left.+\frac{2(\eta-i\omega)e^{-2i\omega t}}{(E_i-E_f+\hbar\omega-i\,\hbar\eta)(E_i-E_f-\hbar\omega+i\,\hbar\eta)}\right)$$
$$=|\langle f|W|i\rangle|^2 e^{2\eta t}$$
$$\times\left[\left(\frac{2\eta}{(E_i-E_f+\hbar\omega)^2+(\hbar\eta)^2}+\frac{2\eta}{(E_i-E_f-\hbar\omega)^2+(\hbar\eta)^2}\right)(1-\cos(2\omega t))\right.$$
$$\left.+2\sin(2\omega t)\left(\frac{E_i-Ef+\hbar\omega}{(E_i-E_f+\hbar\omega)^2+(\hbar\eta)^2}+\frac{E_i-Ef-\hbar\omega}{(E_i-E_f-\hbar\omega)^2+(\hbar\eta)^2}\right)\right]$$
$$=|\langle f|W|i\rangle|^2 e^{2\eta t}\left(\frac{2\eta}{(E_i-E_f+\hbar\omega)^2+(\hbar\eta)^2}+\frac{2\eta}{(E_i-E_f-\hbar\omega)^2+(\hbar\eta)^2}\right)$$

where in the last step we have used the fact that the time-averaged $\cos(2\omega t)$ and $\sin(2\omega t)$ equal 0. Taking $\lim_{\eta\to 0^+}$ as before yields Fermi's golden rule for oscillating perturbations

$$T_{i\to f}\approx\frac{2\pi}{\hbar}|\langle f|W|i\rangle|^2[\delta(E_i-E_f+\hbar\omega)+\delta(E_i-E_f-\hbar\omega)]$$

which may be separated into the two cases of *absorption* ($E_f=E_i+\hbar\omega$) and *emission* (($E_f=E_i-\hbar\omega$)):

$$T_{i\to f} \approx \frac{2\pi}{\hbar}|\langle f|W|i\rangle|^2\delta(E_i - E_f + \hbar\omega) \qquad \text{(absorption)}$$

$$T_{i\to f} \approx \frac{2\pi}{\hbar}|\langle f|W|i\rangle|^2\delta(E_i - E_f - \hbar\omega) \qquad \text{(emission)}$$

Appendix B

The Fourier Transform of a Bravais Lattice

The reciprocal lattice is most concisely defined as the Fourier transform of the direct lattice. This will first be illustrated for the simpler one-dimensional case before generalizing to a three-dimensional Bravais lattice (adapted from [153]):

A one-dimensional lattice can be modeled by an array of delta functions that are evenly spaced along the x axis with spacing a

$$f(x) = \sum_n \delta(x - na)$$

where n is an integer which indexes all sites on the one-dimensional lattice. Taking the Fourier transform of this function, we have

$$\begin{aligned}
\mathcal{F}\{f(x)\} &= \int_{-\infty}^{\infty} f(x) e^{ikx} dx \\
&= \int_{-\infty}^{\infty} \sum_n \delta(x - na) e^{ikx} dx \\
&= \sum_n \delta(k - \frac{2\pi n}{a})
\end{aligned}$$

Thus, the Fourier transform of a one-dimensional lattice with spacing a is itself a one-dimensional lattice with spacing $\frac{2\pi}{a}$.

For the set of primitive lattice vectors, $\{\boldsymbol{a_1}, \boldsymbol{a_2}, \boldsymbol{a_3}\}$, of the three-dimensional direct Bravais lattice, we can write

$$\boldsymbol{r} = r_1\boldsymbol{a_1} + r_2\boldsymbol{a_2} + r_3\boldsymbol{a_3}$$

where $\{r_1, r_2, r_3\}$ are real numbers. The three-dimensional Bravais lattice can then be described by the function

$$\sum_{n_1,n_2,n_3} \delta^3(\boldsymbol{r} - n_1\boldsymbol{a_1} - n_2\boldsymbol{a_2} - n_3\boldsymbol{a_3}) = \sum_{n_1} \delta(r_1 - n_1 a_1) \sum_{n_2} \delta(r_2 - n_2 a_2) \sum_{n_3} \delta(r_3 - n_3 a_3)$$

where $\{n_1, n_2, n_3\}$ are integers. In order to evaluate the Fourier transform of this function, we need $\boldsymbol{k} \cdot \boldsymbol{r}$. Let

$$\boldsymbol{k} = k_1\boldsymbol{b_1} + k_2\boldsymbol{b_2} + k_3\boldsymbol{b_3}$$

where $\{k_1, k_2, k_3\}$ are real numbers and $\{\boldsymbol{a_1}, \boldsymbol{a_2}, \boldsymbol{a_3}\}$ are vectors in reciprocal space. Then

$$\begin{aligned}\boldsymbol{k} \cdot \boldsymbol{r} = {} & r_1 k_1 \boldsymbol{a_1} \cdot \boldsymbol{b_1} + k_1 \boldsymbol{b_1} \cdot (r_2\boldsymbol{a_2} + r_3\boldsymbol{a_3}) \\ & + r_2 k_2 \boldsymbol{a_2} \cdot \boldsymbol{b_2} + k_2 \boldsymbol{b_2} \cdot (r_1\boldsymbol{a_1} + r_3\boldsymbol{a_3}) \\ & + r_3 k_3 \boldsymbol{a_3} \cdot \boldsymbol{b_3} + k_3 \boldsymbol{b_3} \cdot (r_1\boldsymbol{a_1} + r_2\boldsymbol{a_2})\end{aligned}$$

By choosing $\{\boldsymbol{b_1}, \boldsymbol{b_2}, \boldsymbol{b_3}\}$ such that

$$\boldsymbol{b_1} \cdot \boldsymbol{a_2} = \boldsymbol{b_1} \cdot \boldsymbol{a_3} = 0$$

$$\boldsymbol{b_2} \cdot \boldsymbol{a_1} = \boldsymbol{b_2} \cdot \boldsymbol{a_3} = 0$$

$$\boldsymbol{b_3} \cdot \boldsymbol{a_1} = \boldsymbol{b_3} \cdot \boldsymbol{a_2} = 0$$

the cross terms in $\boldsymbol{k} \cdot \boldsymbol{r}$ are all zero, leaving

$$\boldsymbol{k} \cdot \boldsymbol{r} = r_1 k_1 \boldsymbol{a_1} \cdot \boldsymbol{b_1} + r_2 k_2 \boldsymbol{a_2} \cdot \boldsymbol{b_2} + r_3 k_3 \boldsymbol{a_3} \cdot \boldsymbol{b_3}$$

The Fourier transform of the three-dimensional Bravais lattice is then just the product of three one-dimensional Fourier transforms

$$\begin{aligned}
&\mathcal{F}\{\sum_{n_1,n_2,n_3} \delta^3(\boldsymbol{r} - n_1\boldsymbol{a_1} - n_2\boldsymbol{a_2} - n_3\boldsymbol{a_3}) \\
&\qquad = \mathcal{F}\{\sum_{n_1} \delta(r_1 - n_1 a_1)\}\mathcal{F}\{\sum_{n_2} \delta(r_2 - n_2 a_2)\}\mathcal{F}\{\sum_{n_3} \delta(r_3 - n_3 a_3)\} \\
&\qquad = \sum_{n_1} \delta(k_1 - \frac{2\pi n_1}{a_1}) \sum_{n_2} \delta(k_2 - \frac{2\pi n_2}{a_2}) \sum_{n_3} \delta(k_3 - \frac{2\pi n_3}{a_3})
\end{aligned}$$

Thus, the Fourier transform of the three-dimensional Bravais lattice with spacing $\{a_1, a_2, a_3\}$ along the directions of the direct lattice vectors $\{\boldsymbol{a_1}, \boldsymbol{a_2}, \boldsymbol{a_3}\}$ is itself a three-dimensional Bravais lattice with spacing $\{\frac{2\pi}{a_1}, \frac{2\pi}{a_2}, \frac{2\pi}{a_3}\}$ along the directions of the reciprocal lattice vectors $\{\boldsymbol{b_1}, \boldsymbol{b_2}, \boldsymbol{b_3}\}$.

The reciprocal lattice vectors may be expressed in terms of the direct lattice vectors by enforcing the above requirement that $b_i a_j = b_i a_k = 0$ to define the direction, in addition to requiring their magnitudes are equal to $\frac{2\pi}{a_i}$. This yields

$$\boldsymbol{b_1} = \frac{2\pi}{V_{uc}} \boldsymbol{a_2} \times \boldsymbol{a_3}$$
$$\boldsymbol{b_2} = \frac{2\pi}{V_{uc}} \boldsymbol{a_1} \times \boldsymbol{a_3}$$
$$\boldsymbol{b_3} = \frac{2\pi}{V_{uc}} \boldsymbol{a_1} \times \boldsymbol{a_2}$$

where $V_{uc} = \boldsymbol{a}_1 \cdot (\boldsymbol{a}_2 \times \boldsymbol{a}_3)$ is the volume of the unit cell in real space.

Appendix C

Density-Functional Theory

Density-functional theory (DFT) is a powerful computational tool for approximating the solution to the Schrödinger equation for a many-body system. DFT can be used to calculate the structural, electronic, and magnetic properties of materials. DFT is much more computationally efficient than other theories, such as Hartree-Fock, by working with the electron density instead of the N-body wavefunction directly, thereby reducing the number of variables from $3N$ ($\{x,y,z\}$ for N electrons) to 3 (just $\{x,y,z\}$). Operating under the Born-Oppenheimer approximation, the comparatively massive nuclei are treated as fixed within some ionic configuration, producing a potential, $\hat{V}$, which operates on the electronic wavefunction. Because the kinetic energy, $\hat{T}$, and Coulomb interaction, $\hat{U}$, are the same for any N-electron system, it is $\hat{V}$ alone which distinguishes the Hamiltonian, $\hat{H}$, from one system to another. It's derivation is as follows (adapted from [154, 155]):

We start by expressing $\hat{V}$ in terms of the electron density operator, $\hat{n}(\boldsymbol{r})$

$$\hat{V}_{ext} = \sum_{i=1}^{N} V_{ext}(\boldsymbol{r}_i) = \int V_{ext}(\boldsymbol{r})\hat{n}(\boldsymbol{r})\, d\boldsymbol{r}$$

We then introduce two theorems by Walter Kohn and Pierre Hohenberg [156]

Theorem 1: *The ground state of a many-electron system is a functional of the electron*

density.

This theorem states that there is a one-to-one correspondence between a ground state wavefunction and the expectation value of its electron density.

Proof: Let $|\Psi\rangle$ and $|\Psi'\rangle$ be two ground state many-body wavefunctions corresponding to the two potentials $V_{ext}(\boldsymbol{r})$ and $V'_{ext}(\boldsymbol{r})$. Let both ground state wavefunctions have the same electron density expectation value, $\langle\Psi|\hat{n}(\boldsymbol{r})|\Psi\rangle = \langle\Psi'|\hat{n}(\boldsymbol{r})|\Psi'\rangle = n(\boldsymbol{r})$. Then

$$E' = \langle\Psi'|H'|\Psi'\rangle < \langle\Psi|H'|\Psi\rangle$$

where

$$\langle\Psi|H'|\Psi\rangle = \langle\Psi|H|\Psi\rangle + \langle\Psi|V' - V|\Psi\rangle$$

because $|\Psi\rangle$ is not the ground state of H'. Therefore

$$E' < E + \langle\Psi|V' - V|\Psi\rangle$$

A similar inequality is formed by interchanging the primed and unprimed quantities

$$E < E' + \langle\Psi'|V - V'|\Psi'\rangle$$

Adding these inequalities yields

$$\begin{aligned} E' + E &< E + E' + \langle\Psi'|V - V'|\Psi'\rangle + \langle\Psi|V' - V|\Psi\rangle \\ &< E + E' \end{aligned}$$

because $\langle\Psi|\hat{n}(\boldsymbol{r})|\Psi\rangle = \langle\Psi'|\hat{n}(\boldsymbol{r})|\Psi'\rangle$. Thus, we are left with the contradiction $E' + E < E + E'$

and must conclude that ground state wavefunctions for different potentials cannot have the same electron density.

Theorem 2: *The ground state energy can be expressed as a functional of the electron density, $E[n]$, which is minimized by the true ground state density.*

Proof: According to Theorem 1, every electron density, $n(\boldsymbol{r})$ has a corresponding unique ground state wavefunction, $|\Psi[n]\rangle$. We can then define an energy functional

$$E[n] = \langle\Psi[n]|H|\Psi[n]\rangle = \langle\Psi[n]|T+U|\Psi[n]\rangle + \int V_{ext}(\boldsymbol{r})n(\boldsymbol{r})\,d\boldsymbol{r}$$

where $n(\boldsymbol{r})$ is the true ground state density for the potential $V_{ext}(\boldsymbol{r})$. Let $n'(\boldsymbol{r})$ and $|\Psi'[n]\rangle$ be a different density and corresponding ground state wavefunction, respectively. Then

$$\begin{aligned} E[n'] &= \langle\Psi[n']|T+U|\Psi[n']\rangle + \int V_{ext}(\boldsymbol{r})n'(\boldsymbol{r})\,d\boldsymbol{r} \\ &= \langle\Psi[n']|H|\Psi[n']\rangle > E[n] \end{aligned}$$

because $|\Psi[n']\rangle$ is not the ground state of H. Therefore, $E[n]$ is minimized by the true ground state density, $n(\boldsymbol{r})$.

Thus, according to these two theorems, the information of the many-body wavefunction is encoded in the electron density, with the underlying complexity instead being relegated to the minimization of $E[n]$. The internal part of the energy functional, $E_i[n] = \langle\Psi[n]|T+U|\Psi[n]\rangle$, is difficult to compute for a system of interacting electrons. A straightforward and useful approach for doing so was implemented by Walter Kohn and Lu Sham [157], which involves breaking up $E_i[n]$ as

$$E_i[n] = T_S[n] + E_H[n] + E_{xc}[n]$$

$T_S[n]$ is the *internal energy functional* and describes the kinetic energy for a fictional system of *non-interacting* electrons with the same $n(\boldsymbol{r})$, in which a single Slater determinant, $|\Psi_S[n]\rangle$, describes the ground state and has the form

$$T_S[n] = -\frac{\hbar}{2m}\sum_{i,\sigma} n_{i,\sigma}\langle\phi_i|\nabla^2|\phi_i\rangle$$

where $n_{i,\sigma} \in \{0,1\}$ is the occupation number of single-particle orbital $|\phi_i\rangle$ and spin σ that sums to the total number of electrons, N. $E_H[n]$ is called the *Hartree functional* and describes the contribution due to the Coulomb interactions in $|\Psi_S[n]\rangle$

$$E_H[n] = \frac{1}{2}\int d\boldsymbol{r}\int d\boldsymbol{r}'\, n(\boldsymbol{r})\frac{e^2}{|\boldsymbol{r}-\boldsymbol{r}'|}$$

where

$$n(\boldsymbol{r}) = \sum_{i,\sigma} n_{i,\sigma}|\phi_i(\boldsymbol{r})|^2$$

E_{xc} is the *exchange-correlation energy functional* and describes the correlation energy due to the Pauli exchange interaction and does not have an explicit definition besides

$$E_{xc}[n] = E_i[n] - T_S[n] - E_H[n]$$

An approximate form for E_{xc} will ultimately need to made but at this point no approximations have been made at any stage of this formulation. Because the density, $n(\boldsymbol{r})$, is determined by the occupation of the single particle wavefunctions, $\phi_i(\boldsymbol{r})$, minimizing the total energy with respect to $\phi_i(\boldsymbol{r})$ is equivalent to minimizing with respect to $n(\boldsymbol{r})$, as long as orthonormality is preserved. Doing so yields the *Kohn-Sham equations*

$$\left[-\frac{\hbar^2\nabla^2}{2m} + V_{ext}(\boldsymbol{r}) + V_H(\boldsymbol{r}) + V_{xc}(\boldsymbol{r})\right]\phi_i(\boldsymbol{r}) = \varepsilon_i\phi_i(\boldsymbol{r})$$

where

$$V_H = \frac{\delta E_H[n]}{\delta n(\boldsymbol{r})} = e^2 \int \frac{n(\boldsymbol{r}')}{|\boldsymbol{r} - \boldsymbol{r}'|} d(\boldsymbol{r}')$$

and

$$V_{xc} = \frac{\delta E_{xc}[n]}{\delta n(\boldsymbol{r})}$$

It is worth noting that the Kohn-Sham orbitals, $\phi_i(\boldsymbol{r})$, and Kohn-Sham eigenvalues, ε_i, do not correspond to actual electron orbitals or energy levels, respectively. The only connection to the real electron wavefunctions is that they both yield the same density, $n(\boldsymbol{r})$. By using the Kohn-Sham orbitals to calculate the kinetic energy, the system of interacting electrons has essentially been mapped onto a system of non-interacting electrons of the same density within an effective potential that is described by the Kohn-Sham equations. The remaining issue at hand is to find an approximation for the exchange-correlation energy functional, $E_{xc}[n]$, in which all of the electron interactions have been encoded. The most common approximation to $E_{xc}[n]$ is called the local-density approximation (LDA)

$$E_{xc}[n] \approx \int n(\boldsymbol{r}) \varepsilon_{xc}(n(\boldsymbol{r}))\, d\boldsymbol{r} = E_{xc}^{LDA}[n]$$

where $\varepsilon_{xc}(n(\boldsymbol{r}))$ is the exchange-correlation energy per electron for a uniform gas of interacting electrons with density $n(\boldsymbol{r})$. By taking a derivative, an approximate form for V_{xc} may be obtained:

$$V_{xc} \approx \frac{\delta E_{xc}^{LDA}}{\delta n(\boldsymbol{r})} = \varepsilon_{xc}(n(\boldsymbol{r})) + n(\boldsymbol{r}) \frac{\partial \varepsilon_{xc}}{\partial n}\bigg|_{n(\boldsymbol{r})}$$

References

[1] Keesing, R. G. The history of Newton's apple tree. *Contemp. Phys.* **39**, 377–391 (1998).

[2] Abbott, B. P., Abbott, R., Abbott, T. D., Abernathy, M. R., Acernese, F., Ackley, K., Adams, C., Adams, T., Addesso, P., Adhikari, R. X., Adya, V. B., Affeldt, C., Agathos, M., Agatsuma, K., Aggarwal, N., Aguiar, O. D., Aiello, L., Ain, A., Ajith, P., Allen, B., et al. Observation of gravitational waves from a binary black hole merger. *Phys. Rev. Lett.* **116**, 061102 (2016).

[3] Bradt, H. *Astronomy Methods: A Physical Approach to Astonomical Observations*. (Cambridge University Press). (2003).

[4] Klug, A. Rosalind Franklin and the discovery of the structure of DNA. *Nature* **219**, 808–810 (1968).

[5] https://www.nobelprize.org/. (2024).

[6] Blatt, J. M. & Weisskopf, V. F. *Theoretical Nuclear Physics*. (Springer Science Business Media). (2012).

[7] Griffiths, D. J. *Introduction to Elementary Particles*. (Harper Row). (1987).

[8] Rumi, M. & Perry, J. W. Two-photon absorption: An overview of measurements and principles. *Adv. Opt. Photon.* **2**, 451–518 (2010).

[9] Motz, J. W., Olsen, H. A., & Koch, H. W. Pair production by photons. *Rev. Mod. Phys.* **41**, 581–639 (1969).

[10] Primakoff, H. & Rosen, S. P. Baryon number and lepton number conservation laws. *Annu. Rev. Nucl. Part. Sci.* **31**, 145–192 (1981).

[11] Als-Nielsen, J. & McMorrow, D. *Elements of Modern X-ray Physics*. (Wiley), 2 edition. (2011).

[12] Blume, M. Magnetic scattering of x rays (invited). *J. Appl. Phys.* **57**, 3615–3618 (1985).

[13] https://www.britannica.com/science/electromagnetic-spectrum. (2024).

[14] Wang, Z. L., Liu, Y., & Zhang, Z., eds. (2002) *X-ray and Neutron Scattering*. (Springer US, Boston, MA), 344–371.

[15] https://www.nist.gov/ncnr/planning-your-experiment/scattering-length-periodic-table. (2024).

[16] Treiman, A. H., LaManna, J. M., Hussey, D. S., deClue, I., & Anovitz, L. M. Coordinated neutron and x-ray computed tomography of meteorites: Detection and distribution of hydrogen-bearing materials. *Meteorit. Planet. Sci.* **57**, 1820–1835 (2022).

[17] Echevarria-Bonet, C. (2014) Ph.D. thesis.

[18] Röntgen, W. On a new kind of rays. *Nature* **53**, 274–276 (1896).

[19] Röntgen, W. Hand with rings. (1895).

[20] Jenkins, R., Manne, R., Robin, R., & Senemaud, C. IUPAC—nomenclature system for x-ray spectroscopy. *X-Ray Spectrom.* **20**, 149–155 (1991).

[21] Achkar, A. (2011) Master's thesis (University of Waterloo).

[22] Moseley, H. The high-frequency spectra of the elements. *The London, Edinburgh, and Dublin Philosophical Magazine and Journal of Science* **26**, 1024–1034 (1913).

[23] Sabchevski, S., Di Palma, E., Spassovsky, I., & Dattoli, G. Gyrotrons as high-frequency drivers for undulators and high-gradient accelerators. *Appl. Sci.* **12**, 6101 (2022).

[24] https://www.aps.anl.gov. (2024).

[25] Suller, V. Introduction to current and brightness limits. (1998).

[26] Margaritondo, G., Hwu, Y., & Tromba, G. Synchrotron light: From basics to coherence and coherence-related applications. *Science* **3**, 1 (2003).

[27] Mayerhöfer, T. G., Pahlow, S., & Popp, J. The Bouguer-Beer-Lambert law: Shining light on the obscure. *ChemPhysChem* **21**, 2029–2046 (2020).

[28] Yang, W., Liu, X., Qiao, R., Olalde-Velasco, P., Spear, J. D., Roseguo, L., Pepper, J. X., Denlinger, J. D., & Hussain, Z. Key electronic states in lithium battery materials probed by soft x-ray spectroscopy. *J. Electron. Spectrosc. Relat. Phenom.* **190**, 64–74 (2013).

[29] https://www.maths.tcd.ie/ bmurphy/thesis/thesisse4.html. (2024).

[30] Stewart, R. F. & Feil, D. A theoretical study of elastic x-ray scattering. *Acta Crystallogr. Sect. A* **36**, 503–509 (1980).

[31] Kittel, C. *Solid State Physics*. (Shell Development Company). (1955).

[32] http://pd.chem.ucl.ac.uk/. (2024).

[33] http://hyperphysics.phy-astr.gsu.edu/. (2024).

[34] Ashcroft, N. W. & Mermin, N. D. *Solid State Physics*. (Holt, Rinehart and Winston, New York, NY). (1976).

[35] Cornelius, T. W. & Thomas, O. Progress of in situ synchrotron x-ray diffraction studies on the mechanical behavior of materials at small scales. *Prog. Mater Sci.* **94**, 384–434 (2018).

[36] https://www.certif.com/spec_manual/idx.html. (2024).

[37] http://groups.mrl.uiuc.edu/chiang/czoschke/diffraction-selection-rules.html. (2024).

[38] Bednorz, J. G. & Müller, K. A. Possible high T_c superconductivity in the Ba-La-Cu-O system. *Z. Phys. B: Condens. Matter* **64**, 189–193 (1986).

[39] Hackl, R. Superconductivity in copper-oxygen compounds. *Z. Kristallogr. - Cryst. Mater.* **226**, 323–342 (2011).

[40] Searle, C. W. & Wang, S. T. Studies of the ionic ferromagnet (LaPb)MnO_3 V. Electric transport and ferromagnetic properties. *Can. J. Phys.* **48**, 2023–2031 (1970).

[41] Tokura, Y. Critical features of colossal magnetoresistive manganites. *Rep. Prog. Phys.* **69**, 797 (2006).

[42] Fink, J., Schierle, E., Weschke, E., & Geck, J. Resonant elastic soft x-ray scattering. *Rep. Prog. Phys.* **76**, 056502 (2013).

[43] Hämäläinen, K. & Manninen, S. Resonant and non-resonant inelastic x-ray scattering. *J. Phys.: Condens. Matter* **13**, 7539 (2001).

[44] Wang, S.-X. & Zhu, L.-F. Non-resonant inelastic x-ray scattering spectroscopy: A momentum probe to detect the electronic structures of atoms and molecules. *Matter Radiat. Extremes* **5**, 054201 (2020).

[45] Baron, A. Q. R. (2016) *High-Resolution Inelastic X-Ray Scattering II: Scattering Theory, Harmonic Phonons, and Calculations*, eds. Jaeschke, E. J., Khan, S., Schneider, J. R., & Hastings, J. B. (Springer International Publishing, Cham), 1721–1757.

[46] Baron, A. Q. (2016) *High-Resolution Inelastic X-Ray Scattering I: Context, Spectrometers, Samples, and Superconductors*, eds. Jaeschke, E. J., Khan, S., Schneider, J. R., & Hastings, J. B. (Springer International Publishing, Cham), 1643–1719.

[47] Ament, L. J. P., van Veenendaal, M., Devereaux, T. P., Hill, J. P., & van den Brink, J. Resonant inelastic x-ray scattering studies of elementary excitations. *Rev. Mod. Phys.* **83**, 705–767 (2011).

[48] Onnes, H. K. Further experiments with liquid helium. *Proc. K. Ned. Akad. Wet.* **13**, 1093–1113 (1911).

[49] Keimer, B., Kivelson, S. A., Norman, M. R., Uchida, S., & Zaanen, J. From quantum matter to high-temperature superconductivity in copper oxides. *Nature* **518**, 179–186 (2015).

[50] Frañó, A., Blanco-Canosa, S., Keimer, B., & Birgeneau, R. J. Charge ordering in superconducting copper oxides. *J. Phys.: Condens. Matter* **32**, 374005 (2020).

[51] Moon, E. G. & Sachdev, S. Competition between spin density wave order and superconductivity in the underdoped cuprates. *Phys. Rev. B* **80**, 035117 (2009).

[52] Agterberg, D. F., Davis, J. S., Edkins, S. D., Fradkin, E., Van Harlingen, D. J., Kivelson, S. A., Lee, P. A., Radzihovsky, L., Tranquada, J. M., & Wang, Y. The physics of pair-density waves: Cuprate superconductors and beyond. *Annu. Rev. Condens. Matter Phys.* **11**, 231–270 (2020).

[53] Valla, T., Fedorov, A., Lee, J., Davis, J., & Gu, G. The ground state of the pseudogap in cuprate superconductors. *Science* **314**, 1914–1916 (2006).

[54] Cyr-Choinière, O., Grissonnanche, G., Badoux, S., Day, J., Bonn, D., Hardy, W., Liang, R., Doiron-Leyraud, N., & Taillefer, L. Two types of nematicity in the phase diagram of the cuprate superconductor $YBa_2Cu_3O_y$. *Phys. Rev. B* **92**, 224502 (2015).

[55] Arpaia, R. & Ghiringhelli, G. Charge order at high temperature in cuprate superconductors. *J. Phys. Soc. Jpn.* **90**, 111005 (2021).

[56] Tokura, Y. & Nagaosa, N. Orbital physics in transition-metal oxides. *Science* **288**, 462–468 (2000).

[57] Sato, Y., Terasaki, I., Miyamoto, S., Tajima, S., & Tanaka, S. Anisotropic transport properties of $YBa_2Cu_3O_{7-\delta}$ single-crystal. *Adv. in Supercond. VII* 89–92 (1995).

[58] Liang, R., Dosanjh, P., Bonn, D., Baar, D., Carolan, J., & Hardy, W. Growth and properties of superconducting YBCO single crystals. *Physica C* **195**, 51–58 (1992).

[59] Jorgensen, J., Veal, B., Paulikas, A. P., Nowicki, L., Crabtree, G., Claus, H., & Kwok, W. Structural properties of oxygen-deficient $YBa_2Cu_3O_{7-\delta}$. *Phys. Rev. B* **41**, 1863 (1990).

[60] Kim, S.-M. & Lee, S. Y. Characterization of YBCO superconducting films fabricated by pulsed laser deposition. *Thin Solid Films* **355**, 461–464 (1999).

[61] Wang, C. *Theory and Application of Rare Earth Materials*. (Springer Nature). (2023).

[62] Maple, M. B. High-temperature superconductivity. *J. Magn. Magn. Mater.* **177**, 18–30 (1998).

[63] Radousky, H. B. A review of the superconducting and normal state properties of $Y_{1-x}Pr_xBa_2Cu_3O_y$. *J. Mater. Res.* **7**, 1917–1955 (1992).

[64] Rossat-Mignod, J., Regnault, L., Vettier, C., Burlet, P., Henry, J., & Lapertot, G. Investigation of the spin dynamics in $YBa_2Cu_3O_{6+x}$ by inelastic neutron scattering. *Physica B* **169**, 58–65 (1991).

[65] Maple, M., Almasan, C., Seaman, C., Han, S., Yoshiara, K., Buchgeister, M., Paulius, L., Lee, B., Gajewski, D., Jardim, R., Fincher Jr., C., Blanchet, G., & Guertin, R. Extraordinary behaviour of the $Y_{1-x}Pr_xBa_2Cu_3O_{7-\delta}$ system. *J. Supercond.* **7**, 97–106 (1994).

[66] Kang, J.-S., Haffner, S., Olson, C., Kim, J., Maple, M., Kwon, S., & Min, B. Resonant photoemission spectroscopy of the quenched superconductivity system: $Y_{1-x}Pr_xBa_2Cu_3O_{7-\delta}$ single crystals. *Phys. Rev. B* **66**, 052503 (2002).

[67] Gao, Q. & Zhang, L.-y. Bihybridization model of $Y_{1-x}Pr_xBa_2Cu_3O_{7-y}$. *Phys. Rev. B* **50**, 10230 (1994).

[68] Takata, M., Takayama, T., Sakata, M., Sasaki, S., Kodama, K., & Sato, M. Direct observation of Pr CuO_2 hybridization in $PrBa_2Cu_3O_{7-\delta}$ by the MEM charge density study. *Physica C* **263**, 340–343 (1996).

[69] Zhang, F. & Rice, T. Effective hamiltonian for the superconducting Cu oxides. *Phys. Rev. B* **37**, 3759 (1988).

[70] Fehrenbacher, R. & Rice, T. Unusual electronic structure of $PrBa_2Cu_3O_7$. *Phys. Rev. Lett.* **70**, 3471 (1993).

[71] Liechtenstein, A. & Mazin, I. Quantitative model for the superconductivity suppression in $R_{1-x}Pr_xBa_2Cu_3O_7$ with different rare earths. *Phys. Rev. Lett.* **74**, 1000 (1995).

[72] Mazin, I. & Liechtenstein, A. Location of holes in $Y_{1-x}Pr_xBa_2Cu_3O_7$. *Phys. Rev. B* **57**, 150 (1998).

[73] Singhal, R. A comparative study of Pr substitution at Y and Ba sites in $YBa_2Cu_3O_{7-\delta}$. *Mater. Lett.* **65**, 825–827 (2011).

[74] Peng, J., Klavins, P., Shelton, R., Radousky, H., Hahn, P., & Bernardez, L. Upper critical field and normal-state properties of single-phase $Y_{1-x}Pr_xBa_2Cu_3O_{7-\gamma}$ compounds. *Phys. Rev. B* **40**, 4517 (1989).

[75] Liang, J., Xu, X., Xie, S., Rao, G., Shao, X., & Duan, Z. The superconductive properties and crystal structure of $Ba_2(Y_{1-x}Pr_x)Cu_3O_{9-y}$ solid solutions. *Z. Phys. B: Condens. Matter* **69**, 137–140 (1987).

[76] Chittipeddi, S., Song, Y., Cox, D., Gaines, J., Golben, J., & Epstein, A. J. Resistive and magnetic studies of $NdBa_2Cu_3O_{7-\delta}$ and $PrBa_2Cu_3O_{7-\delta}$. *Phys. Rev. B* **37**, 7454 (1988).

[77] López-Morales, M., Bezinge, A., Grant, P., & Ríos-Jara, D. Praseodymium 1-2-3: Intrinsic structure, oxygen concentration effects, and solid solutions with yttrium, calcium and zinc. *Physica C* **162**, 61–62 (1989).

[78] Horn, J., Semmelhack, H.-C., Börner, H., Lippold, B., Boehnke, U., Wurlitzer, M., & Krötzsch, M. Thermogravimetric and structural investigations of $Pr_xY_{1-x}Ba_2Cu_3O_{7-\delta}$. *Physica C* **170**, 343–349 (1990).

[79] Jorgensen, J. D. Defects and superconductivity in the copper oxides. *Phys. Today* **44**, 34–40 (1991).

[80] Narlikar, A., Gupta, A., Samanta, S., Chen, C., Hu, Y., Wondre, F., Wanklyn, B., & Hodby, J. Nanolevel studies of lattice defects and electronic structure of $YBa_2Cu_3O_7$ single crystals doped with praseodymium: Destruction of superconductivity. *Philos. Mag. B* **79**, 717–728 (1999).

[81] Blackstead, H. A. & Dow, J. D. Role of Ba-site Pr in quenching superconductivity of $Y_{1-y}Pr_yBa_2Cu_3O_x$ and related materials. *Phys. Rev. B* **51**, 11830 (1995).

[82] Blackstead, H. A. & Dow, J. D. Implications of superconductivity of $PrBa_2Cu_3O_7$. *Solid State Commun.* **115**, 137–140 (2000).

[83] Ferreira, L. M., Pureur, P., Borges, H. A., & Lejay, P. Effects of pressure on the fluctuation conductivity of YBa_2Cu_3O7. *Phys. Rev. B* **69**, 212505 (2004).

[84] Sharma, P., Kumar, S., Dolia, S., & Singhal, R. *Pr substitution at Y and Ba sites in YBCO (123) System*. (American Institute of Physics), Vol. 1349, 905–906 (2011).

[85] Blackstead, H., Dow, J. D., Chrisey, D., Horwitz, J., Black, M., McGinn, P., Klunzinger, A., & Pulling, D. Observation of superconductivity in $PrBa_2Cu_3O_7$. *Phys. Rev. B* **54**, 6122 (1996).

[86] Zou, Z., Ye, J., Oka, K., & Nishihara, Y. Superconducting $PrBa_2Cu_3O_x$. *Phys. Rev. Lett.* **80**, 1074 (1998).

[87] Paulius, L., Lee, B., Maple, M., & Tsai, P. Preparation and characterization of $Y_{1-x}Pr_xBa_2Cu_3O_{7-\delta}$ single crystals. *Physica C* **230**, 255–262 (1994).

[88] Newville, M. *Larch: An analysis package for XAFS and related spectroscopies*. (IOP Publishing), Vol. 430, 012007 (2013).

[89] Frañó, A. *Spin Spirals and Charge Textures in Transition-Metal-Oxide Heterostructures*. (Springer). (2014).

[90] Haverkort, M. W. *Quanty for core level spectroscopy-excitons, resonances and band excitations in time and frequency domain*. (IOP Publishing), Vol. 712, 012001 (2016).

[91] Goodman, G., Loong, C.-K., & Soderholm, L. Crystal field properties of f-electron states in $RBa_2Cu_3O_7$ for R= Ho, Nd and Pr. *J. Phys.: Condens. Matter* **3**, 49 (1991).

[92] Thole, B., Van der Laan, G., Fuggle, J., Sawatzky, G., Karnatak, R., & Esteva, J.-M. 3d x-ray-absorption lines and the $3d^9\ 4f^{n+1}$ multiplets of the lanthanides. *Phys. Rev. B* **32**, 5107 (1985).

[93] Magnuson, M., Schmitt, T., & Duda, L.-C. Polarization-dependent resonant inelastic x-ray scattering study at the Cu L and O K-edges of $Y_{1-x}Ba_2Cu_3O_{7-x}$. *J. Electron. Spectrosc. Relat. Phenom.* **224**, 38–44 (2018).

[94] Yavaş, H., Sundermann, M., Chen, K., Amorese, A., Severing, A., Gretarsson, H., Haverkort, M. W., & Tjeng, L. H. Direct imaging of orbitals in quantum materials. *Nat. Phys.* **15**, 559–562 (2019).

[95] Leedahl, B., Sundermann, M., Amorese, A., Severing, A., Gretarsson, H., Zhang, L., Komarek, A. C., Maignan, A., Haverkort, M. W., & Tjeng, L. H. Origin of ising magnetism in $Ca_3Co_2O_6$ unveiled by orbital imaging. *Nat. Commun.* **10**, 5447 (2019).

[96] Amorese, A., Leedahl, B., Sundermann, M., Gretarsson, H., Hu, Z., Lin, H.-J., Chen, C., Schmidt, M., Borrmann, H., Grin, Y., Severing, A., Haverkort, M., & Tjeng, L. Selective orbital imaging of excited states with x-ray spectroscopy: The example of α-MnS. *Phys. Rev. X* **11**, 011002 (2021).

[97] Jiang, W., Peng, J., Hagen, S., & Greene, R. Hall-effect studies of $Y_{1-x}Pr_xBa_2Cu_3O_7$ crystals. *Phys. Rev. B* **46**, 8694 (1992).

[98] Zhang, S., Chiu, I.-T., Lee, M.-H., Gunn, B., Feng, M., Park, T. J., Shafer, P., N'Diaye, A. T., Rodolakis, F., Ramanathan, S., Frañó, A., Schuller, I. K., Takamura, Y., & Galli, G. Determining the oxygen stoichiometry of cobaltite thin films. *Chem. Mater.* **34**, 2076–2084 (2022).

[99] Vovk, R., Vovk, N., Shekhovtsov, O., Goulatis, I., & Chroneos, A. c-axis hopping conductivity in heavily Pr-doped YBCO single crystals. *Supercond. Sci. Technol.* **26**, 085017 (2013).

[100] Hervieu, M., Barnabé, A., Martin, C., Maignan, A., Damay, F., & Raveau, B. Evolution of charge ordering in manganites. *Eur. Phys. J. B* **8**, 31–41 (1999).

[101] Lee, S., Chen, R., & Balents, L. Landau theory of charge and spin ordering in the nickelates. *Phys. Rev. Lett.* **106**, 016405 (2011).

[102] Robertson, J. A., Kivelson, S. A., Fradkin, E., Fang, A. C., & Kapitulnik, A. Distinguishing patterns of charge order: Stripes or checkerboards. *Phys. Rev. B* **74**, 134507 (2006).

[103] Chen, C. & Cheong, S. Commensurate to incommensurate charge ordering and its real-space images in $La_{0.5}Ca_{0.5}MnO_3$. *Phys. Rev. Lett.* **76**, 4042 (1996).

[104] Peierls, R. E. *Quantum Theory of Solids*. (Clarendon Press). (1996).

[105] Aebi, P., Pillo, T., Berger, H., & Lévy, F. On the search for Fermi surface nesting in quasi-2D materials. *J. Electron. Spectrosc. Relat. Phenom.* **117**, 433–449 (2001).

[106] Johannes, M. & Mazin, I. Fermi surface nesting and the origin of charge density waves in metals. *Phys. Rev. B* **77**, 165135 (2008).

[107] Comin, R. & Damascelli, A. Resonant x-ray scattering studies of charge order in cuprates. *Annu. Rev. Condens. Matter Phys.* **7**, 369–405 (2016).

[108] Obertelli, S., Cooper, J., & Tallon, J. Systematics in the thermoelectric power of high-T_c oxides. *Phys. Rev. B* **46**, 14928 (1992).

[109] Tranquada, J., Sternlieb, B., Axe, J., Nakamura, Y., & Uchida, S.-i. Evidence for stripe correlations of spins and holes in copper oxide superconductors. *Nature* **375**, 561–563 (1995).

[110] Blanco-Canosa, S., Frañó, A., Schierle, E., Porras, J., Loew, T., Minola, M., Bluschke, M., Weschke, E., Keimer, B., & Le Tacon, M. Resonant x-ray scattering study of charge-density wave correlations in $YBa_2Cu_3O_{6+x}$. *Phys.Rev.B* **90**, 054513 (2014).

[111] Chang, J., Blackburn, E., Holmes, A., Christensen, N. B., Larsen, J., Mesot, J., Liang, R., Bonn, D., Hardy, W., Watenphul, A., Zimmermann, M., Forgan, E., & Hayden, S. Direct observation of competition between superconductivity and charge density wave order in $YBa_2Cu_3O_{6.67}$. *Nat. Phys.* **8**, 871–876 (2012).

[112] Bluschke, M., Frañó, A., Schierle, E., Putzky, D., Ghorbani, F., Ortiz, R., Suzuki, H., Christiani, G., Logvenov, G., Weschke, E., Birgeneau, R. J., da Silva Neto, E. H., Minola, M., Blanco-Canosa, S., & Keimer, B. Stabilization of three-dimensional charge order in $YBa_2Cu_3O_{6+x}$. *Nat. Commun.* **9** (2018).

[113] Robinson, I. K. Crystal truncation rods and surface roughness. *Phys. Rev. B* **33**, 3830 (1986).

[114] Chang, J., Blackburn, E., Ivashko, O., Holmes, A. T., Christensen, N. B., Hücker, M., Liang, R., Bonn, D. A., Hardy, W. N., Rütt, U., Zimmermann, M. V., Forgan, E. M., & Hayden, S. M. Magnetic field controlled charge density wave coupling in underdoped $YBa_2Cu_3O_{6+x}$. *Nat. Commun.* **7**, 11494 (2016).

[115] Kim, H.-H., Souliou, S. M., Barber, M. E., Lefrançois, E., Minola, M., Tortora, M., Heid, R., Nandi, N., Borzi, R. A., Garbarino, G., Bosak, A., Porras, J., Loew, T., König, M., Moll, P. J. W., Mackenzie, A. P., Keimer, B., Hicks, C. W., & Le Tacon, M. Uniaxial pressure control of competing orders in a high-temperature superconductor. *Science* **362**, 1040–1044 (2018).

[116] Ravel, B. & Newville, M. ATHENA, ARTEMIS, HEPHAESTUS: Data analysis for x-ray absorption spectroscopy using IFEFFIT. *J. Synchrotron Radiat.* **12**, 537–541 (2005).

[117] Jang, H., Lee, W.-S., Nojiri, H., Matsuzawa, S., Yasumura, H., Nie, L., Maharaj, A., Gerber, S., Liu, Y.-J., Mehta, A., Bonn, D., Liang, R., Hardy, W., Burns, C., Islam, Z., Song, S., Hastings, J., Devereaux, D., Shen, Z.-X., Kivelson, S., Kao, C.-C., Zhe, D., & Lee, J.-S. Ideal charge-density-wave order in the high-field state of superconducting YBCO. *Proceedings of the National Academy of Sciences* **113**, 14645–14650 (2016).

[118] Tabis, W., Yu, B., Bialo, I., Bluschke, M., Kolodziej, T., Kozlowski, A., Blackburn, E., Sen, K., Forgan, E. M., Zimmermann, M. v., Tang, Y., Weschke, E., Vignolle, B., Hepting, M., Gretarsson, H., Sutarto, R., He, F., Le Tacon, M., Barišić, N., Yu, G., & Greven, M. Synchrotron x-ray scattering study of charge-density-wave order in $HgBa_2CuO_{4+}\delta$. *Phys. Rev. B* **96**, 134510 (2017).

[119] Ghiringhelli, G., Le Tacon, M., Minola, M., Blanco-Canosa, S., Mazzoli, C., Brookes, N., De Luca, G., Frañó, A., Hawthorn, D., He, F., Loew, T., Moretti Sala, M., Peets, D., Salluzzo, M., Schierle, E., Sutarto, R., Sawatzky, G., Weschke, E., Keimer, B., & Braicovich, L. Long-range incommensurate charge fluctuations in (Y, Nd)$Ba_2Cu_3O_{6+x}$. *Science* **337**, 821–825 (2012).

[120] Comin, R., Frañó, A., Yee, M. M., Yoshida, Y., Eisaki, H., Schierle, E., Weschke, E., Sutarto, R., He, F., Soumyanarayanan, A., He, Y., Le Tacon, M., Elfimov, I., Hoffman, J., Sawatzky, G., Keimer, B., & Damascelli, A. Charge order driven by Fermi-arc instability in $Bi_2Sr_{2-x}La_xCuO_{6+\delta}$. *Science* **343**, 390–392 (2014).

[121] da Silva Neto, E. H., Aynajian, P., Frañó, A., Comin, R., Schierle, E., Weschke, E., Gyenis, A., Wen, J., Schneeloch, J., Xu, Z., Ono, S., Gu, G., Le Tacon, M., & Yazdani, A. Ubiquitous interplay between charge ordering and high-temperature superconductivity in cuprates. *Science* **343**, 393–396 (2014).

[122] Arpaia, R., Caprara, S., Fumagalli, R., De Vecchi, G., Peng, Y., Andersson, E., Betto, D., De Luca, G., Brookes, N., Lombardi, F., Salluzzo, M., Braicovich, L., di Castro, C., Grilli, M., & Ghirinchelli, G. Dynamical charge density fluctuations pervading the phase diagram of a Cu-based high-T_c superconductor. *Science* **365**, 906–910 (2019).

[123] Zhu, W., Liu, P., & Zhao, Z. Rare-earth ionic size effect on the Pr-induced T_c depression in the series $R_{1-x}Pr_xBa_2Cu_3O_{7-\delta}$ (R= Sm, Gd, Y, Er, Tm). *Physica C* **199**, 285–288 (1992).

[124] Blaha, P., Schwarz, K., Madsen, G. K., Kvasnicka, D., & Luitz, J. WIEN2k: An augmented plane wave+ local orbitals program for calculating crystal properties. *Institut Für Physikalische und Theoretische Chemie: Vienna, Austria* **60** (2001).

[125] Blaha, P., Schwarz, K., Tran, F., Laskowski, R., Madsen, G. K., & Marks, L. D. WIEN2k: An APW+ lo program for calculating the properties of solids. *J. Chem. Phys.* **152** (2020).

[126] Betto, D., Bluschke, M., Putzky, D., Schierle, E., Amorese, A., Fürsich, K., Blanco-Canosa, S., Christiani, G., Logvenov, G., Keimer, B., & Minola, M. Imprint of charge and oxygen orders on Dy ions in $DyBa_2Cu_3O_{6+x}$ thin films probed by resonant x-ray scattering. *Phys. Rev. B* **102**, 195149 (2020).

[127] Mishchenko, A. & Nagaosa, N. Electron-phonon coupling and a polaron in the t-J model: from the weak to the strong coupling regime. *Phys. Rev. Lett.* **93**, 036402 (2004).

[128] Capone, M., Castellani, C., & Grilli, M. Electron-phonon interaction in strongly correlated systems. *Adv. Condens. Matter Phys.* **2010** (2010).

[129] Le Tacon, M., Bosak, A., Souliou, S., Dellea, G., Loew, T., Heid, R., Bohnen, K., Ghiringhelli, G., Krisch, M., & Keimer, B. Inelastic x-ray scattering in $YBa_2Cu_3O_{6.6}$ reveals giant phonon anomalies and elastic central peak due to charge-density-wave formation. *Nat. Phys.* **10**, 52–58 (2014).

[130] Blackburn, E., Chang, J., Said, A., Leu, B., Liang, R., Bonn, D. A., Hardy, W., Forgan, E. M., & Hayden, S. M. Inelastic x-ray study of phonon broadening and charge-density wave formation in ortho-II-ordered $YBa_2Cu_3O_{6.54}$. *Phys. Rev. B* **88**, 054506 (2013).

[131] Luther, A. & Peschel, I. Single-particle states, Kohn anomaly, and pairing fluctuations in one dimension. *Phys. Rev. B* **9**, 2911 (1974).

[132] Neto, A. C., Guinea, F., Peres, N. M., Novoselov, K. S., & Geim, A. K. The electronic properties of graphene. *Rev. Mod. Phys.* **81**, 109 (2009).

[133] Jiang, K., Wu, T., Yin, J.-X., Wang, Z., Hasan, M. Z., Wilson, S. D., Chen, X., & Hu, J. Kagome superconductors AV_3Sb_5 (A= K, Rb, Cs). *Natl. Sci. Rev.* **10**, nwac199 (2023).

[134] Neupert, T., Denner, M. M., Yin, J.-X., Thomale, R., & Hasan, M. Z. Charge order and superconductivity in kagome materials. *Nat. Phys.* **18**, 137–143 (2022).

[135] Yin, J.-X., Jiang, Y.-X., Teng, X., Hossain, M. S., Mardanya, S., Chang, T.-R., Ye, Z., Xu, G., Denner, M. M., Neupert, T., Lienhard, B., Deng, H.-B., Setty, C., Si, Q., Chang, G., Guguchia, Z., Gao, B., Shumiya, N., Zhang, Q., Cochran, T., Multer, D., Yi, M., Dai, P., & Hasan, M. Discovery of charge order and corresponding edge state in kagome magnet FeGe. *Phys. Rev. Lett.* **129**, 166401 (2022).

[136] Chen, H., Nassar, H., & Huang, G. Topological mechanics of edge waves in kagome lattices. *arXiv preprint arXiv:1802.04404* (2018).

[137] Hu, Y., Wu, X., Ortiz, B. R., Ju, S., Han, X., Ma, J., Plumb, N. C., Radovic, M., Thomale, R., Wilson, S. D., Schnyder, A. P., & Shi, M. Rich nature of van hove singularities in kagome superconductor CsV_3Sb_5. *Nat. Commun.* **13**, 2220 (2022).

[138] Yin, J.-X., Lian, B., & Hasan, M. Z. Topological kagome magnets and superconductors. *Nature* **612**, 647–657 (2022).

[139] Villain, J., Bidaux, R., Carton, J.-P., & Conte, R. Order as an effect of disorder. *J. Phys.* **41**, 1263–1272 (1980).

[140] Zhou, Y., Kanoda, K., & Ng, T.-K. Quantum spin liquid states. *Rev. Mod. Phys.* **89**, 025003 (2017).

[141] Balents, L. Spin liquids in frustrated magnets. *Nature* **464**, 199–208 (2010).

[142] Teng, X., Oh, J. S., Tan, H., Chen, L., Huang, J., Gao, B., Yin, J.-X., Chu, J.-H., Hashimoto, M., Lu, D., Jozwiak, C., Bostwick, A., Rotenberg, E., Granroth, G., Yan, B., Birgeneau, R., Dai, P., & Yi, M. Magnetism and charge density wave order in kagome FeGe. *Nat. Phys.* **19**, 814–822 (2023).

[143] Wang, W.-S., Li, Z.-Z., Xiang, Y.-Y., & Wang, Q.-H. Competing electronic orders on kagome lattices at van Hove filling. *Phys. Rev. B* **87**, 115135 (2013).

[144] Teng, X., Chen, L., Ye, F., Rosenberg, E., Liu, Z., Yin, J.-X., Jiang, Y.-X., Oh, J. S., Hasan, M. Z., Neubauer, K. J., Gao, B., Xie, Y., Hashimoto, M., Lu, D., Jozwiak, C., Bostwick, A., Rotenberg, E., Birgeneau, R. J., Chu, J.-H., Yi, M., & Dai, P. Discovery of charge density wave in a kagome lattice antiferromagnet. *Nature* **609**, 490–495 (2022).

[145] Wang, Y. Enhanced spin-polarization via partial Ge-dimerization as the driving force of the charge density wave in FeGe. *Phys. Rev. Mater.* **7**, 104006 (2023).

[146] Kulić, M. & Dolgov, O. Dominance of the electron-phonon interaction with forward scattering peak in high-T_c superconductors: theoretical explanation of the ARPES kink. *Phys. Rev. B* **71**, 092505 (2005).

[147] Hou, C.-Y., Chamon, C., & Mudry, C. Electron fractionalization in two-dimensional graphenelike structures. *Phys. Rev. Lett.* **98**, 186809 (2007).

[148] Shao, S., Yin, J.-X., Belopolski, I., You, J.-Y., Hou, T., Chen, H., Jiang, Y., Hossain, M. S., Yahyavi, M., Hsu, C.-H., Feng, Y. P., Banzil, A., Hasan, M. Z., & Chang, G. Intertwining of magnetism and charge ordering in kagome FeGe. *ACS nano* **17**, 10164–10171 (2023).

[149] Richardson, M., Ingri, N., Salomaa, P., Bloom, G., & Hagen, G. The partial equilibrium diagram of the Fe-Ge system in the range 40–72 at.% Ge, and the crystallisation of some iron germanides by chemical transport reactions. *Acta Chem. Scand* **21** (1967).

[150] Dubois, M., Guérin, K., Hamwi, A., & Vinogradov, A. (2017) in *New Fluorinated Carbons: Fundamentals and Applications*. (Elsevier), 215–243.

[151] Perdew, J. P., Burke, K., & Ernzerhof, M. Generalized gradient approximation made simple. *Phys. Rev. Lett.* **77**, 3865 (1996).

[152] Jena, D. *Quantum Physics of Semiconductor Materials and Devices*. (Oxford University Press). (2022).

[153] Thompson, D. The reciprocal lattice as the Fourier transform of the direct lattice. *Am. J. Phys.* **64**, 333–334 (1996).

[154] Arovas, D. Lecture notes on condensed matter physics https://courses.physics.ucsd.edu/2020/Spring/physics239/LECTURES/CONDMAT.pdf. (2023).

[155] Girvin, S. M. & Yang, K. *Modern Condensed Matter Physics*. (Cambridge University Press). (2019).

[156] Hohenberg, P. & Kohn, W. Inhomogeneous electron gas. *Phys. Rev.* **136**, B864 (1964).

[157] Kohn, W. & Sham, L. J. Self-consistent equations including exchange and correlation effects. *Phys. Rev.* **140**, A1133 (1965).